2010

Combustion Dynamics And Fluid Mechanics In Acoustically Perturbed Non-premixed Swirl-stabilized Flames.

Uyi Idahosa
University of Central Florida

COMBUSTION DYNAMICS AND FLUID MECHANICS IN ACOUSTICALLY PERTURBED NON–PREMIXED SWIRL–STABILIZED FLAMES

By

UYI O. IDAHOSA
B.Sc. Embry Riddle Aeronautical University, 2003
M.Sc. Embry Riddle Aeronautical University, 2005

A dissertation submitted in partial fulfillment of the requirements
for the degree of Doctor of Philosophy
in the Department of Mechanical, Materials and Aerospace Engineering
in the College of Engineering and Computer Science
at the University of Central Florida
Orlando, Florida

Summer Term
2010

Major Professor: Saptarshi Basu

ABSTRACT

The prevalence of gas turbines operating in primarily lean premixed modes is predicated on the need for lower emissions and increased efficiency. An enhancement in the mixing process through the introduction of swirl in the combustion reactants is also necessary for flame stabilization. The resulting lean swirling flames are often characterized by a susceptibility to feedback between velocity, pressure and heat release perturbations with a potential for unstable self-amplifying dynamics.

The existing literature on combustion dynamics is predominantly dedicated to premixed flame configurations motivated by power generation and propulsive gas turbine applications. In the present research effort, an investigation into the response of atmospheric, non-premixed swirling flames to acoustic perturbations at various frequencies (f_p = 0 – 315 Hz) and swirl intensities (S = 0.09 and 0.34) is carried out. The primary objective of the research effort is to broaden the scope of fundamental understanding in flame dynamics in the literature to include non-premixed swirling flames. Applications of the research effort include control strategies to mitigate the occurrence of combustion instabilities in future power generation gas turbines.

Flame heat release is quantitatively measured using a photomultiplier with a 430nm bandpass filter for observing CH* chemiluminescence which is simultaneously imaged with a phase-locked CCD camera. Acoustic perturbations are generated with a loudspeaker at the base of an atmospheric co-flow burner with resulting velocity oscillation amplitudes $|u'/U_{avg}|$ in the 0.03 –

0.30 range. The dependence of flame dynamics on the relative richness of the flame is investigated by studying various constant fuel flow rate flame configurations. The effect of varying fuel flow rates on the flame response is also examined using with dynamic time-dependent fuel supply rates over the data acquisition period. The Particle Image Velocimetry (PIV) method is used to study the isothermal flow field associated with acoustic pulsing. The acoustic impedance, wavelet analysis, Rayleigh criteria and phase conditioning methods are used to identify fundamental mechanisms common to highly responsive flame configurations.

To Barbara

ACKNOWLEDGMENTS

I would like to thank my advisors Dr. Saptarshi Basu and Dr. Chengying Xu for their guidance over various aspects of the project. I also wish to thank Dr. Vladimir Golubev for his valuable direction over various stages of my academic career and his insights on the acoustic aspects of the current study. My thanks also to Dr. Reda Mankbadi at Embry Riddle Aeronautical University, Daytona Beach, FL for his guidance both academically and professionally. I would also like to thank the other members of my dissertation committee including Dr. Jayanta Kapat and Dr. Ranganathan Kumar for reviewing the manuscript as well as their service on my committee. I also wish to acknowledge the support of the Freshmen Engineering Department at Embry Riddle Aeronautical University, Daytona Beach Florida. The assistance and support have contributed immensely to my ability to pursue this endeavor.

I gratefully acknowledge the assistance from the members of our research group particularly Abhishek Saha and Navid Khatami who helped me significantly at various phases of the research effort. Their assistance has been invaluable in completing this research effort.

I would like to thank my family for their wonderful unconditional support, particularly to my lovely wife Barbara who has tolerated long hours of solitude while I pursued this effort. I would like to express my earnest gratitude to my parents for their steady support. I would not have the opportunities that have come my way without their encouragement.

TABLE OF CONTENTS

LIST OF FIGURES

LIST OF TABLES

CHAPTER 1 INTRODUCTION

1.1 Background and Motivation

In modern gas turbines, the use of swirl in stabilizing combustion processes is critical in enhancing efficiency, reducing emissions as well as optimizing engine performance**.** These improvements are highly correlated to the enhancement of the mixing process in the combustor with swirl inducing mechanisms such as swirl vanes and tangentially directed air supply ports. However, swirl enhanced lean combustion has been observed to be characterized by dynamic feedback mechanisms between equivalence ratio, heat release rate and pressure perturbations particularly at the combustor natural acoustic modes [1-8].

These feedback mechanisms can lead to self-excitation in cases where the relevant perturbations are in phase as defined by the Rayleigh Criterion [9, 10], amplifying the response of the system and resulting in undesirable installation damage, inefficient operation and increased NOx emissions among other effects [7, 11]. The prediction of the onset of instability requires a thorough understanding of the physical processes that govern the dynamic response of the combustion process. Several significant physical phenomena contribute to the dynamics of the combustion process including heat release rate, swirl intensity, flow field properties (vortex formation and shedding), flame surface area fluctuations and fuel dependent chemical kinetics [7, 12-14].

Especially important as captured by the Rayleigh criteria is the phase relationship between various flame dynamics processes. For the atmospheric unconfined burner in the present study, the primary processes essential to the flame response include:

- The flow perturbations (*u'*) at the burner exit
- The resulting heat release oscillations (*q'*) induced in the flame
- The generated acoustic perturbations (*p'*) propagating upstream/downstream

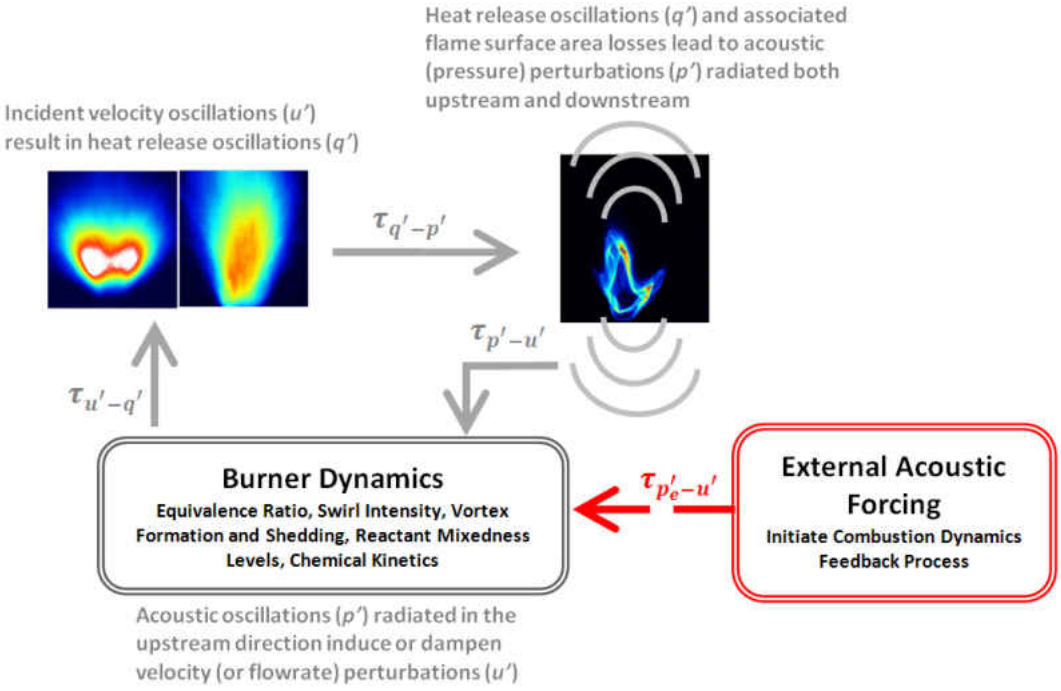

Figure 1.1 General Processes in Flame Response Dynamics

The interactions between these processes are illustrated in Figure 1.1. Velocity perturbations (*u'*) at the burner exit lead to heat release rate (*q'*) oscillations relative to a time delay which is dependent on several parameters including equivalent ratio, swirl intensity, mixing of fuel and reactants and vortex shedding characteristics. Heat release oscillations are in turn linked to flame surface area losses accompanied by combustion noise from the accompanying acoustic

(p') perturbations [5-7] depending on the time delay between the processes. The acoustic radiation from the flame in the upstream direction augments or dampens the velocity perturbations inherent at the burner exit once again dependent on the time delays between the two processes [7-8].

The various time delays essentially translate to phase relationships between these parameters. Several studies [1-8, 10-15] have been carried out to examine the conditions in terms of phase relationships delays between the various parameters. In particular, the phase relationships which lead to self-amplification of the velocity and heat release perturbations are of particular importance due to the potential for significant combustor damage. As illustrated in Figure 1.1, the conditions favorable for self-amplification can be investigated through the introduction of external acoustic forcing on the flame and quantifying the gain and phase response among the various flame dynamics parameters [11-12, 14-16].

1.2 Research Objectives

The motivation behind this study is to broaden the fundamental understanding of flame configurations in the literature to include non-premixed atmospheric swirl stabilized flames. Although a large number of existing power generation and propulsive turbines are based on premixed flame combustion, there is a potential for future non-premixed flame application in power generation gas turbines. An example is the Siemens SGT5-2000E2 power generation gas turbine which burns Syngas in a non-premixed configuration.

The primary objective is to understand and quantify the various parameters that govern the non-premixed flame response to acoustic perturbations. Flame configurations with significant responses characterized by sustained heat release rate and velocity amplification are of particular interest. The research effort is primarily divided into two broad categories including:

(1) The response to acoustic pulsing in a hot (flame present) configuration.

(2) The response of the isothermal cold flow (inert, no flame) fluid dynamics associated with the imposed acoustic perturbations.

A characterization of the response to acoustic perturbations at varying frequencies is carried out using various experimental and analytic techniques including chemiluminescence imaging, phase conditioning, acoustic impedance and wavelet transform methods. The Particle Image Velocimetry (PIV) technique is used to study the isothermal flow fields associated with the various flame configurations to enable correlation between fluid and heat release rate dynamics. This enables the isolation of the fluid dynamic components of the observed flame response. The effect of swirl intensity on the flame response is also studied using different swirl intensities. A flame response index (R) is defined for identifying highly responsive flame configurations and its accuracy is investigated. The flame response index is analogous to the Rayleigh criteria associated with unpulsed flame configurations in several studies [9, 10, 14-15]. The acoustic impedance technique is also utilized in understanding fundamental flame response mechanisms. Finally, common criteria in highly responsive configurations among the studied non-premixed swirling flames are presented.

1.3 Dissertation Outline

The background and motivation for the research effort is highlighted in Chapter 1 with a basic overview of the critical processes important in the flame response to acoustic perturbations. Also included in the chapter is a basic outline of the dissertation document.

Chapter 2 is devoted to a review of existing literature related to the dynamics in unperturbed and acoustically forced flames of various types including premixed, non-premixed (diffusion), bluff body, perforated plate and swirling configurations. Significant attention is paid to reviewing the conditions and fundamental mechanisms identified in the literature as common to high responsive flames. These include flames under acoustically forced conditions as well as unperturbed flames that characterized by self-amplification and feedback dynamics. The use of the acoustic impedance at the burner-flame interface in analyzing the flame response is reviewed along with the application of the continuous wavelet transform method to be applied in the present investigation.

Existing literature on the fluid dynamics associated with acoustic forcing of isothermal (inert) conditions with no flame is also presented. Chapter 2 also includes summaries of existing investigations of critical fluid dynamic phenomena in inert swirling configurations. Reviews on fluid phenomena including large scale vortex shedding (LSVS), precessing vortex cores (PVCs) and the formation of central (inner) and outer recirculation zones are presented.

Chapter 3 details the experimental approach applied in the present investigation. Specifications on the equipment utilized are provided along with the timing sequences used in data acquisition. Several analysis methods are employed in the present study including the familiar Fast Fourier Transform (FFT). Other analytical tools applied include the Continuous Wavelet Transform (CWT), acoustic impedance, coherence as well as the Rayleigh criteria. General descriptions of these analyses methods are also provided in the chapter. The swirl intensities, fuel flowrates, Reynolds' numbers and associated baseline experimental parameters are also discussed.

The combustion dynamics results for acoustically perturbed flame configurations with constant (time-invariant) fuel flow rates are presented in Chapter 4. This is followed in Chapter 5 by analogous results for flame configurations with time-varying fuel flowrates until flame extinction. All results are presented for two swirl intensities and two baseline fuel flow rates. The different flowrates are employed to study the impact of relatively lean vs. rich flame configurations on the observed response to the incident acoustics.

Chapter 6 discusses the results of isothermal fluid dynamics carried out on inert configurations where no flame is present. The primary objective is to examine the purely fluid dynamics components of the observed flame responses. In particular, the relationships between the recirculation zone dynamics, vortex shedding and swirl intensity is discussed. Summary conclusions including the conditions for responsive flame are presented in Chapter 7 along with possible directions for future research based on the current investigation.

CHAPTER 2 LITERATURE REVIEW

2.1 Experimental Investigations

Combustion dynamics investigations have been motivated by feedback mechanisms between acoustic propagation and the combustion process. This feedback between the acoustic and combustion processes is known to lead to coupling and self-amplification that may lead to significant combustor hardware and installation damage [1-5]. Historically, thermoacoustic instabilities have been observed in liquid propellant rocket engines since the 1950's and HVAC and furnace industries in the 1970's. The advent and rapid expansion of Dry Low NOx (DLN) power generation gas turbines operating in lean regimes in the 1990's meant that issues with thermoacoustic instabilities had to be addressed to further extend the lean regimes of these gas turbines.

Experiments such as those carried out by Schuller and Candel [6-7] have show that these thermoacoustic instabilities are caused by large amplitude oscillations when the flame is subjected to acoustic perturbations. The resulting fluctuations in heat release rate are accompanied by similarly cyclic flame surface area losses. These flame surface area losses are the result of interaction and annihilation between adjacent elements of the flame sheet and lead to an intense emission of sound (pressure perturbations). The sound related pressure perturbations in turn serve as the driving source of Helmholtz-type resonant burner modes particularly in the low frequency regime [8].

Thermoacoustic instabilities are only triggered depending on the tradeoff between the acoustic driving and damping as illustrated by Lieuwen and Preetham [3, 10]. The flame may respond as an amplifier due to the constructive superposition of flame disturbances by incident acoustics. For destructive superposition between the flame disturbances the flame response may be identically zero [11]. The time-delays between the various velocity, heat release rate and pressure oscillations are a strong indicator of the degree of feedback and synchronization necessary for instability to be initiated. In essence, the processes that drive heat release rate oscillations do not necessary lead to instability depending on the phase and amplitude relationships between the dynamic processes. Time delays between acoustic and combustion phenomena essentially translate to phase differences.

The criterion theoretically presented by Lord Rayleigh [4, 9-12] is used to assess the combustion-acoustics phase relationship as quantified by the heat release rate (*q'*) and acoustic pressure (*p'*). Several forms of the Rayleigh criterion exist in literature with the more widely used formulation:

$$R = \int_0^T q'(\mathrm{t}) p'(t) dt \tag{2.1}$$

T designates the total data sample acquisition period. The Rayleigh index will result in positive (≥ 0) values for in-phase heat release rate and pressure oscillation and negative values for out-of-phase fluctuations as a prerequisite for occurrence of thermoacoustic instabilities [3, 13-14]. The Rayleigh condition only exists as a necessary but insufficient condition for the initiation of

instabilities. In addition to in-phase acoustic and heat release rate oscillations, the amplitude of the acoustic source must sufficient to overwhelm the damping mechanisms in the system including acoustic linear and combustor geometry to minimize reflected acoustic radiation within the combustor. Nicoud [14] and Durox [15] present extensions of the Rayleigh with the integral in Eq. 2.1 as the acoustic source term along with power dissipation and radiation energy flux terms to account for the driving and damping processes respectively. In the present work, the widely used Rayleigh index defined in Eq. 2.1 is utilized.

The investigation of thermoacoustic instabilities requires a quantification of heat release rate of the flame relative to incident acoustics. The heat release rate (q') is generally assumed proportional to the light intensity of combustion related radicals including CH*, the hydroxyl radical OH* and formaldehyde (CH_2O) [15-19]. Photomultiplier tubes (PMT) centered at 430nm and 310nm are typically used to observe the chemiluminescence of the CH* and OH* radicals emitted due to the combustion process. CCD imaging phase-locked to the perturbation signal in acoustically forced flames also allow the correlation of the observed flame geometry to the acoustic oscillation. Typically, the CCD cameras are fitted with filters for the imaging of the chemiluminescence of the appropriate radicals.

A third widely used tool is the Planar Laser Induced Fluorescence (PLIF) technique highly detailed in the works on Schulz and Sick [20]. Tracers including biacetyl and acetone are used to seed the fluid medium and a laser sheet used to excite the tracer molecules. The tracer molecules emit radiation at various wavelengths which are captures via CCD imaging camera.

The PLIF technique may be applied to mapping mixture fractions, temperature and to some extent pressure in reacting medium. Ayoola et al. [21] carried out the spatial resolution of het release rate measurements in turbulent premixed flames using the PLIF technique to observe hydroxyl (OH*) and formaldehyde (CH_2O) chemiluminescence. The OH* PLIF imaging was achieved by exciting the acetone tracer molecules with a laser sheet tuned to excite at 283nm and the resulting chemiluminescence acquired at 305nm. In the case of the formaldehyde PLIF imaging, the laser sheet was used to excite the air-diluted biacetyl molecules at a wavelength of 355nm with the resulting chemiluminescence imaged at a similar wavelength of 353nm.

It is worthwhile to acknowledge the debate in the literature on the adequacy of the various heat release rate markers. The V shaped flame studies of Vagelopoulos and Frank [22] suggest the CH* fraction does not track the heat release rate particularly well when the flame varies from rich to lean and also when applied for flame front track purposes. Yi and Santavicca [23] also suggest the CH* chemiluminescence should limited in flame edge detection application. In the very recent OH* PLIF investigations of Tachibana et al. [24] the heat release rate response is observed to be linearly dependent on the amplitude of velocity oscillations. The flame surface area oscillation were verified as exhibiting a similar response to the OH* based heat release rate measurements.

The preponderance of extensive studies including the very recent works of Pater [5], Nair and Lieuwen [25], Palies [26-27], Bellows [28], Fritsche [29], Noiray et al. [30-31], Lawn [32], Li [33], Fanaca [34] represent thermoacoustic instability studies utilizing either CH* or OH*

chemiluminescence. There thus appears to be a wide consensus in the literature that these heat release rate markers represent the leading edge of flame heat release rate quantification and imaging methods.

A critical tool in the literature for assessing the flame response is the flame transfer function relating the heat release rate (*q'*) and velocity (*u'*) perturbations normalized by their respective mean values:

$$FTF = \frac{q'/\bar{q}}{u'/\bar{u}} \tag{2.2}$$

A fundamental understanding of the processes that drives thermoacoustic instabilities is essential to preventing their occurrence in the modern lean premixed mode gas turbines. A means to achieve this is to investigate various acoustically perturbed atmospheric flame configurations at the laboratory scale for an understanding of the conditions and parameters critical to initiating thermoacoustic instabilities. The existing literature is extensive and extends over on a multitude of flame configurations to include, bluff body stabilized, perforated plate, and swirl stabilized flames.

2.1.1 Bluff Body Stabilized Flames

The existing literature on bluff body stabilized flames is dominated by premixed flame configurations motivated by the lean premixed mode gas turbines prevalent today (2010). The

generation of Kelvin Helmholtz and Bernard Von Karman vortices along with some phase jitter is reported by Shanbhogue and Lieuwen [13] for acoustically pulsed bluff body stabilized flames at peak vorticity locations. Other recent studies on bluff body stabilized flames include the experiments of Nicoud, Durox, Chaparro, Shanbhogue and Kim among other authors [15-19, 25-26]. The gain of the transfer function is observed to be greater than unity for high amplified flame responses. The gain is also observed to be dependent on the amplitude of the acoustic perturbations, decreasing with increasing perturbation amplitudes. The accompanying transfer function phase for the bluff body stabilized flame is observed to be relative independent of the amplitude of forcing [15]. The flame transfer function (FTF) phase is observed to be linearly increasing with frequency similar to the observation of Durox et al. [15-16] and Chaparro et al. [19] for a variety of bluff body flame geometries including flat, conical, V and M shaped flames.

The experimental investigations of Durox et al. [15-16, 18] on premixed bluff body stabilized V-flames illustrate the burner Helmholtz resonance modes activated by acoustic excitation and heat release coupling. The power from acoustic forcing at resonant modes must balance losses from damping and far field radiation as similarly observed by Lieuwen and Preetham [3, 10]. Higher amplitude responses were confined to forcing frequencies below 200Hz corresponding to Strouhal numbers (*St*) in the 1-2 range, or generally on the order of unity. The Strouhal number [15-19] represents forcing frequencies (f_p) in non-dimensional form and is defined as:

$$St = \frac{uf_p}{D} \tag{2.3}$$

The velocity at the burner exit (u) and a representative length scale such as the burner diameter (D) is used in the non-dimensionalization of the forcing frequencies (f_p). A low pass filter response is generally observed for the various bluff body stabilized flame geometries. The V shaped flames are observed to be strong amplifiers compared to flames with alternative flame geometries such as the M or conically shaped flames. This result is consistent across the premixed methane-air flames of Durox et al. [15-16] and the propane-air flames of Chaparro et al. [19].

The bluff body stabilized flames characterized by large amplitude responses are observed to exhibit a positive Rayleigh index as expected. As the Rayleigh index relates heat release rate (q') and pressure (p') oscillations, the positive Rayleigh index is indicative of in-phase q' and p' perturbations. Durox et al. [15-16] demonstrates that velocity (u') to heat release rate (q') perturbations with a phase in the π-2π range is required in addition to a positive Rayleigh index for the occurrence of significant amplification in the flame response. The optimal amplification is observed for u'-q' phase angles of $3\pi/2$ along with a positive Rayleigh index. The third requirement proposed by Durox et al. [15] for the initiation of thermoacoustic instabilities in their bluff body stabilized flame configuration is a quadrature ($\pi/2$) phase relationship between the internal burner pressure (p_1') and external acoustic pressure (p_2') perturbations.

The mechanisms associated with flame blowoff are also of importance as thermoacoustic instabilities may potentially lead to flame extinction in cases of unbounded increasing amplitude oscillations. Several studies to examine the blowoff dynamics of bluff body stabilized

flames include the works of Nair and Lieuwen [25] and Chaudhuri et al. [35-36]. Nair and Lieuwen [25] suggest that the average flame strain rate need not correspond to the extinction strain rate for blowoff to occur. Instead, the blowoff event is precipitated by large scale time-localized extinction events of sufficient amplitudes leading to irrevocable extinction. Chaudhuri et al. [35-36] suggest that flame extinction is observed to occur with higher frequency heat release rate (q') oscillations are a precursor event to extinction. The bluff body stabilized flames of Chaudhuri et al. employ spatial gradients in heat release due to their potential for lower NOx emissions without and associated increase in CO while maintaining the overall burning rate [37].

2.1.2 Swirl Stabilized Flames

The improved mixing necessary for more complete combustion and higher heat release is typically achieved by addition of a swirling motion to the incoming reactants in the combustion chamber. A swirler composed of turning vanes or tangentially directed air supply ports are two of the typical modes by which the swirling motion is imparted to the incoming reactants.

The swirl intensity imparted into the flow is defined by the swirl number(*S*). It is a quantification of the tangential momentum imparted to the axially directed flow by the swirl generating mechanism (swirler vanes or tangential air ports). A geometric swirl based on the burner dimensions is utilized by Khannah [4] for a burner with a swirl vane configuration. The premixed swirling flame dynamics studies of Bellows et al. [28] show strong forcing amplitude dependence between heat release rate (*q'*) and pressure (*p'*) oscillations. The velocity (*u'*) and

pressure (*p'*) relationship is observed to be linear with constant phase for the premixed flame. The gasdynamics represented by the u'-p' relationship is also considered to play less of a role than the p'-q' relationship in the premixed flame configuration in their study. Four primary phenomena are observed as prevalent in the swirling flame response to acoustic perturbations. These include the equivalence ratio, global extinction, chemical kinetics and flame holding height.

Several other definitions of the swirl number based on the axial and tangential velocity distributions exist in the literature [38]. In the present study, the swirl number definition utilized is the prevalent definition in literature by Ribeiro and Whitelaw [39]:

$$S = \frac{\int_{R_i}^{R_o} r^2 uw dr}{R_o \int_{R_i}^{R_o} r\left(u^2 - \frac{1}{2}w^2\right) dr} \tag{2.4}$$

For the present investigation, the velocity components are defined in a symmetric plane containing the burner axis. The axial velocity (*u)* denotes the components directed downstream from the burner exit. The tangential velocity (*w*) is directed in the azimuthal direction tangent to the burner circumference. These swirl stabilized flames are considered less susceptible to instabilities in comparison to their bluff body counterparts. However, the desire for leaner combustion modes means thermoacoustic instabilities still represent a fundamental issue to be addressed. As was the case in the previous discussion on bluff body stabilized flames, a preponderance of existing literature on swirl stabilized flames is related to premixed flame configurations.

The primary stabilization mechanisms in swirling flames include the flow divergence mechanisms of Chan [40] and the more common internal recirculation zone (IRZ) configurations of Fick et al. [41], Paschereit et al. [42], Umemura et al [43] and Kulsheimer et al. [44] among others. Umemura and Owaki [43] find the competition between the swirl and heat release rate are the critical mechanisms behind the flame propagation. Kulsheimer [44] finds a $Pu \approx 1/St$ relationship a necessary condition for the initiation of a premixed swirling flame response where the mass flow rate of the fuel-air mixture is modulated. The pulsation amplitude (*Pu*) was defined as the ratio of the rms to mean mass flow rate of the fuel-air mixture modulation, with *St* defined as the Strouhal number.

Entrainment of ambient air and vortex rollup are observed to be also significant influences on measured flame transfer functions and the general flame response [44 -45]. The premixed swirl stabilized flames of Paschereit et al. [46] exhibit amplification with the flame as an acoustic source in the 40Hz–160Hz range. This result is analogous to the previously presented observations in bluff body flame studies [15-19] of strong responses below 200Hz,. This response characteristic is also observed in the swirling flame response of several authors where amplification is observed for Strouhal numbers on the order of unity [4, 26-27, 47-48].

The experimental studies of Khannah [4] comparing flat laminar and swirl flames also reveal an 8th order low pass filter response for fully premixed swirling flame configurations with OH* chemiluminescence as the heat release rate marker. The effects of acoustic pulsing on the

flame dynamics were observed in the 20Hz-400Hz range, with the most significant effects on the flame occurring with acoustic pulsing in the 20Hz-100Hz. Minimal effect of acoustic perturbation were observed above an equivalence ratio of 0.6 with methane as the fuel. Freitag et al. [47] attempt to investigate the pressure dependence of flame transfer functions for premixed swirling flames subjected to 1-5bar pressures. A power scaling effect on the flame transfer function was observed with the largest effect at higher frequencies.

The extensive studies on the impact of acoustic forcing amplitudes on the flame transfer function of premixed swirling flames by Palies et al. [26-27] result in the definition of the Flame Describing Function (FDF). The FDF represents a family of curves, with each curve representing the flame transfer function for a specific forcing amplitude. The gain of the FDF is observed to be more dependent on forcing amplitude in comparison to the FDF phase curves which are observed to be linearly increasing with frequency. This result is analogous to the previous observations by Durox et al. [15-16] and Chaparro [19] for premixed bluff body stabilized flames where a similarly linear phase dependency with frequency and minimal dependence of the phase on the amplitude of acoustic forcing was observed.

The flame response to acoustic forcing in premixed swirling flames is observed by Palies et al. [27] to be controlled two primary mechanisms:

- The propagation of axial velocity perturbations (u') at the speed of sound (c)
- A vortex wave generated by the swirler producing azimuthal velocity (w') perturbations. These azimuthal velocity perturbations are convected at the bulk axial velocity (U).

The identification of the convective and acoustic mechanisms improve on the sound propagation observations by Golubev and Atassi [48]. The splitting of the disturbance velocity into vortical and potential parts in a potential swirl model showed that pressure modes are governed by single homogeneous convective wave equation for the velocity potential. Palies et al. show that the induced axial and azimuthal perturbations lead to swirl number fluctuations with acoustic pulsing. These swirl intensity oscillations generate a mode switching mechanism that governs the response of the swirling flame to the incident acoustics.

In analyzing the response of swirling flames, several authors introduce the analogy of the electrical impedance known as the acoustic impedance (*Z*) at the burner-flame interface [35, 39-40, 49-50]. The acoustic impedance is the complex frequency spectra of the ratio of acoustic pressure (p') and the volume velocity (*v*). The "acoustic" refers to the oscillating component of pressure [51-54]:

$$Z = \frac{p'}{v} \tag{2.5}$$

For the case of a stagnant fluid medium the volume velocity similarly corresponds to the velocity oscillations which accompany the acoustic pressure. Several methods of determining the acoustic impedances of various cylindrical are presented by Dickens et al. [55]. *Re(Z)* represents the real component of the acoustic impedance and is referred to as the *resistance* component representative of the dissipative nature of the flame response. *Im(Z)* is the referred

to as the reactance and is a measure of the incident acoustic energy conversion through various forms including periodic rarefaction and compression [53-55].

Bellows et al. [28] characterize the flame response of a swirling premixed flame as a classic nonlinear duffing oscillator. The previously discussed studies by Noiray et al. [30-31] also extensively utilize the acoustic impedance concept for premixed perforated plate flames dynamics experiments. As was the case in bluff body stabilized configurations, flame surface are losses induce heat release rate and pressure perturbations from the accompanying acoustic sound generation. Flame responses are divided into two broad categories based on the acoustic impedance. These include flames with negative resistances i.e., $Re(Z)<0$, corresponding to amplifying acoustic source flames with active, energy producing responses. Passive energy dissipating flame configurations are characterized by positive resistances i.e., $Re(Z)>0$.

2.1.3 Non-Premixed Flames

A majority of the previously discussed literature on swirl stabilized flames is once again primarily focused on premixed flame configuration as was the case in the bluff body stabilized flame literature. However, the non-premixed flame studies in the literature illustrate similarities to reported observations in premixed flame configurations. Huang and Yen [56] report three characteristic non-forced flame modes including a weak swirling flame (S=0.316, Re = 364), lifted flame (S=0.541, Re=1000) and turbulent reattached flame (S=0.596, Re=1700). The dominant flames modes are directly related to the swirl intensity. The direction of rotation in the inner recirculation zone vortices is observed to alternate between the various flame

modes. Inward rotating IRZs characterized the turbulent reattached and weak swirling flames with the outward rotating IRZ characteristic of the lifted flame regime. The enhanced mixing effect at high swirl is observed to significantly shorten the flame length accompanied by an increase in the flame width.

Juniper at al. [57] report a coupled oscillatory behavior for non-premixed round jet diffusion flames subjected to acoustic forcing. The diffusion jets were observed to lock into the forcing frequencies at sufficiently high amplitudes. The reported oscillatory behavior is similar to the reported oscillatory flame response characterized by a negative *Re(Z)* reported by Bellows et al. [28] for premixed swirling flames and Noiray et al. [30-31] for perforated plate flame configurations.

Extinction studies on non-premixed flames suggest that blowout limits for swirling configurations can be predicted using the Damkohler number (*Da*) defined as the ratio of characteristic chemical and convective time delays [58-59]. A similar Damkohler dependence was previously reported by Fritsche et al. [29] for swirling premixed flames. Unstable flames were also observed to be isolated by a lean boundary delineated by a minimum adiabatic flame temperature and a rich boundary marked indicated by critical Damkohler number. This inference is supported by Koutmos et al. [60] and Leuckel et al. [61] where local extinction events in non-premixed, non-swirling flames are predicated on *Da* numbers below a critical value.

2.2 Analytical and Numerical Investigations

Thermoacoustic instability models for the prediction of the flame response to acoustic perturbations have been develop by a variety of authors typically based on the G surface definition of Markstein [62-63]. The analytical flame response to velocity oscillations is observed to be dependent on the *flame* Strouhal number and the *flow* Strouhal number. The laminar burning velocity is used in the flame Strouhal number definition and the bulk velocity is utilized in the flow Strouhal number definition by Fleifil et al. [64].

Generalized analytical thermoacoustic instabilities models based on the flame surface area oscillations are developed for non-swirling premixed conical, M and V shaped flame geometries by Schuller et al. [63]. A non-dimensional frequency analogous to the flow Strouhal number of Fleifil et al. [64] is observed to be a critical parameter in the flame transfer functions. The flame surface is represented as an isosurface and the flame surface area used as a marker for heat release rate oscillations [63-69].

In the laminar flames studies, high frequency velocity oscillations were found to pass through the flame with minimal effect on heat release rate, while low frequency perturbations initiated significant response in the flame heat release rate. The developed analytical V shaped flame response was characteristic of a low pass filter with strong amplification for even moderate acoustic forcing amplitudes. The incident acoustic perturbations generated large amplitude periodic motions in the flame inducing flame surface area variations and associated cyclic heat

release rate oscillations. As observed on the experimental flame response studies, intense sound emissions (pressure oscillations) are generated from the localized annihilation of the flame sheet.

Huang and Yang [70] carried out a large eddy simulation (LES) based numerical study of flame dynamics in a lean-premixed, swirl-stabilized combustor, establishing the inlet temperature and equivalence ratio as primary parameters related to combustor stability. Energy interactions between combustion zone chemistry and acoustic oscillation in the chamber were found to be characterized by a feedback closed-loop coupling between combustion chamber acoustics, the fluid dynamics of vortex shedding and heat release rate oscillations. An aggregate estimate by Lieuwen [2] of these energy interaction/feedback timescales based on premixed flame speeds and thicknesses led to timescales of the order of 0.002 – 0.07s for methane/air flames. This established the likelihood of prominent flame response to acoustic perturbations in the 20 to 500Hz frequency range associated with these time scales. This low frequency range is in agreement with the highly responsive acoustic forcing configurations reported in several of the previously discussed experimental and analytical investigations.

The analytical premixed flame response study of Cho and Lieuwen [67] reveal several mechanisms behind the flame response. The flame speed and flame surface area fluctuations are observed to lead to equivalence ratio perturbations that govern the flame response. The analytical models of You et al. [68] also exhibit a negative phase relationship between the heat release rate and velocity oscillations for the occurrence of flame amplification. This is in keeping

with the Rayleigh criteria report for the previously discussed flame configurations. The flame liftoff height which decreased with increasing swirl intensity is also observed to be critical in the numerical simulation of a swirling premixed flame response.

2.3 Isothermal Swirling Fluid Mechanics

The early investigations into the fluid mechanics of swirling jets include the works of Ribeiro and Whitelaw [39] as well as Syred and Dahman [71] among others. Several of these studies reveal the well known expansion of the internal recirculation zone (IRZ) with increasing swirl intensity and the accompanying enhancement of flame stabilization. In premixed configurations identified as more susceptible to instability, vortex shedding as well as the area ratio between the air supply port and the combustion chamber are found to be critical influences on the observed fluid mechanics and associated flame dynamics [72-73]. These isothermal flow field measurements are typically carried out using the well known Particle Image Velocimetry (PIV) technique. PIV is a well known flow field visualization approach that has been successfully applied to a variety of fluid flow configurations including swirling water jets, turbomachinery as well as the swirling flow configuration of interest in the present effort [73-77].

Particle Image Velocimetry (PIV) studies of unconfined swirling flames by Gupta and Archer [74] reveal strong similarities between the isothermal flow field measurements and those conducted under hot (flame present) conditions for an unconfined swirling configuration. However, combustion is observed to increase the flow field velocity magnitude. Increased

entrainment and radial expansion of the flow field is also reported with combustion. This observation is corroborated in the previously discussed confined swirling flame PIV measurements of Fanaca et al. [34].

Al-Abdeli and Masri [77] report elevated axial-azimuthal (*u'w'*) shear stresses in swirling flame configurations. The onset of the downstream recirculation zone was observed to be not necessarily dependent on the attainment high swirl intensities. As a example, conditions favorable to IRZ formation were achieved with a combination of low swirl intensity and high axial velocity. However, for a constant axial velocity (mass flow rate) the formation of the inner recirculation zone is observed to occur at intermediate rather than high swirl intensities. In additional to a lateral spread of the flow field with increasing swirl, Zhang et al. [78] report the swirling jet as characterized by a precession vortex core (PVC) and an M-shaped axial velocity profile with increased swirl.

Increased turbulent kinetic energy (TKE) is reported at higher swirl intensities for the acoustically forced swirling jet configuration of Alekseenko et al. [79]. The TKE increase was found to be a strong function of the amplitude of acoustic forcing particularly for the non-swirling and low swirl intensity jets. Minimal effects on the jet structure were observed with similar amplitude acoustic forcing at higher swirl intensities. For a similar unforced swirling jet configuration, Giannadakis et al. [38] report intense momentum transfer between the inner and outer shear layers as quantified using the skewness values. Two primary zones are

identified in the flow field including the previously discussed recirculation zone immediately downstream of the burner exit dominated by the IRZ bubble. A secondary zone aft of the IRZ bubble is found to be dominated by wake flow characteristics. The Rossby number is utilized in characterizing the observed fluid mechanics.

An increase in the turbulence intensity at higher swirl is reported by Al-Abdeli [77] and Alekseenko [79]. The PIV and Large Eddy Simulation (LES) studies of Maciel et al. [80] illustrate the existence of the IRZ at moderate swirl intensities. Above a critical Swirl number, the IRZ ceases to exist and vortex breakdown occurs accompanied by a significant change in the jet characteristics. The flow at the pipe exit is dominated by helical instabilities leading to large scale cortex structures (LSVS) in up to triple helix configurations similar to the observations of Cai et al. [81]. LES analyses of an isothermal swirling flow configuration by Shanwu et al [82] also illustrate the presence of Kelvin-Helmholtz (KH) and helical instabilities. The presence of these KH instabilities has also been reported under hot (flame present) conditions by Shanbhogue and Lieuwen for bluff body stabilized flames.

The previously discussed LES studies on isothermal jets reveal the prevalence of the LES methodology in the inert fluid mechanics modeling literature on swirling jets. The very recent LES analysis of isothermal swirling jets in a tangential supply configuration by Dinesh and Kilpatrick [83] suggest the precessing vortex core phenomena is significant even at lower swirl intensities. The alternative Direct Numerical Simulation (DNS) based investigations of Siamas et al. [84] are characterized by perturbed swirling jets with two concentric shear layers and the

expected inner recirculation zones. In general the isothermal investigations allow the isolation of physical phenomena critical to the flame response including vortex shedding, vortex breakdown at higher swirl, large scale vortex structures (LSVS) and intermittency of fuel injection in non premixed configurations [85].

CHAPTER 3 EXPERIMENTAL AND ANALYSIS METHODS

3.1 Experimental Approach

The swirl stabilized non-premixed atmospheric burner used in the study is illustrated in Figure 3.1. Research grade propane is delivered through the central fuel pipe of inner radius 0.46cm. Surrounding the fuel pipe is a co-flow annulus of outer radius, R_o = 2.54cm through which the main axial air is supplied. Six 1cm-diameter ports are circumferentially spaced 3.5cm below the exit plane of the burner through which tangentially directed airflow is supplied to induce swirl in the main axial air flow. The amount of swirl imparted to the main axial flow is quantified by the Swirl Number (*S*) which is determined using the integral relationship in Eq. 2.4 where *u,* v and *w* are the axial, radial and tangential velocities respectively. R_i (0.48cm) and R_o (2.54cm) are the radii of the inner and outer walls of the burner co-flow annulus.

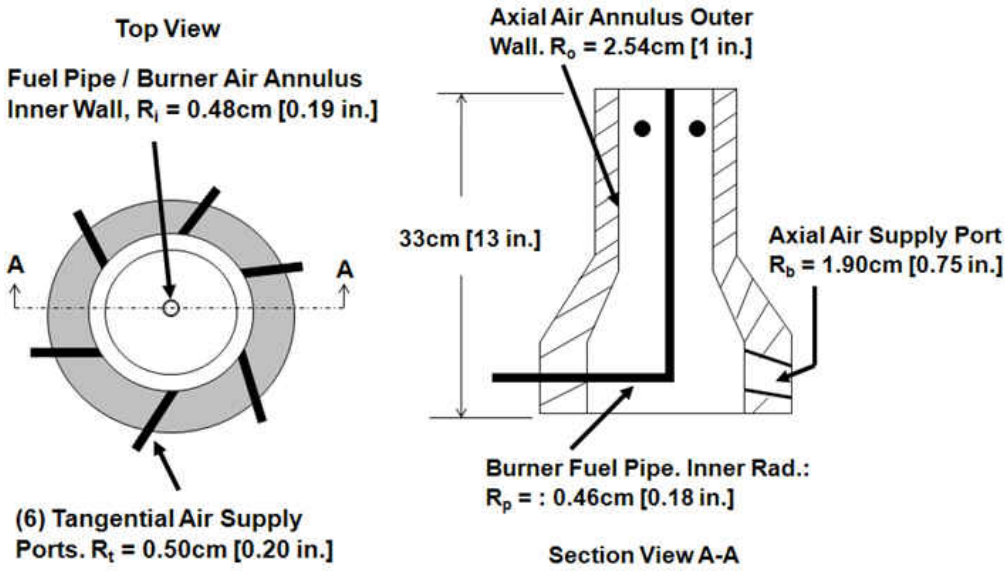

Figure 3.1: Non-Premixed Burner Geometry

The experimental set-up for the combustion dynamics and isothermal PIV study is illustrated in Figure 3.2. Honeycomb flow conditioners are employed in the burner annulus to straighten the co-flowing axial air supply. The equipment utilized includes a Brooks Instrument mass flow controller (Model 5851E with Card Edge Connector) for propane supply through the central fuel line. The velocity at the exit of the burner (u) is measured using a Constant Temperature Anemometer (CTA) system (TSI Model IFA300) fitted with a hot wire (3.8μm diameter) probe. The CTA probe location is selected to be close enough to the flame to pick up the flame dynamics but not exceed the temperature rating of the tungsten probe (300^{o}C). The spatial location of the probe is 0.8cm above the burner exit and 1.3cm from the axis of the burner.

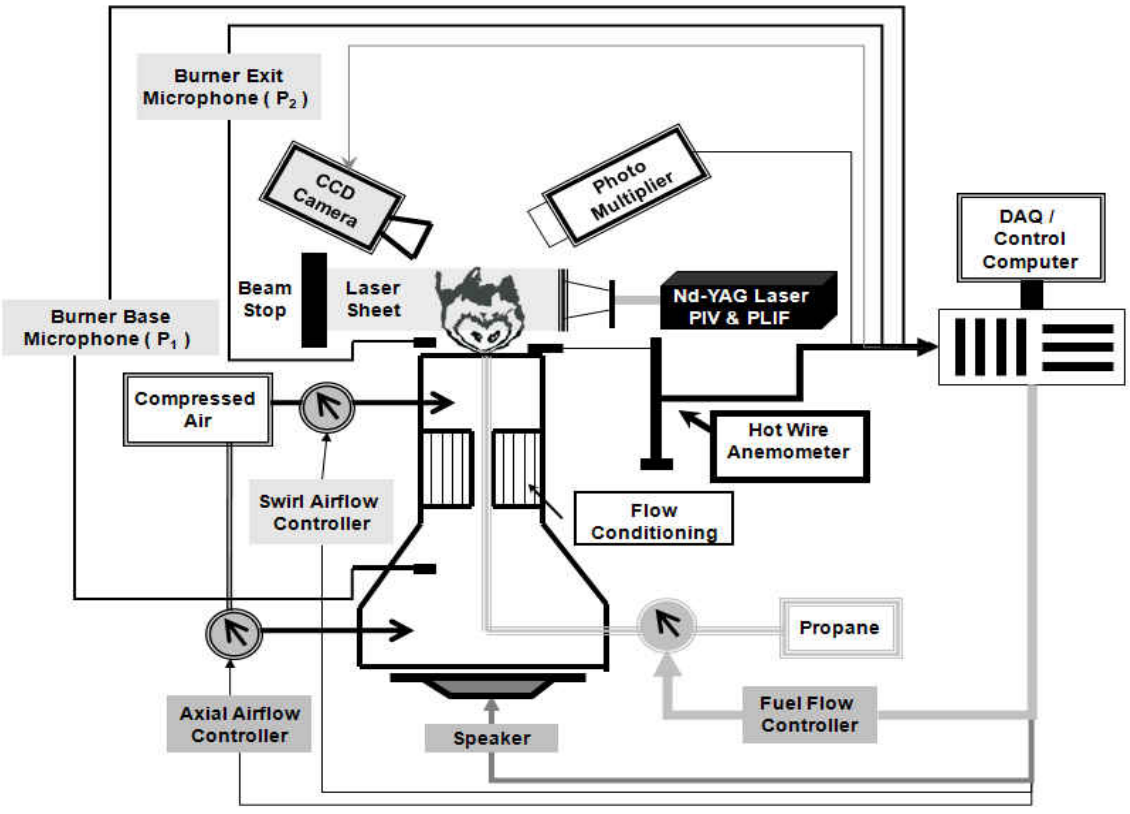

Figure 3.2: Combustion Dynamics and Isothermal PIV Experimental Setup

The heat release rate signature of the flame (q) is detected using a photomultiplier (PMT) tube (Hamamatsu Model H9307-02) with a detection range of 185nm – 900nm. Along with the PMT, flame images during the combustion process are simultaneously obtained using a CCD camera (LaVision Imager Intense Model). The photomultiplier (PMT) and CCD camera are fitted with 430nm ±10nm bandpass filters for the detection of CH* chemiluminescence which is used in the absence of mixing data as a heat release rate marker.

Two 0.635cm (1/4in.) microphones (PCB 130D20 ICP model) are used for measuring the dynamic pressure perturbations at the base of the speaker (p_1') and 1.3cm above the burner exit (p_2') radially opposite from the CTA probe (1.3cm from the axis of the burner). Acoustic perturbations are generated using a loudspeaker (200W Boss Audio BL3250) located at the base of the burner.

The Particle Image Velocimetry (PIV) technique is used for cross comparison of the isothermal flow field associated with the investigated flame configurations. This is in order to isolate the fluid dynamic components of the flame response observed in the combustion dynamics experiments. The Particle Image Velocimetry system is composed of a Litron Nano Nd:YAG pulsed laser providing a 70mJ/pulse 532nm laser beam which is passed through an optical setup to create a laser sheet at the mid plane of the burner.

Di-Ethyl-Hexyl-Sebacat (DEHS) is used as the seeding medium in the fuel, axial and tangential air lines. DEHS is a non soluble, colorless and odorless liquid with 0.3 μm diameter droplets having

an average lifetime of approximately 4 hours . The PIV images are acquired using a CCD camera (LaVision Imager Intense Model) phase-locked to the acoustic pulsing signal with a 100μs delay between successive frames of each PIV image. The 1376 pixels x 1040 pixels PIV images are acquired at a rate of 2 images a second and analyzed using LaVision Davis software routines based on 32 by 32 interrogation windows with 50% overlap.

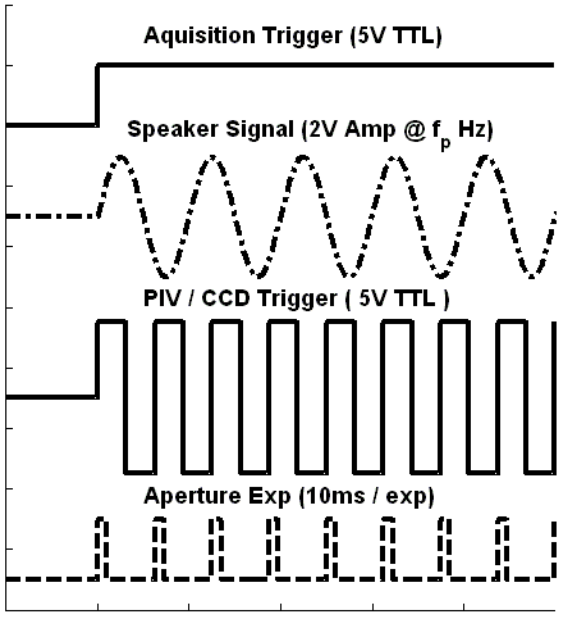

Figure 3.3: Experimental Phase-Locking and Trigger Timing Diagram

The CCD camera in the combustion dynamics and PIV study is externally triggered using the National Instruments LabView data control and acquisition system relative to the speaker signal. As a result, the PIV images, CH* chemiluminescence images, velocity, pressure and PMT (heat release rate) signals are all phase-locked to the sinusoid acoustic pulsing signal of frequency f_p. A master trigger simultaneously activates the acoustic perturbation signal, laser pulse and CCD image acquisition trigger (5v TTL) signal designed to account for the internal camera delays associated with image capture. The CH* chemiluminescence images are

acquired at a rate of eight images per second with a 10ms aperture exposure initiated on the low-to-high transition of the CCD TTL trigger. Figure 3.3 illustrates the timing sequence associated with the combustion dynamics and isothermal PIV experiments.

The experimental dataset is composed of the burner base and exit dynamic pressure perturbations (p_1' and p_2'), the burner exit velocity (u) from the CTA, heat release rate intensity via the photomultiplier (q), fuel flow rate (m_{fr}) and the associated CH* chemiluminescence and isothermal PIV images. Experimental data is acquired over a sampling period (t_P) of 14 seconds at a sampling rate of 50kS/s.

Table 1: Combustion Dynamics Test Cases

CASES	Mass Flow Rates [mg/s]			Average Velocities [m/s]		Swirl Number (S)	Reynolds Number [/] ($R_e=\rho U_{avg} d_m / \mu$)
	Propane (m_{fb})	Axial Air ($m_{a,a}$)	Tang. Air ($m_{a,t}$)	Axial Air Only ($U_{avg,a}$)	Combined Air Sources (U_{avg})		
S009	37.93	3436	1027	1.569	1.75	0.09	2662
S034	37.93	3348	1773	1.528	2.00	0.34	3043
Fuel Used: Propane. R_e Based on Mean Burner Dia., d_m = 0.0254m [1 in] R_e Computed for Burner Annulus Isothermal Configurations @ Ambient (300K) Conditions							

3.2 Experimental Test Cases

The baseline experimental flow conditions used in the present study are described in Table 1. Specifically, two swirl intensity levels are studied: S = 0.09 and 0.34. These respectively correspond to increasing Reynolds numbers of 2662 and 3042 based on the average velocities (1.75 m/s – 2 m/s) at the burner exit and mean burner diameter, d_m. In the present article, each

case is designated using its swirl number prefixed with an "S." for example the S=0.09 case will be subsequently referenced as the S009 case. Increasing swirl intensity is analogous to increasing the air flow through the tangential ports and momentum transfer from the tangential air supply is also dependent on the co-flowing axial air flow rate. Using the S009 case as a baseline, the axial air flow rate is relatively constant while the tangential airflow is significantly increased to attain the S034 case as illustrated in Table 1.

Table 2: Test Case Subsets – Fuel Flow Rate Variation

	Fuel Flow Rate[a] (m_f)
C1	$m_f = m_{fb}$
C2	$m_f = 0.4 m_{fb}$
C3	$m_f = m_{fb}(\hat{\lambda})^{2t}$

[a] m_{fr} is baseline fuel flow rate from Table 1
[b] $\hat{\lambda}$ selected to achieve $0.1m_{fr}$ at end of 14 sample period ($\hat{\lambda}$<1)

In addition to the swirl intensity variations in the baseline cases in Table 1, the effect of changing equivalence ratio at constant swirl intensity levels on the flame response is also examined. For each baseline case described in Table 1, three fuel flow rates (C1, C2 and C3) are used to investigate the impact of equivalence ratio variations on the flame response. These fuel flow rates are described in Table 2 and involve modifying the fuel flow rate (m_f) relative to the baseline value (m_{fb}) described in Table 1. The fuel flow rate in the C2 case is selected to be 40% of the fuel flow rate of the baseline (C1) case. Although non-premixed flames are exclusively studied in this article, the C1 and C2 nomenclature will be respectively referred to the "rich" (C1) and "lean" (C2) flame configurations. As illustrated in Figure 3.4, the fuel flow rates are

held constant during the experiment over the 14s sampling period for the C1 and C2 flame configurations.

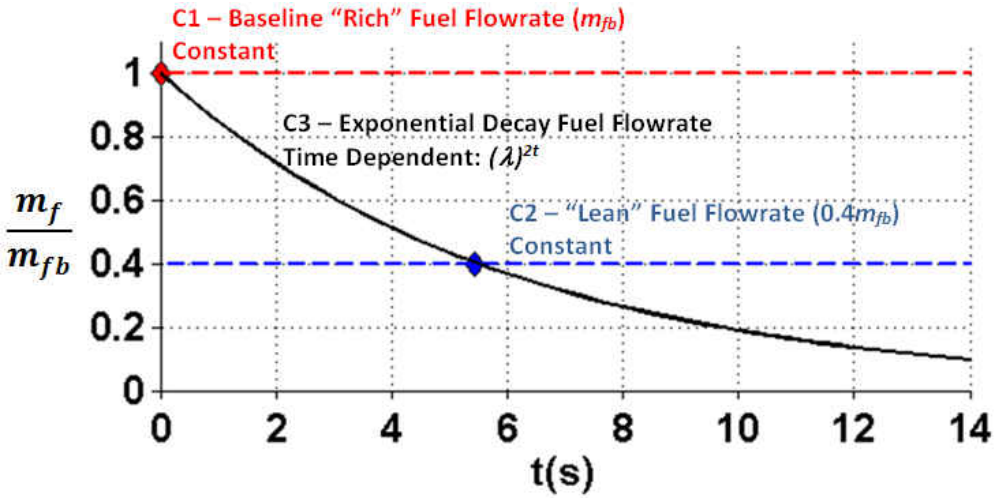

Figure 3.4: Fuel Flowrate Settings

For the C3 fuel flow rate condition, an exponential decay function is used to decrease the fuel supply over the 14s experiment sample period. As illustrated in Table 2, the decay constant (λ) for the fuel flow rate decay function is selected to yield 10% of the baseline (maximum) fuel flow rate at t=14s. The 10% of baseline fuel setting is experimentally selected to ensure complete extinction of the flame for all the various swirl intensity configurations in the present study. The flame response investigations are carried out for several acoustic forcing frequencies (f_p) from 0Hz in the unpulsed mode through 315Hz as described in Table 3.

Table 3: Acoustic Pulsing Frequencies

Index	f_1	f_2	f_3	f_4	f_5	f_6	f_7	f_8
f_p (Hz)	0	105	123	167	201	257	283	315

3.3 Analysis Methods

This section details the methods used in the analysis of acquired flame dynamics data. These techniques include phase-conditioning, coherence and transfer function analysis as well as the acoustic impedance technique. The details of these methods are subsequently discussed.

3.3.1 Phase Conditioned Flame Dynamics

The experimental data set is primarily analyzed based on a phase conditioning of the measured heat release rate (q'), burner exit velocity (u'), burner base (p_1') and exit (p_2') pressure perturbations. The phase angle (ϕ) associated with a data sample acquired at time instant, t is determined using the acquisition time of the data sample relative to the acoustic pulsing frequency (f_p) by:

$$\phi = modulo(2\pi f_p t, 2\pi) \tag{3.1}$$

This allows the acquired flame dynamics perturbation signals to be phase conditioned relative to the acoustic pulsing frequency (f_p). Several samples at a specific phase angle are acquired over the experimental sampling period requiring a phase conditioned average of the associated flame dynamics. The number of samples acquired over the experimental sampling period at the specific phase angle (ϕ) is designated as n. This phase conditioning technique is applied to the all components of the experimental data set. As an example, the phase conditioned velocity perturbation ($u'_{avg,\phi}$) and its normalized equivalent $\langle u' \rangle$ at a specific phase angle (ϕ) are determined by:

$$u'_{avg,\phi} = \frac{\sum_{i=1}^{n} u'_{i,\phi}}{n}, \ \langle u' \rangle = \frac{u'_{avg,\phi}}{u_{avg,fp}}$$

(3.2)

The phase conditioned data over various phase angles from ϕ = 0 through ϕ = 2π allows the flame dynamics to be analyzed for the amplitude response and phase difference between the various components of the experimental data set as well as relative to the supplied acoustic pulsing signal. A normalized amplitude response due to acoustic perturbation at a specific pulsing frequency is estimated by (using the velocity as an example):

$$|\langle u' \rangle| = \left| \frac{u'_{avg,\phi}}{u_{avg,f_p}} \right| = \frac{1}{2} [max\langle u' \rangle - min\langle u' \rangle]$$

(3.3)

The normalization variable ($u_{avg,fp}$) in Eq. (3) and Eq. (4) is the time averaged velocity across all phases at forcing frequency (f_p). The time-average is carried out across all phases using the time trace of the velocity, $u_{fp}(t)$ at a specific pulsing frequency:

$$u_{avg,fp} = \frac{1}{t_p} \int_0^{t_p} u_{f_p}(t)\, dt$$

(3.4)

This procedure is repeated for the burner base (p_1') and exit (p_2') pressure as well as heat release rate response (q') perturbations associated with the observed flame response. The phase difference between components of the flame dynamics is also estimated using the Fast Fourier Transform of the observed perturbations. As an example, at a specific pulsing frequency (f_p), the phase difference ($\phi_d^{\,p1'-u'}$) and time delay ($\tau_d^{\,p1'-u'}$) between the burner exit velocity (u')

(considered as the output) and the burner base pressure (p_1') perturbations (considered the input) are estimated as:

$$\phi_d^{p_1'-u'} = atan\left[\frac{F(u',f_p)}{F(p_1',f_p)}\right],\ \tau_d^{p_1'-u'} = \frac{\phi_d^{p_1'-u'}}{2\pi f_p}$$

(3.5)

The complex value of the Fast Fourier Transform (FFT) of the velocity perturbation at the pulsing frequency is denoted by $F(u',f_p)$. This technique is also used in estimating the phase differences and time delays between the various flame response parameters. The intensity of velocity fluctuations (I_U) is estimated using the relationship:

$$I_U = \frac{1}{u_{avg,fp}}\left[\frac{1}{t_p}\int_0^{t_p}\left(u_{fp}(t) - u_{avg,fp}\right)^2 dt\right]^{\frac{1}{2}}$$

(3.6)

3.3.2 Coherence Analysis

The magnitude squares coherence (γ^2) function is a measure of the degree to which an output signal, *y* is caused by an input signal, *x*. It is determined using the complex cross-power spectral density (P_{xy}) and auto-power spectral density of the input (P_{xx}) and output (P_{yy}) signals [36]:

$$\gamma^2 = \frac{\left|P_{xy}(f)\right|^2}{P_{xx}(f)P_{yy}(f)} \qquad 0 \le \gamma^2 \le 1$$

(3.7)

An important use of the coherence function is the attribution of causality [4] between the input and output as (γ^2) approaches unity. Higher coherence values close to unity indicates that the output signal at a specific frequency is caused to a large degree by the input signal at the same

frequency. The degree of linearity as well as the noise levels inherent in the system dynamics can be subsequently evaluated. In the present work, the coherence function is utilized in assessing the degree of linearity (causality) between the various flame dynamics parameters.

3.3.3 Flame Lift off height and Surface Area Estimation

The flame surface area and lift-off height from the burner exit is estimated using a grayscale image intensity-based threshold technique. To estimate the flame lift-off height, the CH* chemiluminescence grayscale image intensity along the centerline of the flame (I_{CL}) is examined for the first pixel intensity beyond a threshold of 15% of maximum. Figure 3.5 illustrates sample centerline intensities for relatively richer and leaner flames as well as the location of the computed flame lift-off height (h_f). The richer flame is shown to be lifted from the burner exit (h_f = 0.51cm) and the leaner flame shown attached to the central fuel pipe (h_f = 0.00cm).

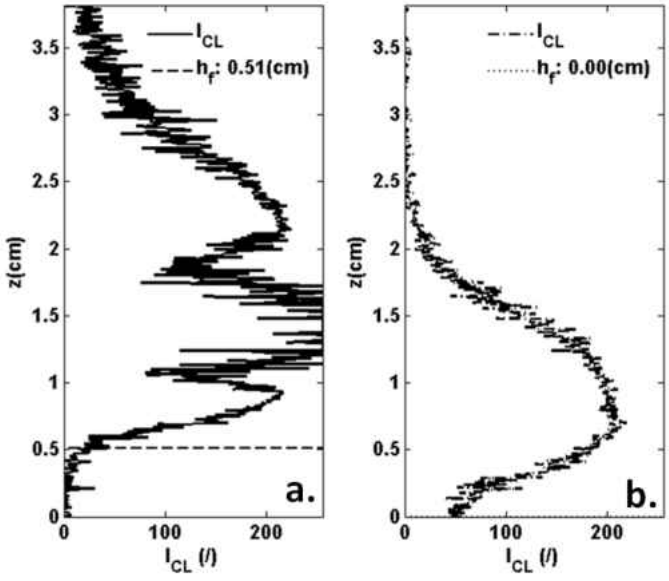

Figure 3.5: Flame Liftoff Height (h_f) Methodology (Sample Centerline CH* Intensity)
a. Lifted Richer (C1) Flame (h_f = 0.51cm) | b. Attached Leaner (C2) Flame (h_f = 0cm)

The 15% threshold was experimentally determined iteratively by comparing estimated flame lift-off heights with direct CH* chemiluminescence image estimates. The flame surface area is similarly estimated based on a grayscale image intensity threshold technique. Similar to the flame lift-off height estimation methodology, pixels in grayscale CH* chemiluminescence images with intensity values below the 15%-of-maximum threshold are assigned to the background of the image. Pixels with intensities exceeding the threshold are considered flame image pixels and are used to estimate the flame surface area using the size-to-pixel scaling factors

3.3.4 Flame Response Index Analysis

As discussed in section 2.1, the potential for instability in unforced flames is estimated using the Rayleigh Index (R) between the heat release rate (q') and burner exit pressure (p_2') perturbations. The Rayleigh index yields a positive value if the heat release rate and pressure perturbations are in phase as a necessary condition for the incidence of instability [4, 9-12]. Larger positive Rayleigh indices consequently indicate an increased susceptibility to instability. As the Rayleigh index is typically applied to unforced flames, an analogous *Flame Response Index* (R) is defined for use in the present study:

$$R = \int_0^{t_p} q'(t)\, p_2'(t)\, dt \tag{3.8}$$

The pressure at the burner exit (p_2') and the acquisition period (t_p) replace the corresponding parameters in the Rayleigh index formulation of Eq. 2.1. It is subsequently shown that the

Flame Response Index is a useful parameter in identifying highly responsive flame configurations. However, it is also shown that this flame response index is also an insufficient condition for completely isolating highly responsive flames.

3.3.5 Flame Transfer Functions

The application of acoustic forcing at a fixed frequency (f_p) generates pressure oscillations at the base of the burner (p_1'). These in turn lead to velocity perturbations (u') at the burner exit. The velocity perturbations and resulting burner exit pressure (p_2') perturbations interact with the flame to yield heat release oscillations (q'). The system dynamics between these flame dynamics parameters (u', p_2' and q') can be characterized using a transfer function as has been previously discussed [15-16, 35-37, 44-46].

The numerical investigations of Poinsot at al. [87] identify two primary techniques for obtaining the flame transfer function including:

- Harmonic Forcing – FFT Postprocessed Method (HF–FFT) Method:

  In this method, acoustic perturbations are supplied at a fixed frequency (f_p). The Fast Fourier Transform (FFT) is used to extract the flame heat release rate (q') response at the pulsing frequency (f_p) as measured with a photomultiplier (PMT). The flame transfer function *H(f)* is then assembled by forcing at a multitude of frequencies in the range of interest. The primary disadvantage of this method is the time-intensive nature required for acoustic forcing at several frequencies required for an accurate detailed transfer function.

- White Noise Forcing – Wiener-Hopf Postprocessed Method (WN–WH) Method:

  Acoustic perturbations are generated using a white noise signal containing frequencies below a cut-off value. The flame transfer function, *H(f)* is then generated using the Wiener-Hopf relation inversion. Assuming a system input *x(t)* and system output parameter *y(t)*, this inversion is essentially the complex quotient of the cross power spectral density (Φ_{yx}) of *x* and *y* and the power spectral density (Φ_{xx}) of *x*. Thus:

$$H(f) = \frac{\Phi_{yx}(f)}{\Phi_{xx}(f)} \tag{3.9}$$

  The power and cross spectral densities are the frequency domain transforms of the autocovariances and crosscovariances of the input and output signals. This method appears to be also referred to as the Blackman-Turkey approach in the flame transfer function studies of Chaudhuri et al. [36] for premixed flames with spatial mixture (equivalence ratio) gradients.

The harmonics forcing (HT-FFT) method is used in experimentally determining the flame transfer function in the present study. The measured transfer function is used to relate the scaled release (*q'*), velocity (*u'*), burner base (p_1') and burner exit (p_2') pressure perturbations that are experimentally measured. These perturbations are defined by the variations from the time-average of the respective parameter, i.e. for heat release perturbations (*q'*):

$$q' = q_{fp}(t) - q_{avg,fp} \tag{3.10}$$

In Eq. 3.31, $q_{fp}(t)$ represents that time trace of the heat release rate of a flame with acoustic forcing at frequency (f_p). The time average of the heat release signal of a flame subject to perturbations at frequency fp is designated as $q_{avg,fp}$. The respective perturbations are non-dimensionalized in the time domain as follows:

$$\hat{q} = \frac{q'}{q_{avg,fp}} \quad , \qquad \hat{u} = \frac{u}{u_{avg,fp}}$$

(3.11)

The time average is used to non-dimensionalize the heat release and velocity perturbations. As a result of the inherent non-linearity between the pressure and velocity, the pressure perturbations are non-dimensionalized using the nominal dynamic pressure, $(1/2)\rho u_{avg,fp}^2$ at the burner exit:

$$\hat{p}_1 = \frac{p_1'}{(1/2)\rho u_{avg,fp}^2} \quad , \qquad \hat{p}_2 = \frac{p_2'}{(1/2)\rho u_{avg,fp}^2}$$

(3.12)

The measured transfer functions are particularly valid if the system dynamics are linearly time invariant and one of the important objectives in this study is assessing the degree of linearity of the non-premixed flame dynamics.

Global, Mixing and Reaction Transfer Function Definitions

The system dynamics in a non-premixed burner are the result of the interaction between two primary processes. The first is the fuel/oxidizer mixing process related to swirl intensity induced by the relative flow rates of the co-flowing and tangential airstream in the burner. The second

primary process is the resulting combustion occurring in the flame and the subsequent feedback of hot products into fresh reactants in the inner recirculation zone.

In the present study three transfer functions are defined to study these inherent dynamics between the non-dimensionalized pressure, velocity and heat release perturbations:

- The *Reaction Transfer Function R(f)* relates the non-dimensionalized burner exit pressure (p_2') and resulting flame heat release (q') perturbations. The burner exit pressure and heat release perturbations are considered the system input and output respectively. The system dynamics primarily due to the combustion reaction occurring in the flame are captured by *R(f)*:

$$R(f) = \frac{\Phi_{\hat{q}\hat{p}_2}(f)}{\Phi_{\hat{p}_2\hat{p}_2}(f)} \tag{3.13}$$

- The *Mixing Transfer Function, M(f)* relates the velocity (u') and resulting pressure (p_2') perturbations at the burner exit. The mixing transfer function is defined to capture purely mixing dynamics from the tangential airflow interaction with the co-flowing air and the resulting mixing and recirculation at the burner exit. It is necessary to mention that the reaction transfer function does contain some feedback dynamics due to the reintroduction of hot combustion product gases with fresh reactants that naturally occurs inside the inner recirculation zone in a most swirl stabilized burners. The input and output of *M(f)* are the velocity (u') and resulting burner exit pressure (p_2') oscillations:

$$M(f) = \frac{\Phi_{\hat{p}_2\hat{u}}(f)}{\Phi_{\hat{u}\hat{u}}(f)}$$

(3.14)

- The *Global Transfer Function, G(f)* directly relates the burner exit velocity (u') and heat release (*q*) perturbations. *G(jω)* is defined to account for the global system dynamics once a velocity perturbation occurs at the burner exit through its impact on the flame heat release response. It may be considered a combination of the mixing and reaction transfer function. The velocity and heat release perturbations are considered the transfer function input and output respectively:

$$G(f) = \frac{\Phi_{\hat{q}\hat{u}}(f)}{\Phi_{\hat{u}\hat{u}}(f)}$$

(3.15)

3.3.6 Acoustic Impedance Estimation

The acoustic impedance (***Z***) is the complex ratio of the acoustic (oscillating component of) pressure and volume velocity as defined in Eq. 2.5. In the present study, the pressure perturbations (p_2') and velocity (*u*) at the burner exit are used in estimating the acoustic impedance using the frequency spectrum of the pressure-velocity quotient. As previously discussed and duplicated below for clarity, the components of the acoustic impedance include [30-31, 51-54]:

- *Resistance: Re(Z)* is the real component of the impedance denoting dissipative nature of flame response

- <u>*Reactance*</u>: *Im(Z)* is imaginary component of the impedance and a measure of incident acoustic energy conversion through various forms including periodic rarefaction and compression

In addition, the magnitude $|Z|$ and phase (ϕ_Z) of acoustic impedance is determined by:

$$|Z| = \sqrt{Re(Z)^2 + Im(Z)^2} \qquad \frac{\phi_z}{\pi} = \left(\frac{1}{\pi}\right) atan\left[\frac{Im(Z)}{Re(Z)}\right]$$

(3.16)

3.3.7 Wavelet and Strouhal Number Analysis

The frequency content of the burner exit velocity and heat release perturbations are analyzed using the Continuous Wavelet Transform (CWT). The CWT is analogous to the Fast Fourier Transform but provides the temporal distribution of the frequency spectrum of the signal. Similar to the practice in the Fourier transform technique, the CWT uses a set of fundamental or "Mother Wavelet" functions to describe the observed signal as an aggregation of composite functions of various frequencies (or "scales" in the case of wavelets). The primary results of the wavelet transform are the wavelet coefficients *C(t,a)* used in the transformation of the heat release rate perturbation signal q'*(t)* from the time domain to the scale domain given by [86]:

$$C(t,a) = \int q'(t) \frac{1}{\sqrt{a}} \psi\left(\frac{t-\tau}{a}\right) d\tau$$

(3.17)

In the transformation of the temporal signal *q'(t)*, the "mother wavelet function" given by the function $\Psi(a, t)$ is shifted in time by τ and compressed and/or expanded using the scale, *a*. As a

result, the wavelet coefficients show the degree of correlation of the signal with the particular scales at specific instants in the time domain.

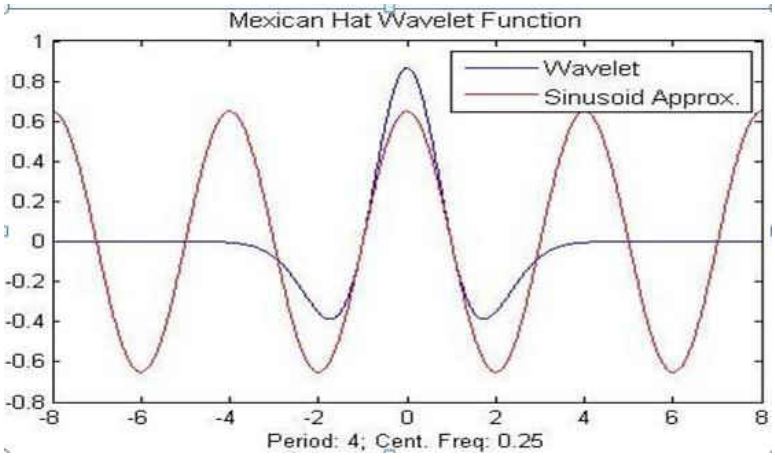

Figure 3.6: Mexican Hat Wavelet and Sinusoidal (f_c = 0.25Hz) Approximation

For a given wavelet, a center frequency, f_c is used in the approximation of the wavelet function using sinusoids. The selected "Mother Wavelet" in this study is the popular Mexican hat wavelet with a center frequency of 0.25Hz. More specifically, the known center frequency allows the conversion of the wavelet scales into frequency equivalents with the relationship:

$$f_a = \frac{f_c}{a\Delta} \tag{3.18}$$

Δ is the per-data point sampling period of the combustion dynamics dataset. Thus, given the wavelet coefficients from Eq. (3.10) at predetermined scales, Eq. (3.11) allows for the temporal resolution of the signal's frequency response since larger wavelet coefficients are proportional to the power of the various frequency modes at specific time instants.

CHAPTER 4 CONSTANT FUEL FLOWRATE COMBUSTION DYNAMICS

The frequency spectra of the acoustic perturbations introduced by the speaker are first discussed. This is followed by the coherence between the introduced forcing and the flame dynamics as well as their associated frequency spectra. The time-averaged flame response for the relatively rich (C1) and lean (C2) constant fuel flow rate conditions across all swirl intensities are then presented. The phase conditioned analysis of the flame response at all swirl intensities is subsequently discussed. The application of the Flame Response Index, acoustic impedance and continuous wavelet spectra in identifying highly responsive modes is presented. Finally, prevalent criteria in highly responsive flame configurations are summarized.

4.1 Imposed Acoustic Perturbation Frequency Spectra

As a precursor to the flame dynamics results, Figure 4.1 illustrates the binned frequency spectra of the normalized pressure perturbations ($\hat{p}_1$) at the base of the burner for unpulsed (f_p = 0Hz) and acoustically forced configurations. Immediately evident is the presence of pulsing frequency harmonics below a 500Hz cutoff threshold. More harmonics are present for lower pulsing frequencies with the 105Hz pulsing frequency characterized by up to three harmonics of considerable power above the background spectra. The various forcing modes are characterized by comparable acoustic power at the fundamental as illustrated in Figure 4.1 with gradually decaying magnitudes at succeeding harmonics.

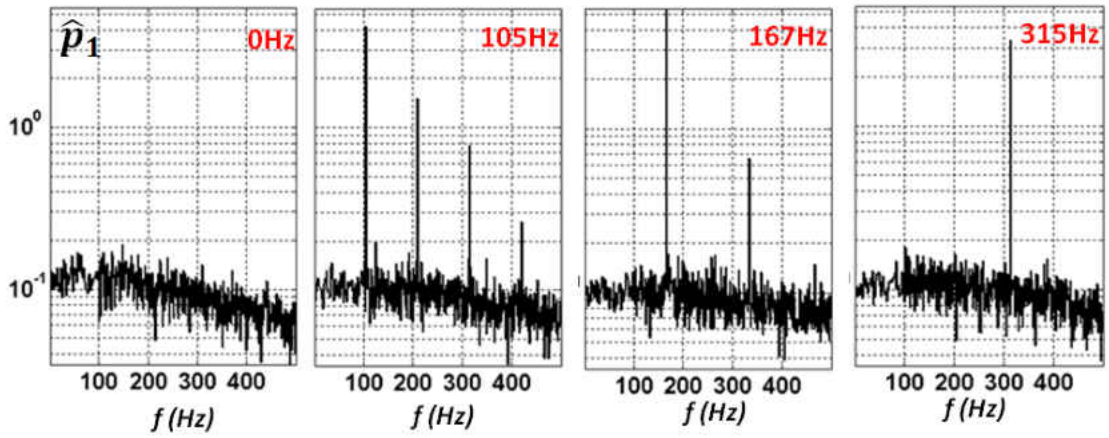

Figure 4.1: Frequency Spectra of Imposed Acoustic Perturbations

4.2 Coherence Analysis

As previously discussed, the magnitude squared coherence function (γ^2) allows the degree of causality between a system input and output to be examined. Higher coherence values are characteristic of highly correlated processes with a high degree of causality approaching coherence values of unity for strongly linear processes. The coherence estimates between the measured flame dynamics parameters are presented in Figure 4.2 for low swirl intensity (S009) at the 0Hz (unpulsed), 105Hz and 315Hz forcing frequencies.

The unpulsed (f_p = 0Hz) flame configuration in Figure 4.2 suggest a relatively high background noise level between the flame dynamics parameters. This is to be expected given the highly nonlinear mixing processes inherent in the non-premixed configuration in the present study. In Figure 4.2 there appears to be some coherence at natural modes between the various unforced flame dynamics parameters particularly for lean (C2) flames.

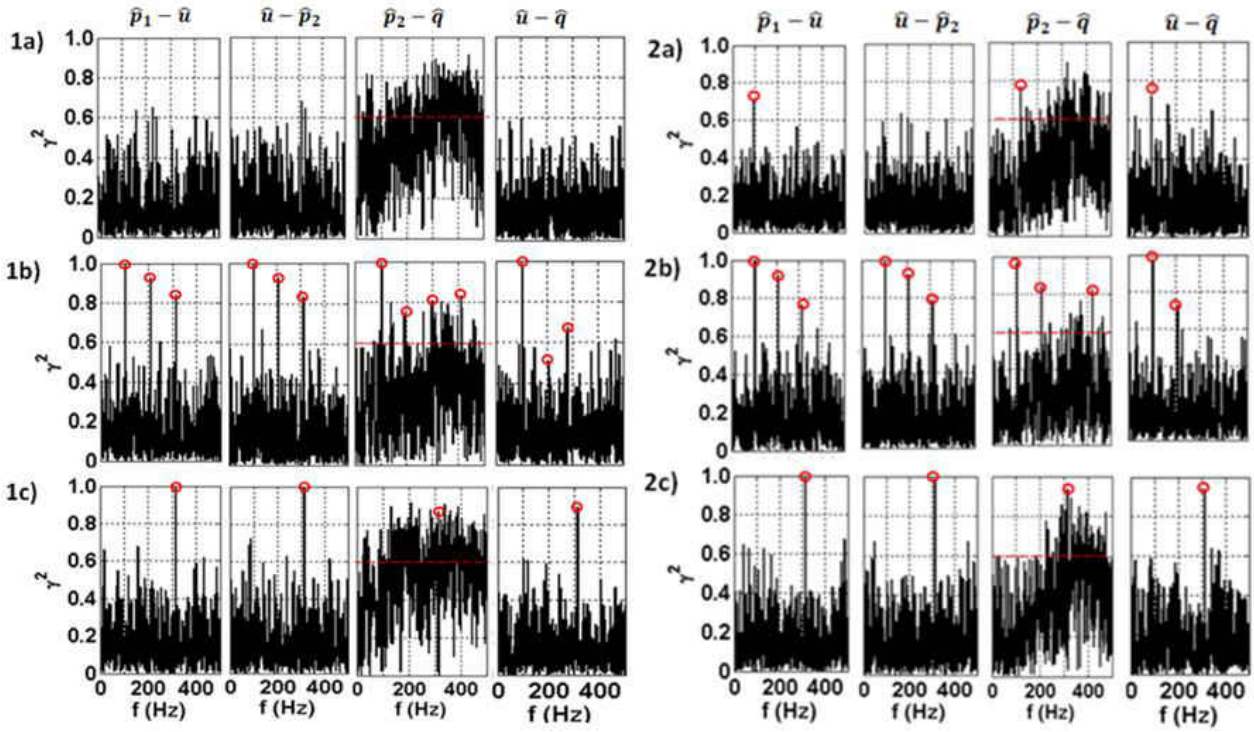

Figure 4.2: Magnitude Squared Coherence – S009
1. S009-C1 | 2. S009-C2
a. f_p = 0Hz | b. f_p = 105Hz | c. f_p = 315Hz

For the low swirl lean flame (S009-C2), with a γ^2 value of approximately 0.7, there is a clearly observable natural mode at 100Hz between the burner base pressure ($\hat{p}_1$) and the burner exit velocity perturbations ($\hat{u}$). The unforced leans (C2) flame in Figure 4.2-2a illustrates some coherence ($\gamma^2 \approx 0.6$) between the velocity and the burner exit pressure ($\hat{u}$-$\hat{p}_2$) perturbations at 100Hz as well as its harmonics up to 400Hz. This unforced flame is also characterized by ($\hat{p}_2$-$\hat{q}$) and ($\hat{u}$-$\hat{q}$) processes naturally coupling at 100Hz. There is an additional broadband coupling for the ($\hat{p}_2$-$\hat{q}$) process centered at 300Hz indicating the natural mode of the flame-pressure feedback process. There does not appear to be a similar significant 100Hz coherence in the

unpulsed rich (C1) flame in Figure 4.2-1 except for the ($\hat{p}_2$-$\hat{q}$) process with a broadband coupling across several frequencies above the background noise inherent in the system dynamics.

With the introduction of acoustic pulsing, Figure 4.2 also illustrates very strong coherence estimates (γ^2 > 0.8) for various system dynamics at the fundamental 105Hz pulsing frequency as well at its first two harmonics (210Hz and 315Hz). The supplied acoustic energy drives the flame response at the supplied fundamental frequency or its harmonics. In the lean (C2) flame characterized by processes coupling at the previously identified 100Hz natural mode, the acoustic energy reinforces the system dynamics at their natural coupling modes.

At the 315 Hz pulsing mode, Figure 4.1 demonstrated the absence of any harmonics with only the fundamental mode present in the frequency spectra. As a result, the magnitude square coherence estimates for this pulsing mode in Figure 4.2-3 are characterized by a single very strong coupling (γ^2 ≈ 1) at 315Hz for both rich (C1) and lean (C) flames. This pulsing mode also corresponds to the peak coherence mode for the ($\hat{p}_2$-$\hat{q}$) process for both lean and rich flames. Figure 4.2c illustrates that this mode and the broadband region is reinforced for the ($\hat{p}_2$-$\hat{q}$) process (γ^2 > 0.9) with acoustic forcing at 315Hz. In addition, most of the previously identified natural acoustic modes (such as the 105Hz natural mode) are suppressed for the various system processes at the 315Hz pulsing mode for the low swirl intensity flames in Figure 4.1.

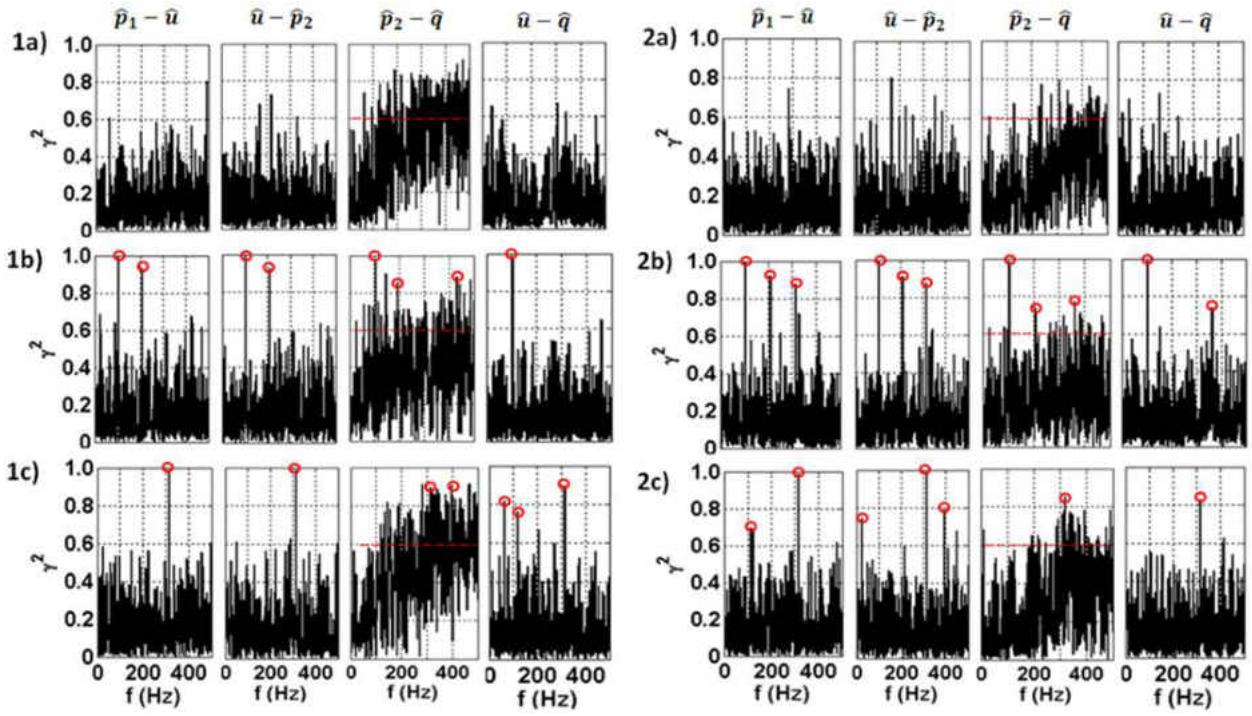

Figure 4.3: Magnitude Squared Coherence – S034
1. S034-C1 | 2. S034-C2
a. fp = 0Hz | b. fp = 105Hz | c. fp = 315Hz

The observed coherence dynamics for the high swirl intensity (S034) flame configurations are presented in Figure 4.3. The primary difference in the unpulsed flames at high swirl is the absence of the natural 105Hz mode in the unpulsed dynamics particularly at lean (C2) fuel flowrates detailed in Figure 4.3-2a. In the high swirl intensity (S034) flames at rich fuel (C1) conditions and 105Hz acoustic pulsing, the 315Hz harmonic in Figure 4.3-1b is observed to be less coherent compared to the analogous low swirl intensity flame in Figure 4.2-1b. The lean (C2) flames at high swirl and pulsed at 105Hz exhibit harmonics in the flame response that are similar to those in the corresponding low swirl configuration in Figure 4.2-3.

4.3 Flame Response Frequency Spectrum Analysis

The binned power spectrum for the normalized flame response perturbations ($\hat{q}$, $\hat{p}_2$, $\hat{u}$) of the constant fuel flow rate (C1 and C2) conditions and low swirl intensity (S009) are illustrated in Figure 4.4. In the figure, the acoustic pulsing frequencies are abbreviated as f_1 through f_8 with the nomenclature provided. The peak frequency observed in the power spectrum at each pulsing frequency is provided in the legend. For example, a legend of f_1[14Hz] implies an observed peak frequency of 14Hz in the signal due to flame response effects from acoustic forcing at a frequency of 0Hz (unpulsed).

The primary effect of acoustic forcing is to amplify heat release rate ($\hat{q}$) perturbations in the 1Hz – 10Hz range centered around 3Hz as illustrated in Figure 4.4. However there is a significant difference in the flame response of the rich (C1) and lean (C2) flames. The amplitudes of heat release perturbations ($\hat{q}$) in the 1Hz – 10Hz range elicited due to acoustic pulsing are significantly higher in the low swirl (C2) flames. The low swirl flames with the highest heat release rate response are acoustically forced at 105Hz through 201Hz. In this forcing frequency range, Figure 4.4 illustrates that the heat release rate response occurs at the same frequency as the incident acoustic perturbations.

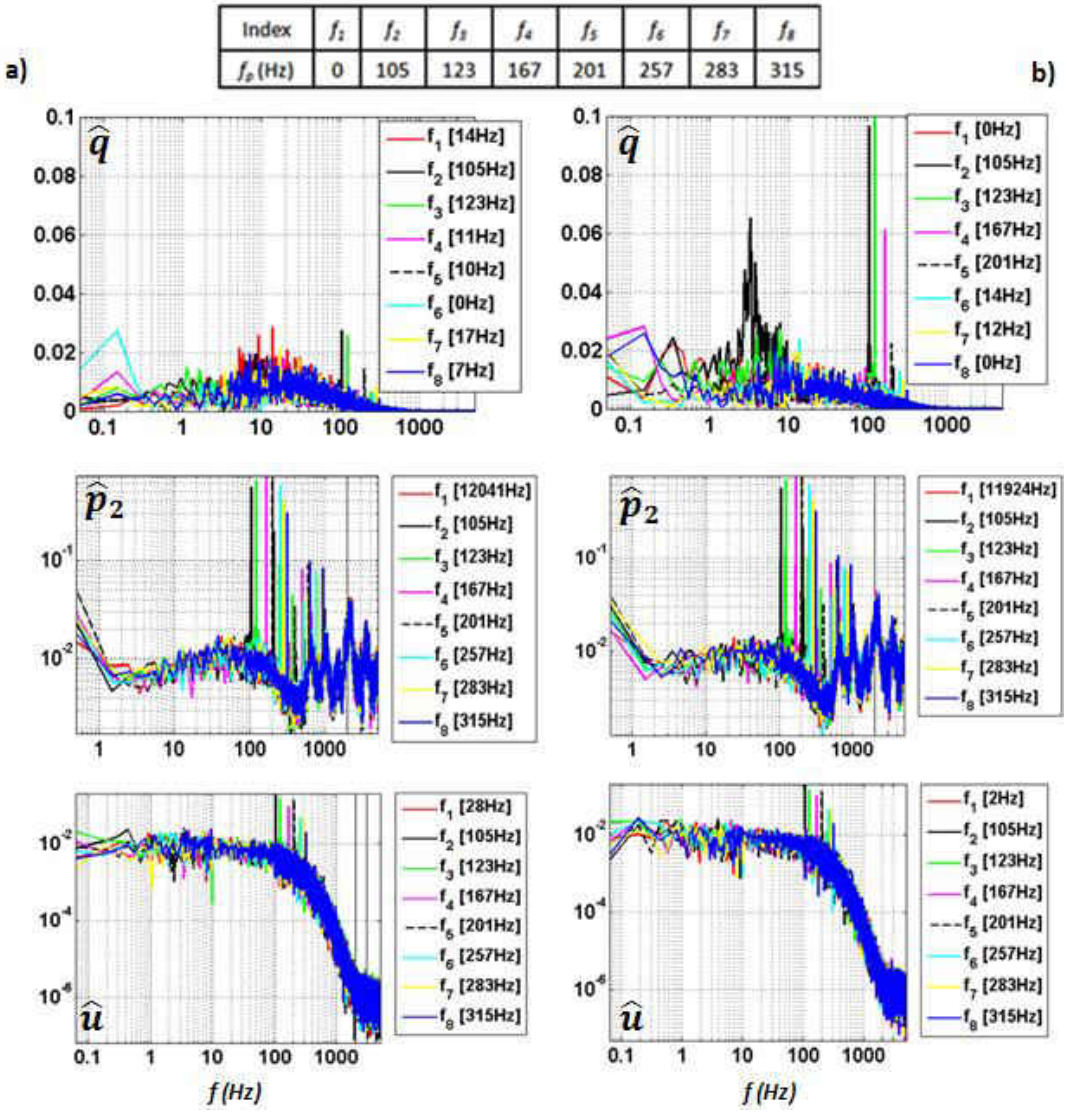

Figure 4.4: Flame Response Frequency Spectra – S009
a. Rich (C1) Flames | b. Lean (C2) Flames

The frequency spectra for the high swirl intensity (S034) flames are illustrated in Figure 4.5 for both lean (C1) and rich (C2) fuel flowrates. As observed in low swirl flames, distinctive heat release rate perturbation peaks at the forcing modes are obtained for frequencies of 105Hz through 201Hz in the high swirl flames of Figure 4.5. The power spectrum shows not only a distinctive $\hat{q}$ frequency response at the fundamental but also a wider strong perturbation region dissipated (smeared) over a broad band of frequencies centered around 3Hz.

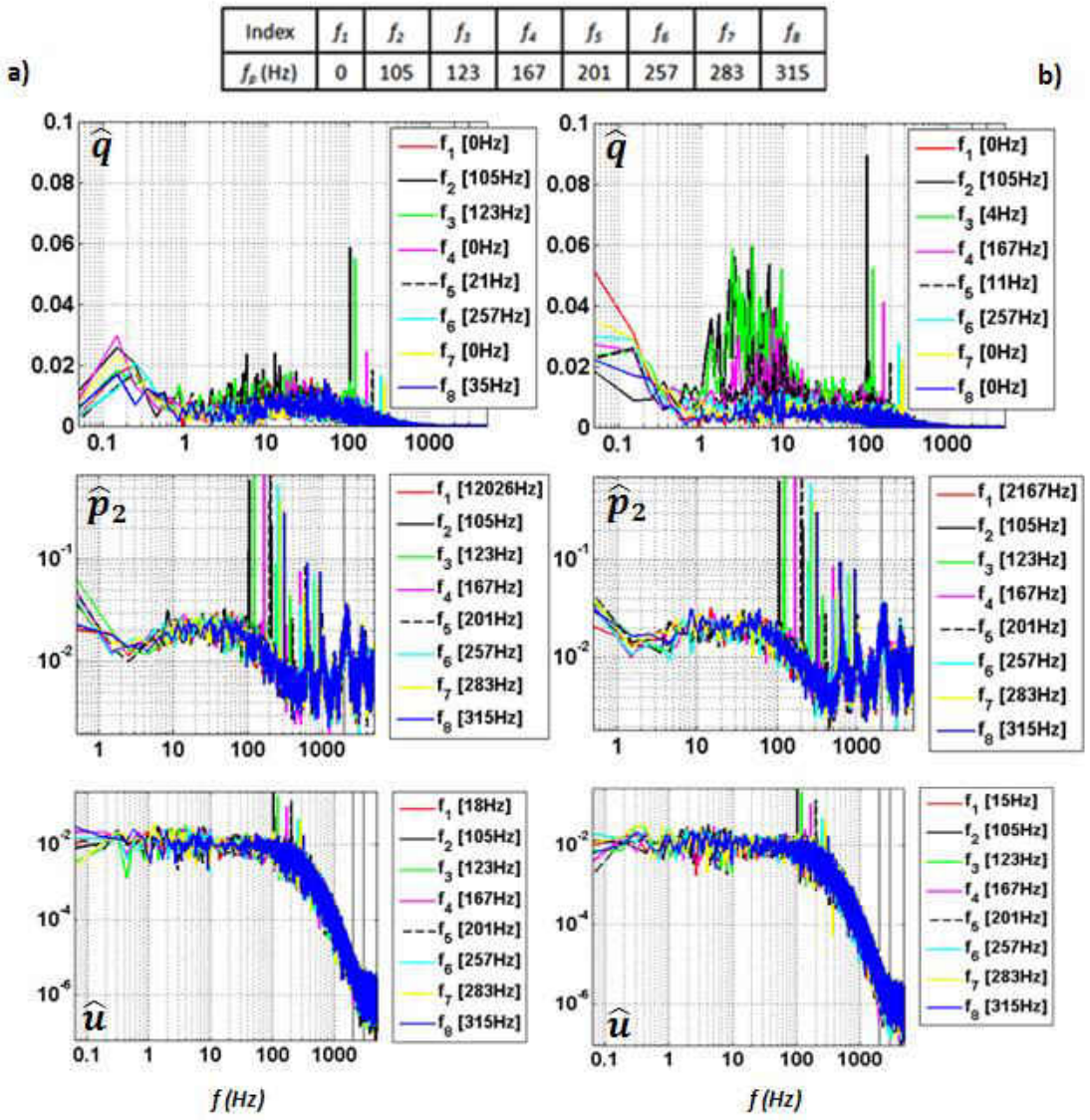

Figure 4.5: Flame Response Frequency Spectra – S034
a. Rich (C1) Flames | b. Lean (C2) Flames

The results in Figure 4.4 and 4.5 show increasingly prominent heat release perturbations centered around 3Hz at higher swirl intensity. As an example, Figure 4.4 shows acoustic forcing at 123Hz yielding minimal 3Hz-centered CH* $\hat{q}$ perturbations for the lean flame (C2) at the S009 swirl level. At the S034 swirl intensity level, Figure 4.5 shows higher amplitude 3Hz–centered perturbations for the same 123Hz acoustic forcing in lean (C2) flames. This is accompanied by a

reduction in the energy at the fundamental 123Hz mode. This suggests that increased swirl enhances the accessibility of dynamic modes other than the fundamental mode of heat release perturbations. In other words, increasing the swirl intensity in leaner flames facilitates energy transfer from the forcing mode to other dynamic modes associated with the natural flame dynamics.

The opposite flame response is observed in the rich (C1) flames subjected to acoustic perturbations. The higher S034 swirl intensity rich (C1) flames in Figure 4.5 exhibit higher energies at the forcing mode compared with the S009 rich (C1) flames in Figure 4.4. For the richer (C1) flames, there is also minimal energy in the 1Hz – 10Hz range compared to the leaner (C2) counterparts.

A closer examination of the peak heat release rate ($\hat{q}$) response frequencies reveal that richer (C1) flames are less able to resonate at the forcing frequency compared with the lean (C2) flames. As a result the leaner flames consistently yield heat release rates oscillations at the forcing frequency for acoustic perturbations in the highly responsive 100Hz – 201Hz range. In the richer (C1) flames, it is likely that the higher acoustic oscillation amplitude threshold necessary to yield heat release perturbations at the forcing frequencies were not met resulting in $\hat{q}$ perturbations at lower frequencies.

4.4 Time Averaged Flame Response

The time averaged flame CH* chemiluminescence intensity images for the two swirl intensities and fuel flow settings are presented for all acoustic pulsing frequencies in Figure 4.6. The time-averaged image areas are obtained by averaging the 112 CCD images acquired over the 14s sample period.

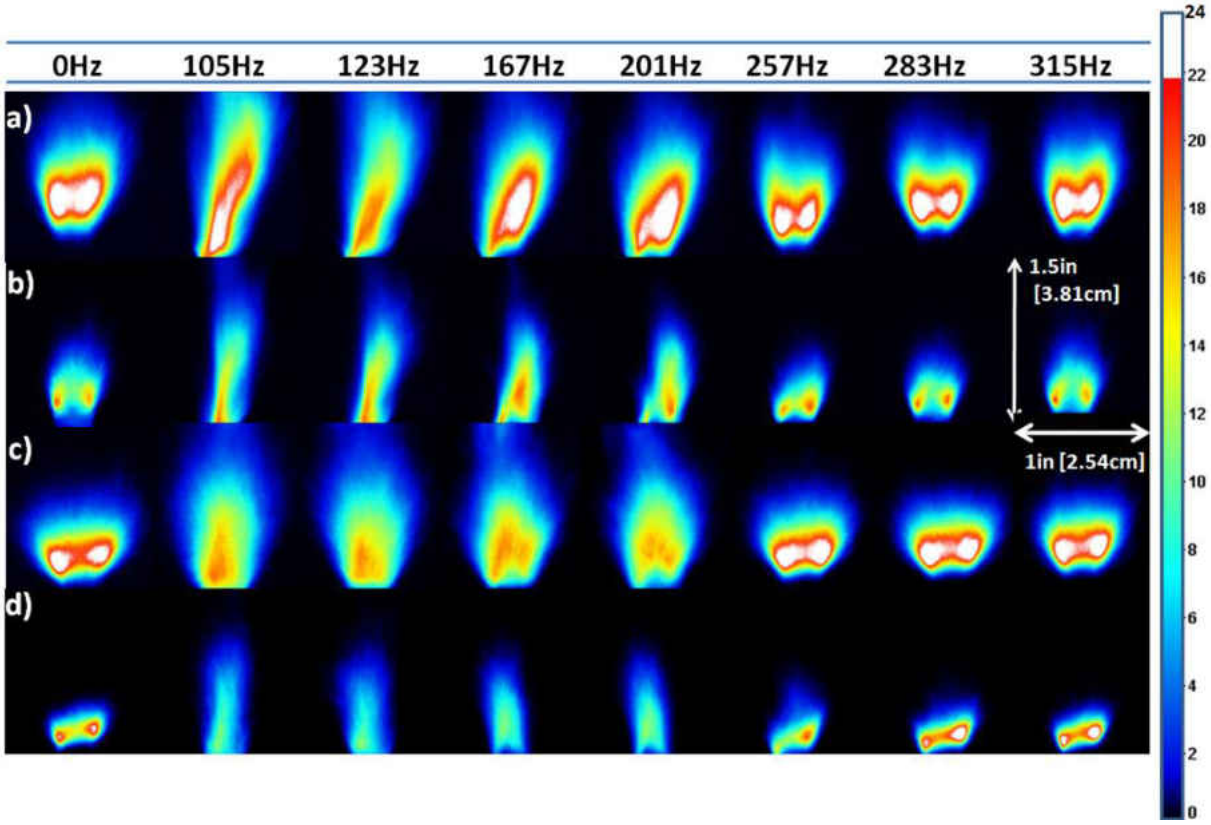

Figure 4.6: Time Averaged CH* Chemiluminescence Images
a. S009-C1 | b. S009-C2 | c. S034-C1 | d. S034-C2

The unpulsed (f_p = 0Hz) cases show generally symmetric flame structures lifted from the burner exit. There is however some asymmetry in the core of the flame geometry which will be subsequently addressed. The leaner fuel flow rate (C2) flames are observed to move upstream towards the fuel pipe even in the unpulsed mode. In the acoustically perturbed modes, the

flame is completely attached to the central fuel pipe for the highly responsive 105Hz through 201Hz acoustic pulsing modes. At lean (C2) conditions, Figure 4.6 illustrates low swirl flames with larger flame surfaces areas and high swirl flames with lower flame surface area. This suggests a central role of inertia related to higher centrifugal forces inherent at higher swirl levels.

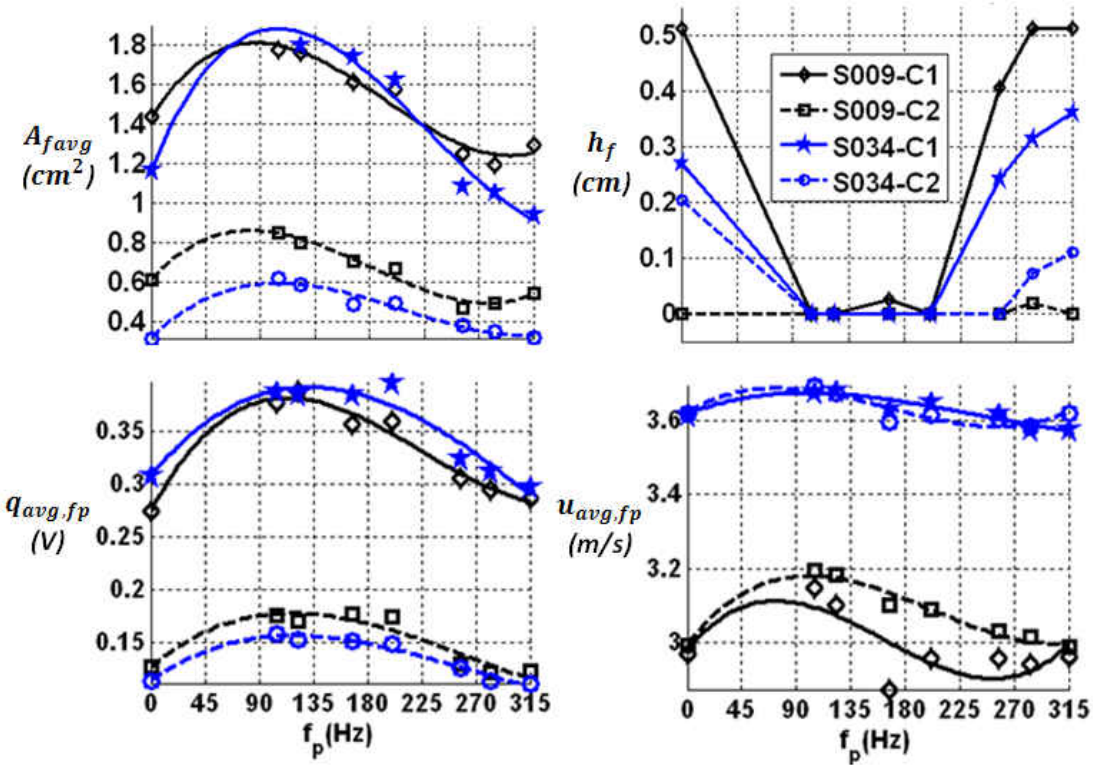

Figure 4.7: Time Averaged Flame Response

The time averaged flame response is summarized in Figure 4.7 to include the average flame surface area (A_{favg}), heat release rate ($q_{avg,fp}$), liftoff height (h_f) and velocity ($u_{avg,fp}$) at each forcing frequency. The highly responsive acoustic modes between 105Hz and 201Hz are associated with the largest average flame surface areas (A_{favg}). The richer (C1) flames have a larger surface area compared to the leaner (C2) flames. This is expected due to the lower fuel

supply in the leaner (C2) fuel flow configuration and is reflected in the CH* chemiluminescence images of Figure 4.6. In the unpulsed (f_p = 0Hz) mode, the resulting flame surface area is smaller at the higher swirl intensity. This occurs for both the C1 and C2 flames and is possibly linked to the fluid dynamics associated with higher swirl. The average velocity at the burner exit also appears to be a strong function of swirl intensity with minimal impact of fuel flowrate variation.

The lift-off height (h_f) is observed to be zero (attached to fuel pipe) for the lean, low swirl (S009-C2) flames in both the pulsed and unpulsed modes. The upstream displacement of the flame is also observed in the liftoff height curves of Figure 4.7 for richer (C1) flames at high swirl. This suggests that the upstream displacement of the flame is symptomatic of any combination of three phenomena to include high swirl intensity, lower fuel flowrates and the introduction of acoustic forcing.

In Figure 4.7, the flame surface area, flame liftoff height and CH* chemiluminescence images of Figure 4.6 illustrate previously reported highly responsive flame response dynamics below a cut-off forcing frequency of 201Hz. Beyond this cut-off frequency the flame surface areas and liftoff heights essentially return to their unpulsed modes. As a result the flame response is characterized by a low pass filter behavior consistent with dynamic flame behavior previously reported for a variety of flame configurations [19, 26-36, 44-46].

The low pass flame response characteristic observed is also reflected in the normalized time averaged flame response data reported in Figure 4.8. The time-averaged heat release rate,

velocity and flame surface area data are normalized by their corresponding time averaged quantities at the unpulsed (f_p = 0Hz) mode. The normalized CH* chemiluminescence intensity (q^*) used as a measure of the heat release rate is amplified at the highly response acoustic pulsing modes as is the normalized flame surface area (A^*). The amplification in heat release rate (q^*) is comparable at both swirl levels. However, the flame surface area amplification (A^*) is much lower in the low swirl flame. This suggests that the higher inertia inherent at higher swirl promotes the amplification in total flame surface area.

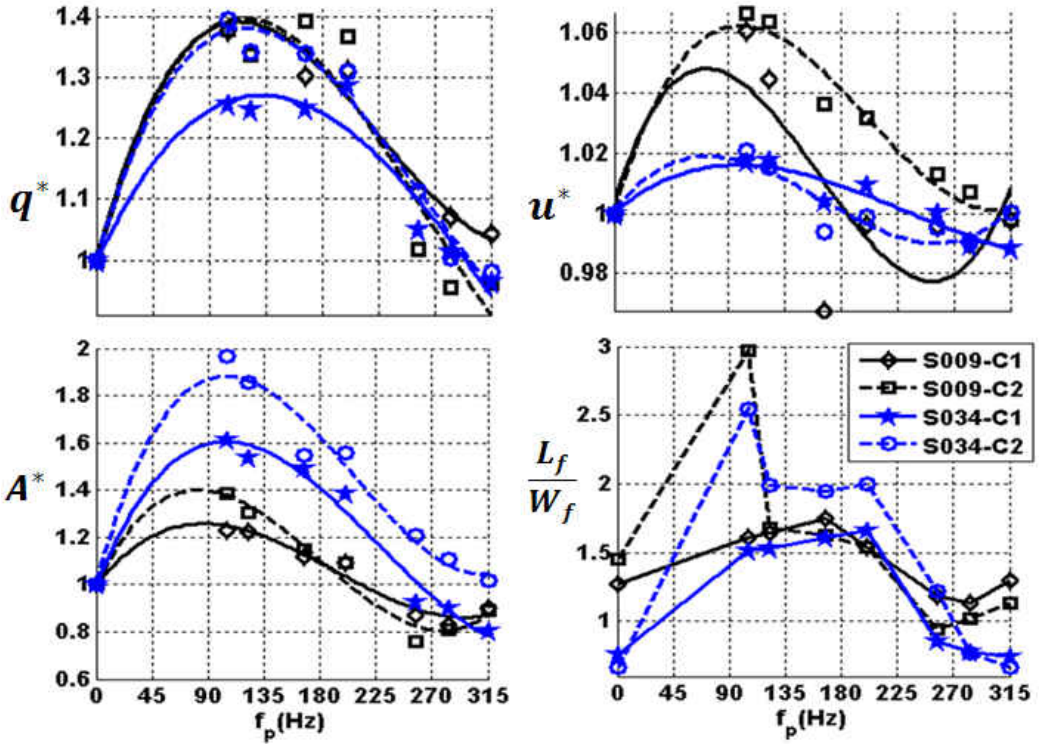

Figure 4.8: Normalized Time Averaged Flame Response

$$q^* = \frac{q_{avg,fp}}{q_{avg,fp=0Hz}} \mid u^* = \frac{q_{avg,fp}}{q_{avg,fp=0Hz}} \mid A^* = \frac{A_{favg}}{A_{favg,fp=0Hz}}$$

The time averaged flame chemiluminescence images of Figure 4.6 illustrate significant amplification in the vertical flame length (L_f) within the highly responsive acoustic pulsing regime. This amplification in the flame length can be quantified by the ratio of the vertical

flame length (L_f) to the flame width (W_f) or the flame aspect ratio. The flame aspect ratio (L_f/W_f) curves in Figure 4.8 show the highest flame aspect ratio at the 105Hz acoustic pulsing mode, gradually returning to unpulsed values beyond 201Hz forcing.

The highly responsive nature of lean (C2) flames is reflected in their generally higher flame aspect ratios in Figure 4.8. This is in contrast to the higher swirl flames characterized by higher total flame surface area (A^*) in Figure 4.7. The inherent inertia in the flame consequently plays a considerable role in the response mechanism to acoustic forcing. The lean flames primarily respond with amplification in aspect ratio while high swirl flames undergo an increase in total flame surface area.

The higher aspect ratio response in low swirl flames imply they are subject to higher strain rates in comparison to the high swirl flames. These higher strain rates do not appear to diminish the heat release rate response of the low swirl flames. For example, Figure 4.8 shows the normalized heat release rate (q^*) response to be comparable across swirl intensities particularly for lean flames. This is the case in spite of the different flame amplification mechanisms involved such as the lower surface area (A^*) amplification observed in the low swirl intensity flames. The restoration of the flame response to its unpulsed mode at pulsing frequencies beyond 200Hz is also clearly reflected in the flame surface area, heat release rate and velocity response in Figure 4.8. There also appear to the good correlation between the normalized heat release rate (q^*) and flame surface area (A^*) in Figure 4.8 for high swirl (S034) flames.

4.5 Flame Response Index Analysis

The Rayleigh criterion is well established as a necessary condition from for the occurrence of instability and has been widely discussed in literature [4, 9-12]. Based on Eq. 3.8, it is an estimate of the in-phase relationship between the burner exit pressure (p_2') and heat release rate (q') perturbations and is typically applied to unforced flame configurations. A positive Rayleigh index will indicate in-phase perturbations with a potential for instability due to coupling and feedback between heat release rate and pressure perturbations.

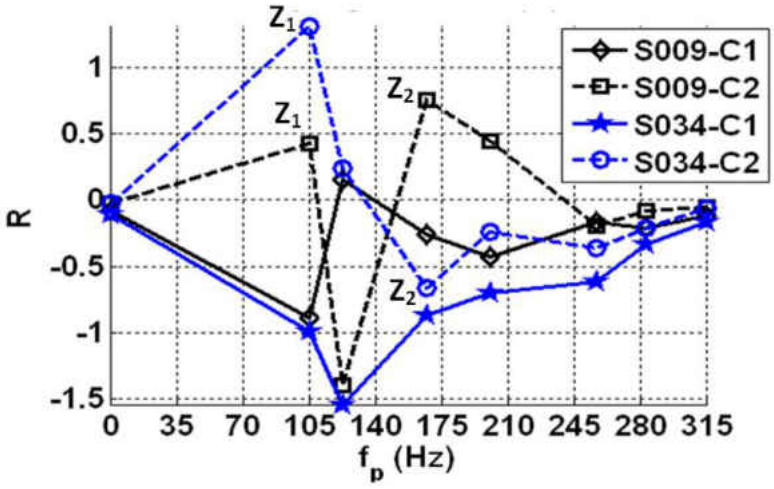

Figure 4.9: Flame Response Index Estimate
Zn – Flame Location in complex Acoustic Impedance Plane of Figure 4.16

As the majority of flame configurations in the present study are acoustically forced, a Flame Response Index (R) is defined to estimate the in-phase relationship between the burner exit (p_2') and flame heat release rate (q') perturbations. The defined Flame response index consequently collapses to the familiar Rayleigh index for the unforced flame configurations. As is the case in the Rayleigh criteria, a positive Flame Response Index implies in-phase heat release rate and burner exit pressure perturbations.

Figure 4.9 illustrates the Flame Response Indices for the various swirl intensities and fuel flow rate settings. The Z_n nomenclature indicates locations of selected flame configurations in the complex acoustic impedance plane to be subsequently discussed in Figure 4.16. Immediately evident is that the 105Hz flames are primarily located in the Z_1 impedance zone while the 167Hz flames are located in the Z_2 impedance region.

Flames with positive indices in Figure 4.9 are primarily confined to leaner (C2) flames characterized by large aspect ratio amplification in Figure 4.8. The configurations with the highest flame response indices are lean flames at 105Hz and 167Hz acoustic pulsing modes. For the lean (C2) configurations, Figure 4.9 shows the 167Hz highly responsive mode present at low swirl (S009) is converted to a minimally responsive mode (negative index) at higher swirl intensity (S034).

The opposite phenomena is exhibited at the 105Hz pulsing mode where the response index of the lean (C2) flame increases resulting in a more responsive flame at the high swirl (S034) intensity level. The mechanism by which the responsive 167Hz mode is eliminated and the 105Hz mode response is amplified can be understood by examining the phase relationships between the various flame response parameters.

4.6 Phase-Conditioned Flame Response

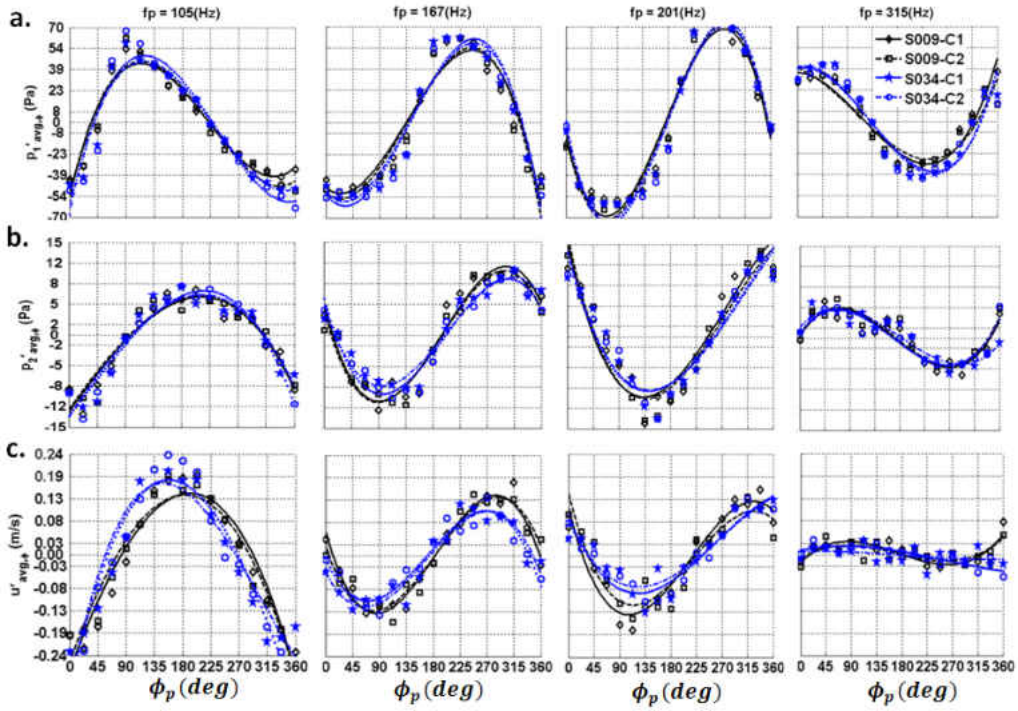

Figure 4.10: Phase Conditioned Perturbations
a. Burner Base Pressure ($p_1'_{avg,\phi}$) | b. Burner Exit Pressure ($p_2'_{avg,\phi}$)
c. Burner Exit Velocity ($u'_{avg,\phi}$)

The phase conditioned velocity and pressure perturbations at the burner base ($p_1'_{avg,\phi}$) and exit ($p_2'_{avg,\phi}$) are illustrated in Figure 4.10. The consistent nature of the supplied perturbations at the base of the burner is clearly evident across swirl intensities in Figure 4.10a. This is particularly important in determining the impact of swirl intensity on the flame response to acoustic forcing. The phase lag from the acoustic forcing signal to the burner base pressure ($p_1'_{avg,\phi}$) perturbations increases with forcing frequency. The phase lag of the burner base pressure perturbations appears to increase at higher forcing frequencies while the amplitude of the pressure perturbations at the burner exit ($p_2'_{avg,\phi}$) decreases at higher forcing frequencies.

The velocity perturbations in Figure 4.10c appear to exhibit some dependence on the swirl intensity. This is particularly the case for the highly responsive 105Hz forcing mode. Increased swirl (S034) leads to a reduction in the phase lag between the imposed pressure perturbations in Figure 4.10a and the resulting velocity oscillations in Figure 4.10c. The velocity oscillation amplitude is also highest at the 105Hz forcing frequency.

4.6.1 Phase–Averaged CH* Chemiluminescence Imaging

The phase conditioned images of several flame configurations are presented in Figure 4.11 for representative frequencies. The CH* chemiluminescence images are generally consistent with the large aspect ratio response observed in the time-averaged flame images of Figure 4.6. As observed in the time-averaged flames, the richer (C1) flames are larger in area compared to the leaner (C2) flames.

The leaner flames in Figure 4.11 are translated upstream across all forcing frequencies with attachment to the fuel pipe in some cases. These lean (C2) flames also exhibit a higher aspect ratio response compared to the richer (C1) flames. As previously indicated, the physical mechanism for flame attachment appears to be strongly linked to the fluid dynamics induced by acoustic forcing. This physical mechanism appears exacerbated in the lean flames leading to the observed large aspect ratio amplification.

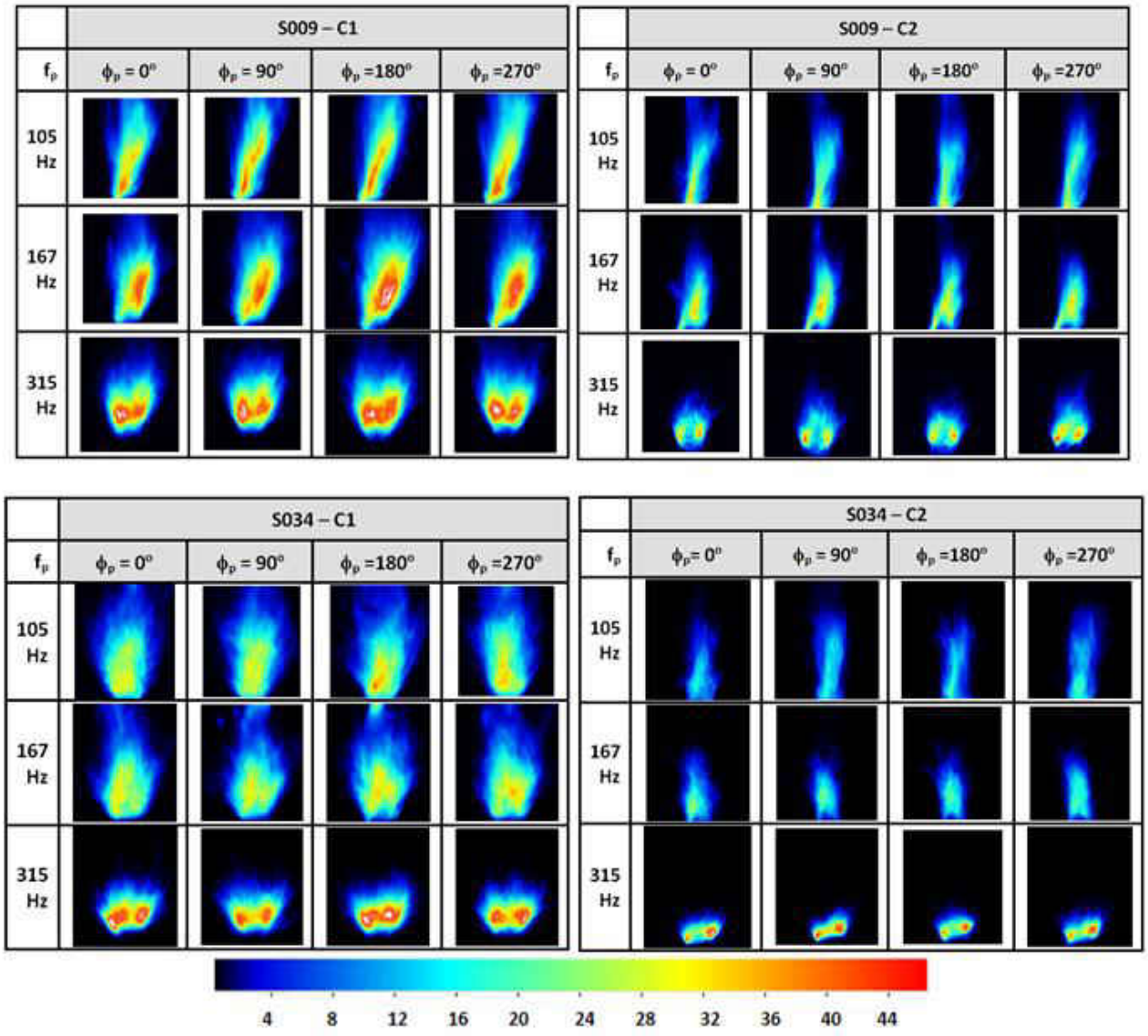

Figure 4.11: Phase Conditioned CH* Chemiluminescence Images

The phase dependence of the estimated flame surface area fluctuations at representative acoustically pulsed modes is illustrated in Figure 4.12 for the high swirl level. The increased susceptibility of lean (C2) flames to acoustic forcing is illustrated by their larger flame area fluctuations in Figure 4.12b. Indeed, the most vigorous flame surface area fluctuations are observed for lean (C2) flames at the highly responsive 105Hz acoustic pulsing mode. This flame configuration is also characterized by the highest flame response index (R >> 0) in Figure 4.9.

The flame surface area fluctuations are less vigorous in the minimally responsive (R<0) S034-C2 flame with acoustic forcing at 315Hz.

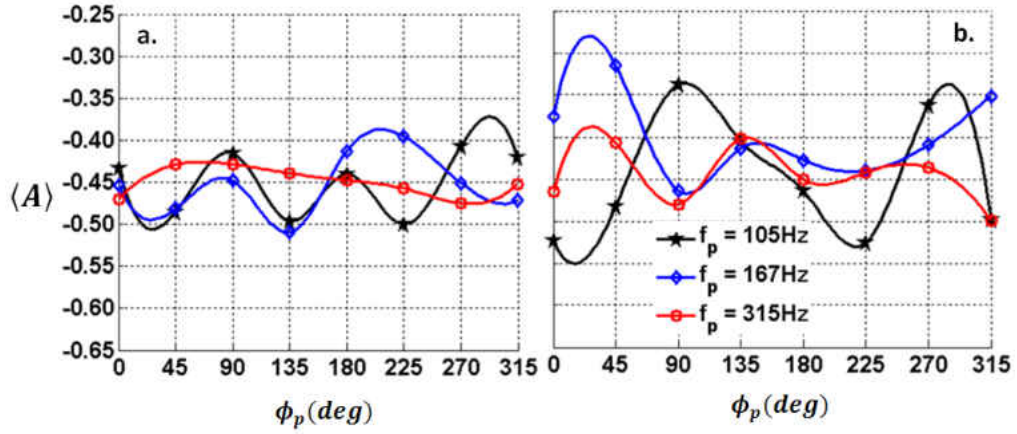

Figure 4.12: Normalized Phase Conditioned Flame Surface Area Fluctuations
a. S034-C1 | b. S034-C2

$$\langle A \rangle = \frac{A_{favg,\phi} - A_{favg,fp}}{A_{favg,fp}}$$

The spectra of the imposed acoustic perturbations in Figure 4.1 indicated the presence of up to two harmonics of lower amplitudes compared to the fundamental. The effect of these harmonics on the phase conditioned flame surface area appears to be the area oscillations over the perturbations cycle evident in Figure 4.12. In the following discussion, a phase conditioned analysis is carried out on the other flame response measurements to include pressure, velocity and CH* chemiluminescence intensity.

4.6.2 Phase-Conditioned Flame Response Analysis

Figure 4.13 illustrates the phase-conditioned flame response based on Eq. (2) and Eq. (3) for various parameters in richer (C1) flames. Data points of are illustrated with markers for each measurement at specific phase angles relative to the acoustic signal. The curves illustrate the

first harmonic (f_p) sinusoidal fits to the measured flame response data. The left column of Figure 4.13 describes the phase conditioned results for acoustic pulsing at 105Hz for the low swirl (top) and high swirl (bottom) configurations. The magnitude of the Flame Response Index (R) for each flame is shown for each flame configuration. Also annotated is the location of the each flame (Z_n) in the subsequently discussed complex impedance plane of Figure 4.16.

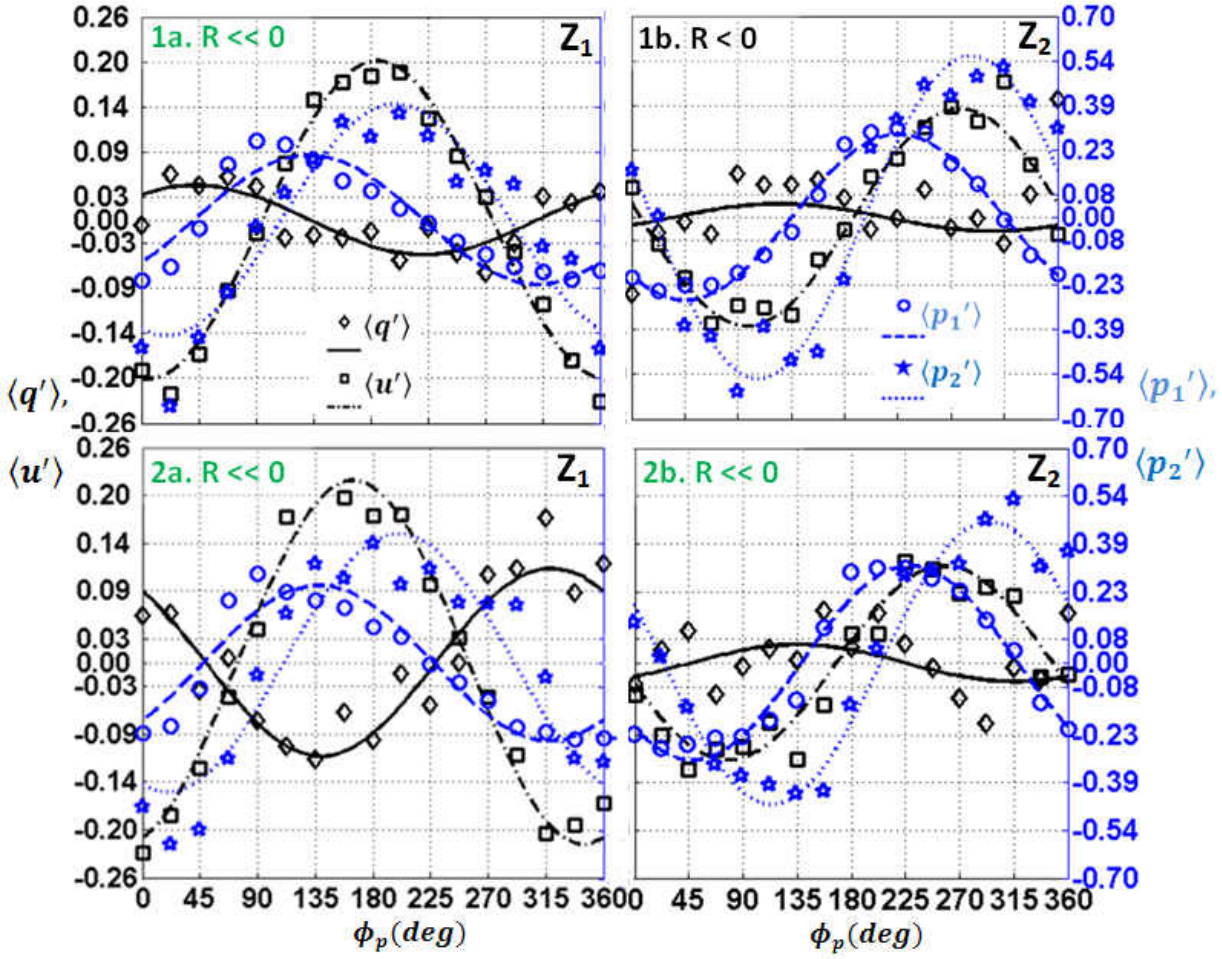

Figure 4.13: Normalized Phase Conditioned Flame Response – Rich (C1) Flames
1a. S009-C1-105Hz | 1b. S009-C1-167Hz
2a. S034-C1-105Hz | 2b. S034-C1-167Hz
R – Flame Response Index from Figure 4.9
Zn – Flame Locations in Complex Acoustic Impedance Plane of Figure 4.16

$$\langle q' \rangle = \frac{q'_{avg,\phi}}{q_{avg,fp}} \mid \langle u' \rangle = \frac{u'_{avg,\phi}}{u_{avg,fp}} \mid \langle p'_1 \rangle = \frac{1}{200} P'_{1avg,\phi} \mid \langle p'_2 \rangle = \frac{1}{20} P'_{2avg,\phi}$$

The rich (C1) flame phase conditioned curves in Figure 4.13 clearly demonstrate the relatively short time lags between the velocity $\langle u' \rangle$ and pressure $\langle p_2' \rangle$ perturbations at the burner exit. This is accompanied by relatively large time lags between the incident velocity $\langle u' \rangle$ and resulting heat release rate $\langle q' \rangle$ oscillations due to acoustic forcing. The result is the out of phase velocity $\langle u' \rangle$ and heat release rate $\langle q' \rangle$ perturbations across all swirl intensities and forcing frequencies in Figure 4.13. This out of phase characteristic is well captured by the generally negative Flame Response index values (R<0) for the rich (C1) flames in Figure 4.13, demonstrating its utility in identifying the phase relationships particularly between heat release rate $\langle q' \rangle$ and pressure $\langle p_2' \rangle$ at the burner exit.

The rich (C1) flames in Figure 4.13 are also characterized by relatively minimal flame aspect ratio amplification in Figure 4.8. Thus it is possible to conclude that the negative Flame Response Index is an indicator of flame configurations that are minimally responsive to acoustic forcing. This result is consistent in spite of the swirl intensity, forcing frequency and perturbation amplitude variations in the richer (C1) flames of Figure 4.13.

The analogous phase conditioned analyses for leaner (C2) flames are illustrated in Figure 4.14. Immediately evident is the positive Flame Response Index (R>0) signifying a strong susceptibility to acoustic forcing in a number of the lean (C2) flame configurations. The mechanism behind the increased flame response index in the lean (C2) flames is a reduction in the heat release rate to velocity phase lag in comparison to the richer (C1) flames in Figure 4.13.

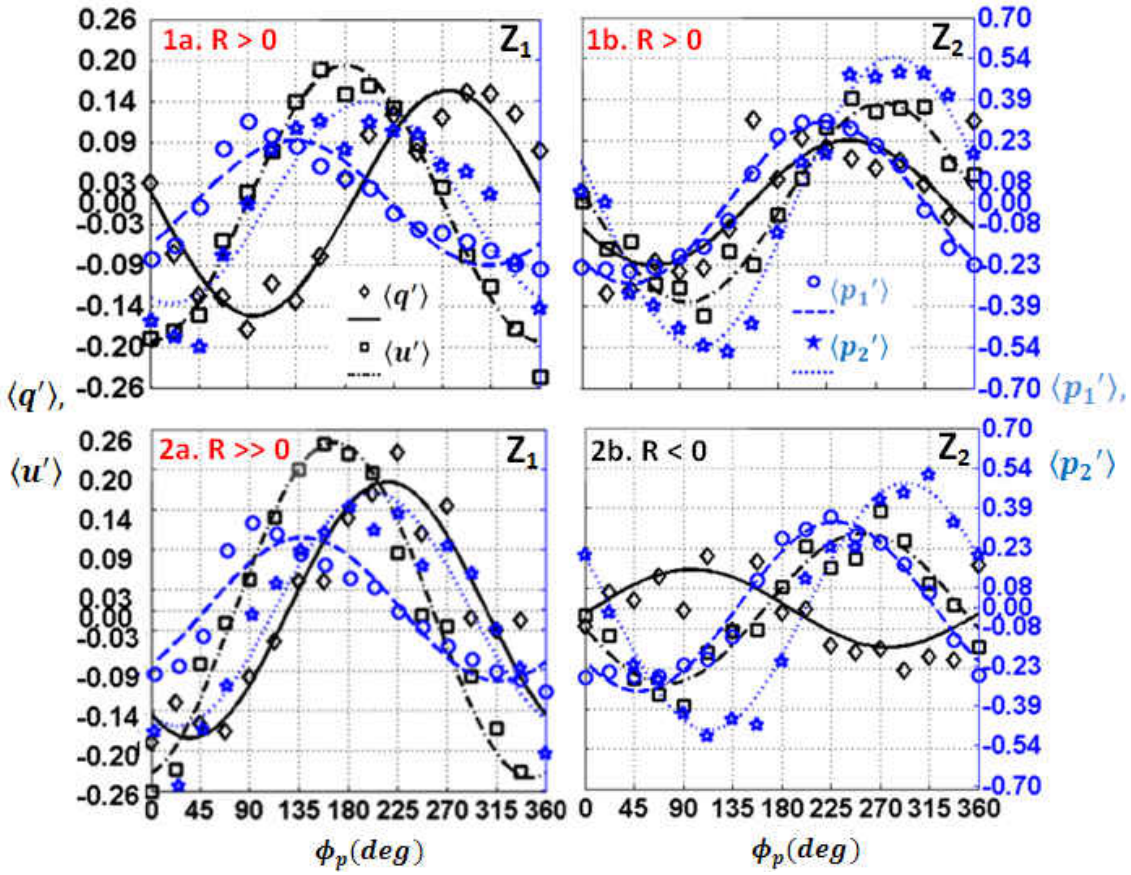

Figure 4.14: Normalized Phase Conditioned Flame Response – Lean (C2) Flames
1a. S009-C2-105Hz | 1b. S009-C2-167Hz
2a. S034-C2-105Hz | 2b. S034-C2-167Hz
R – Flame Response Index from Figure 4.9
Zn – Flame Locations in Complex Acoustic Impedance Plane of Figure 4.16

$$\langle q' \rangle = \frac{q'_{avg,\phi}}{q_{avg,fp}} \mid \langle u' \rangle = \frac{u'_{avg,\phi}}{u_{avg,fp}} \mid \langle p'_1 \rangle = \frac{1}{200} P'_{1avg,\phi} \mid \langle p'_2 \rangle = \frac{1}{20} P'_{2avg,\phi}$$

The lean (C2) flames in Figure 4.14 exhibit higher heat release rate $\langle q' \rangle$ perturbations compared to their richer counterparts. The highest heat release rate perturbations are observed in the high swirl, lean (S034-C2) flame subjected to 105Hz acoustic forcing. In Figure 4.14, this flame is also characterized by a low velocity $\langle u' \rangle$ to heat release rate $\langle q' \rangle$ perturbation phase lag. The end result is that the S034-C2 flame exhibits the highest Flame Response Index (R>>0) of all the lean (C2) flames in Figure 4.14.

The amplitude dependence of the flame dynamics is readily reflected in the phase conditioned results of Figure 4.14. The highest amplitude velocity $\langle u' \rangle$ and heat release rate $\langle q' \rangle$ oscillations are obtained for acoustic forcing at 105Hz increasing with swirl intensity and decreasing at the higher 167Hz forcing frequency. This is the analogous result to the isolated phase conditioned perturbations illustrated in Figure 4.10.

The impact of swirl intensity on the flame response is also visible in Figure 4.14. Acoustic forcing at higher swirl for the 105Hz mode effectively moves the heat release rate $\langle q' \rangle$ increasingly in phase with velocity $\langle u' \rangle$ perturbations thereby reducing the lag. The result is a higher flame response index at the S034 swirl level for 105Hz acoustic forcing. The swirl intensity variations consequently act in a mode switching fashion modifying the phase relationship between the imposed acoustics and the heat release rate. This mode switching mechanism of swirl intensity has also been observed in the recent premixed flame studies of Palies et al. [27].

The reduction in the $\langle u' \rangle$– $\langle q' \rangle$ lag with higher swirl is analogous to a reduction in the lag of the heat release rate $\langle q' \rangle$ relative to the acoustic pulsing signal. At the 167Hz forcing mode in Figure 4.14, the lower lag in $\langle q' \rangle$ relative to the acoustic pulsing signal is also evident. However, the effect of this lag reduction is to move the heat release rate $\langle q' \rangle$ out of phase with the velocity $\langle u' \rangle$ perturbations when acoustically pulsed at 167Hz. The result is the negative index (less responsive flame) observed for the high swirl, 167Hz mode in Figure 4.14.

Two important results are obtained based on the phase conditioned analysis of the flame response. The first involves the critical nature of the fuel flowrate on the flame response, with lean (C2) flames exhibiting a stronger susceptibility to acoustic forcing than their richer (C1) counterparts. The mechanism behind the stronger response appears to be related to the mixing/combustion timescales inherent in the two flame configurations. It should be noted that lag changes essentially represent time delay changes between the heat release rate and velocity perturbations. The longer mixing timescales required for richer fuel flowrates prior to combustion may result in the longer phase lags observed in Figure 4.13 relative to the incident acoustics. On the other hand, the leaner flames appear to exhibit shorter mixing and combustion time scales, resulting in a shorter phase lag to the incident perturbations.

The second important result is the influence of the swirl intensity variations on the flame response. Swirl variations are observed to act in a mode switching manner modifying the relative phase relationships between the flame dynamics. Higher swirl intensities appear to reduce the lag between the acoustic signal and the heat release rate oscillations (i.e. due to improved flame stabilization). This lag reduction manifests as a phase reduction between the heat release rate and acoustic forcing signal. The increased swirl intensity also changes the lag between the velocity perturbations that occur from acoustic forcing. The net lag change between these two processes determines if flames dynamics are in phase (highly responsive, $R>0$) such as S009-C2-167Hz in Figure 4.14. The net lag reduction may also lead to cases such as the S034-C2-167Hz flame with out of phase (minimally responsive, $R<0$) dynamics.

4.7 Flame Transfer Function Analysis

The phase conditioned analysis in the previous discussion led to a qualitative description of the flame dynamics that result from acoustic forcing. In the present section, the flame transfer function method is utilized to obtain a quantitative analysis of the flame response. The major objective is to establish the phase requirements between the various processes in highly responsive flame configurations.

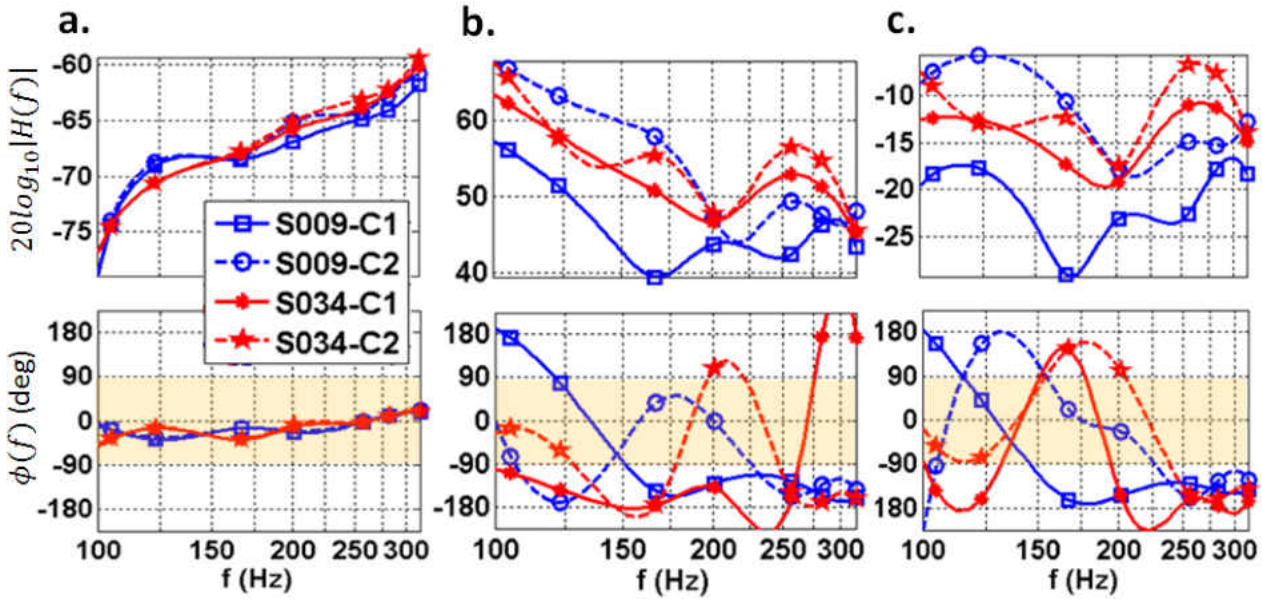

Figure 4.15: Harmonic Forcing (HF-FFT) Transfer Functions

a. Mixing Transfer Function: $M(f) = \frac{\hat{p}_2}{\hat{u}}$ **| b. Reaction Transfer Function:** $R(f) = \frac{\hat{q}}{\hat{p}_2}$

c. Global Transfer Function: $G(f) = \frac{\hat{q}}{\hat{u}}$

Based on the previous results, transfer functions based on the Harmonic Forcing – FFT Post Processed (HF-FFT) method are illustrated in Figure 4.15. The acquired flame dynamics data series at each forcing frequency is used to estimate a single point in the transfer function gain and phase curves based on a linear system assumption. The gain and phase for the flame

response at a specific pulsing frequency are obtained using the complex Fast Fourier Transform (FFT) spectrum component at the pulsing frequency bin. As an example, the gain $H(f_p)$ and phase $\phi(f_p)$ for input x(t) and output y(t) at an acoustic pulsing frequency f_p is determined as:

$$G(f_p) = \frac{Y(f)}{X(f)}\Big|_{f_p} \qquad \phi(f_p) = atan\left\langle \frac{Y(f)}{X(f)}\Big|_{f_p} \right\rangle \tag{4. 1}$$

In Eq. 4.1 the complex FFT transforms of the time domain input x(t) and output y(t) are denoted by *X(f)* and *Y(f)*. The FFT components at the pulsing frequency (f_p) are then extracted to compute the harmonic forcing (HT-FFT) method transfer functions. The HT-FFT based mixing (*M(f)*), reaction (*R(f)*) and global (*G(f)*) transfers functions illustrated in Figure 4.15 are generated at the pulsing frequencies listed in Table 3.

The mixing transfer function *M(f)* in Figure 4.15a relates the velocity ($\hat{u}$) to pressure ($\hat{p}_2$) perturbations at the burner exit as the input and output respectively. At the lower pulsing frequencies high velocity perturbation amplitudes lead to lower gain values in the mixing transfer function. The mixing transfer function gain curves show a primary dependence on the swirl intensity since the mixing process is dominated by the swirling fluid dynamics. The phase angles between the velocity ($\hat{u}$) to pressure ($\hat{p}_2$) perturbations are in the $-90 \leq \phi_M \leq +90$ range for all the flame configurations in the present study. In addition, the velocity ($\hat{u}$) to pressure ($\hat{p}_2$) perturbations phase angles are in the $-90 \leq \phi_M \leq 0$ range for the highly responsive forcing domain of 105Hz – 201Hz.

The reaction transfer function *R(f)* in Figure 4.15b relates the burner exit pressure ($\hat{p}_2$) perturbations to heat release rate ($\hat{q}$) perturbations as the input and output of the process. The gain curves show larger gain values for low frequency acoustic perturbations. This suggests higher heat release rate oscillations generated by lower magnitude pressure oscillations particularly in the low pulsing frequency zone. The leaner (C2) flame configurations appear to have the larger reaction transfer function gain values of the flame configurations studied. The low swirl intensity and lean S009-C2 flame configuration in Figure 4.15b is characterized by the highest reaction transfer function gain values.

The reaction transfer function phase curves in Figure 4.15b also illustrates that the flame configurations with the most in-phase pressure and heat release rate perturbations are the leaner (C2) flames. These flames are characterized by phase angles in the shaded region of the transfer function phase in the range of $-90 \leq \phi_R \leq +90$. This result is in agreement with the phase conditioned results discussed in section 4.6.2 where lean flames were observed to be highly susceptible to acoustic forcing.

The HT-FFT based global transfer function *G(f)* of Figure 4.15c represents a linear combination of the mixing and reaction transfer function. The global transfer function directly relates the velocity perturbations velocity ($\hat{u}$) to the heat release rate ($\hat{q}$) perturbations as the input and output of the flame dynamics process. Figure 4.15c has a large number of lean (C2) flames within the shaded in-phase perturbation region of $-90 \leq \phi_G \leq 90$. These leaner (C2) flames also possess higher *G(f)* gain values compared to the richer (C1) flame configurations. A reduction in

the global transfer function gain is obtained with increased swirl intensity for lean (C2) flames but an increase is observed in the G(f) gain values for richer (C1) flame configurations.

The flame transfer functions analysis of Figure 4.15 suggests that the previously identified responsive flames with positive flame response indices are indicative of configurations with heat release rate ($\hat{q}$), velocity ($\hat{u}$) and burner exit ($\hat{p}_2$) perturbations with phase relationships in the ±π/2 range. This is consistent with observations by Noiray et al. [30-31] regarding heat release rate and pressure perturbation phase angle requirements in the ±π/2 modulo 2π range for the enhancement of thermoacoustic coupling.

4.8 Acoustic Impedance Analysis

Acoustic impedance estimates at the burner exit are illustrated in Figure 4.16 for the studied flame configurations. A relatively symmetric impedance magnitude function with a 201Hz peak is obtained. The resistance (*Re(Z)*) and reactance (*Im(Z)*) components of the acoustic impedance in Figure 4.16a illustrate significant variations in the acoustic impedance composition with a strong dependence on frequency.

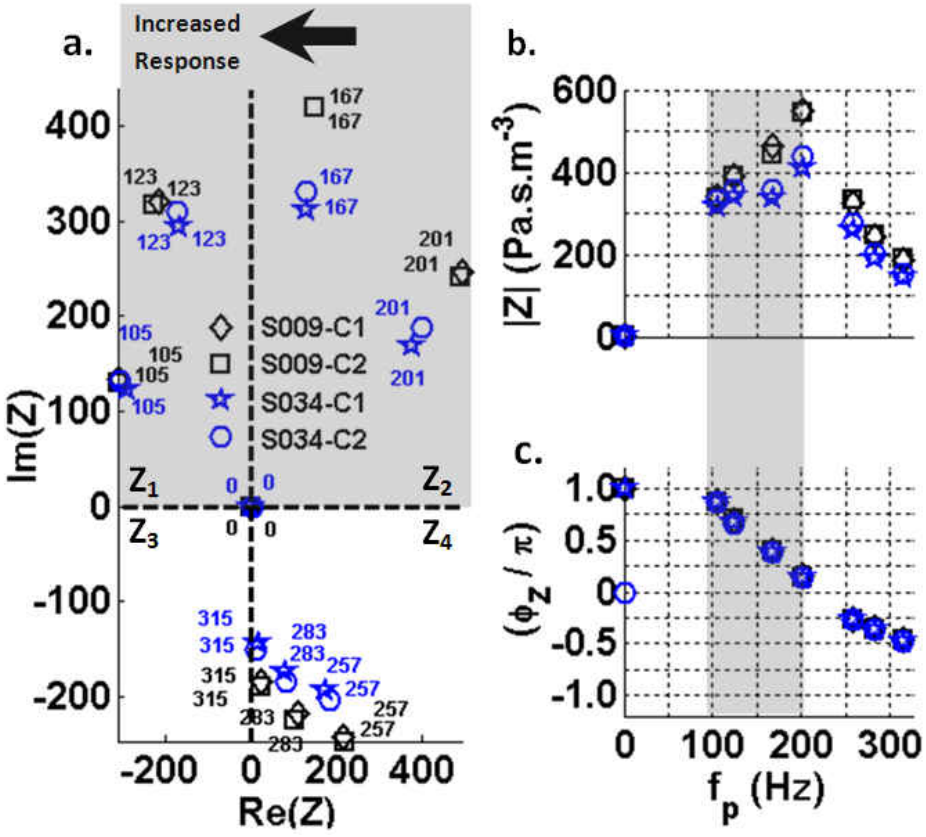

Figure 4.16: Acoustic Impedance Estimates
a. Complex Impedance Plane
b. Acoustic Impedance Magnitude $|\mathbf{Z}| = \sqrt{\mathbf{Re(Z)}^2 + \mathbf{Im(Z)}^2}$
c. Acoustic Impedance Phase $\boldsymbol{\phi_Z} = \boldsymbol{atan}\left(\frac{Im(Z)}{Re(Z)}\right)$

The real (resistance) and complex (reactance) components show the highly responsive flames confined to the positive regions of the complex plane in Figure 4.16a. The reactance is a measure of the energy conversion through various forms including kinetic and potential through periodic rarefaction and compression due to the acoustic source [53-55]. The positive reactances of flames at pulsing frequencies below 201Hz illustrate the energy absorption from the supplied acoustic perturbations. The negative resistances of the 105Hz and 123Hz flame configurations are characteristic of oscillation or amplification at these highly responsive energy releasing modes [30-31].

The flames associated with the positive reactance (energy absorption) at the 105Hz and 123Hz modes subsequently feedback energy into the system as indicated by the negative resistance values. The result is an oscillatory flame response where energy is periodically absorbed and fed back establishing highly responsive flame dynamics. The exact mechanism of the energy transfer is presently unclear although increased vortex shedding and ambient medium entrainment has been reported at highly responsive flame configuration. The reactance-resistance phase angles in Figure 4.16c are obtained using the relationship in Eq. 3.16.

The phase angles in Figure 4.16c show positive phase angles below 201Hz indicating the reactance (energy storage) process is in advance of (leads) the negative resistance (energy feedback) process for the 105Hz and 123Hz flames. Although the 167Hz and 201Hz flames exhibit a positive reactance, they are characterized by positive resistances. This implies that energy absorbed is subsequently dissipated due to the positive resistance of the flame

configurations at the burner exit. The 167Hz and 201Hz flames are also characterized by positive impedance angles in Figure 15 indicating the reactance process also leads the dissipative process in these flames. As a result, the 105Hz and 123Hz modes show the most significant flame response of all the flame configurations in the present study.

The most responsive lean flames (for 105Hz – 123Hz forcing) with very positive Flame Response Indices are located in the Z_1 acoustic impedance region in Figure 4.16a. This Z_1 region of the complex impedance plane also contains the richer (C1) flames with negative (minimally responsive) Flame Response Indices from Figure 4.9. This implies that the acoustic impedance must be combined with the Flame Response Index to identify the flame configurations susceptible to thermoacoustic coupling.

In addition to a flame located in the Z_1 region of the complex impedance plane, a phase difference of $-90 \leq \phi_G \leq 90$ between the heat release rate ($\hat{q}$) and velocity ($\hat{u}$) perturbations is necessary to trigger a significant flame response. This phase requirement is alternatively stated as a positive (R>0) Flame Response Index in addition to a negative resistance component of the acoustic impedance.

4.9 Continuous Wavelet Transform (CWT) Spectra

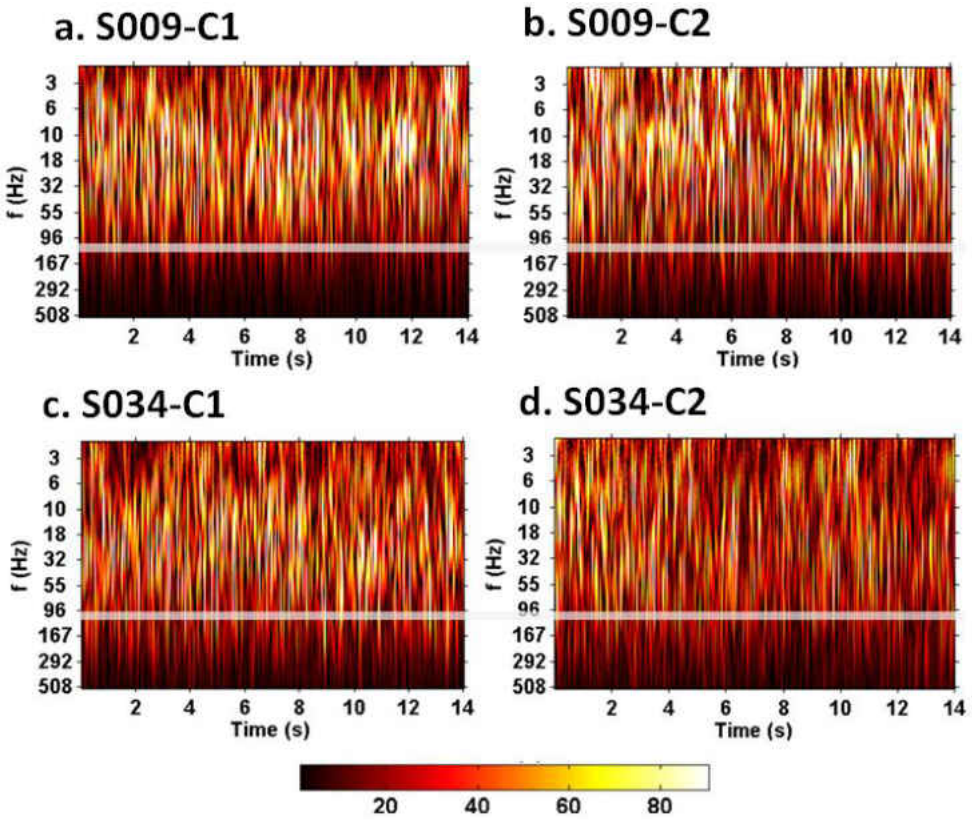

Figure 4.17: CH* Chemiluminescence Intensity CWT Spectra – Unpulsed (f_p = 0Hz)
a. S009-C1-0Hz (Unpulsed) | b. S009-C2-0Hz (Unpulsed)
c. S034-C1-0Hz (Unpulsed) | d. S034-C2-0Hz (Unpulsed)

The heat release perturbation (q') continuous wavelet transform spectra for the unpulsed constant fuel flow rate (C1 and C2) flames are presented in Figure 4.17. The wavelet spectra illustrate the dominant frequencies over the 14s data sample period. The provided index maps the magnitude of the wavelet coefficients that are proportional to the power of the respective frequency at each time instant. A larger (brighter) wavelet coefficient at a specific frequency implies increased dominance of the pertinent frequency at the specific time instant [86]. A

reference line provided at the 96Hz frequency in Figure 4.17 illustrates the increased prominence of heat release oscillations above 96Hz at higher swirl (S034) intensities for the unpulsed (f_p = 0Hz) flames across both fuel flow rates.

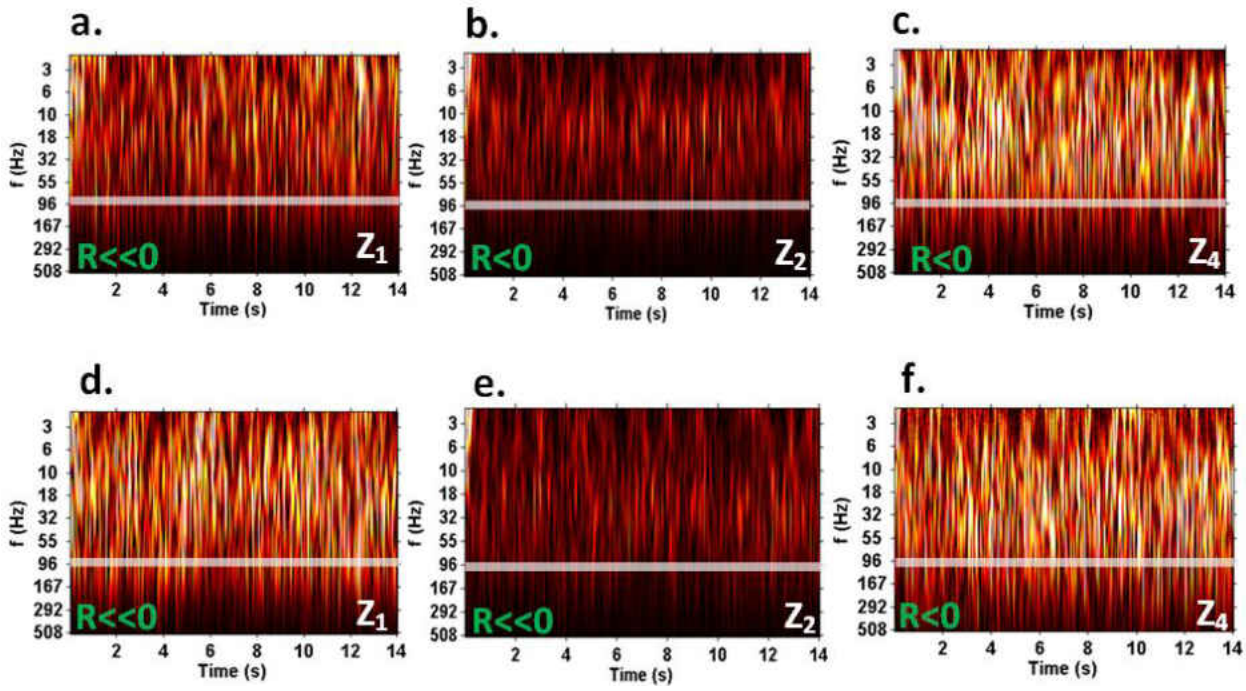

Figure 4.18: CH* Chemiluminescence Intensity CWT Spectra – Forced Rich (C1) Flames
a. S009-C1-105Hz | b. S009-C1-167Hz | c. S009-C1-315Hz
a. S034-C1-105Hz | b. S034-C1-167Hz | c. S034-C1-315Hz
R – Flame Response Index from Figure 4.9
Zn – Flame Locations in Complex Acoustic Impedance Plane of Figure 4.16

The introduction of the acoustic pulsing yields the different heat release rate wavelet spectra illustrated for rich (C1) flames in Figure 4.18 for 105Hz, 167Hz and 315Hz forcing modes. The location of each flame (Z_n) in the complex impedance plane of Figure 4.16 is indicated. The Flame Response Index of each configuration is also provided based on the illustrated values in Figure 4.9. In general, high frequency heat release rate oscillations are observed at higher swirl in Figure 4.18 as was the case for the unpulsed flames in Figure 4.17.

In Figure 4.18, the intensities of heat release rate oscillations (magnitude of wavelet coefficients) are dampened at the 105Hz pulsing mode in comparison with the previously discussed unforced flames. The high swirl forced flame in Figure 4.18d exhibits higher intensities than the low swirl forced flame in Figure 4.18a. The cause can be traced to the Global Transfer Function *G(f)* illustrated in Figure 4.15c relating velocity ($\hat{u}$) to the heat release rate ($\hat{q}$) perturbations.

The *G(f)* phase curves of Figure 4.15c show a phase angle of +180^{o} between the velocity and heat release perturbations for the S009-C1 flame pulsed at 105Hz. The corresponding phase angle from Figure 4.15c for the S034-C1 flame pulsed at 105Hz is -135^{o}. This demonstrates the dependence of the flame response on the actually phase lag between velocity ($\hat{u}$) to the heat release rate ($\hat{q}$) perturbations even though the Flame Response Index provide a qualitative description of the phase relationship.

Examining the heat release rate CWT spectra for the 167Hz forced flames in Figure 4.18b and 4.18e illustrate the effect of the *G(f)* gain between velocity ($\hat{u}$) and heat release rate ($\hat{q}$) perturbations. Unlike the 105Hz forced flames, low intensity oscillations characterize the 167Hz forcing mode at both swirl intensities. The phase angles of both the S009-C1 and the S034-C1 flames are (ϕ = -180^{o}) and (ϕ = +135^{o}) in Figure 4.15c respectively. At the 167Hz forcing mode, the gain value of the S009-C1 flame is the lowest across all forcing frequencies in the *G(f)* transfer function plot of Figure 4.15. A similarly low velocity ($\hat{u}$) and heat release rate ($\hat{q}$) gain characterizes the 167Hz S034-C1 flame in Figure 4.15. The low gain combined with out of phase

velocity ($\hat{u}$) and heat release rate ($\hat{q}$) perturbations results is the muted CWT spectra observed for the 167Hz forcing mode.

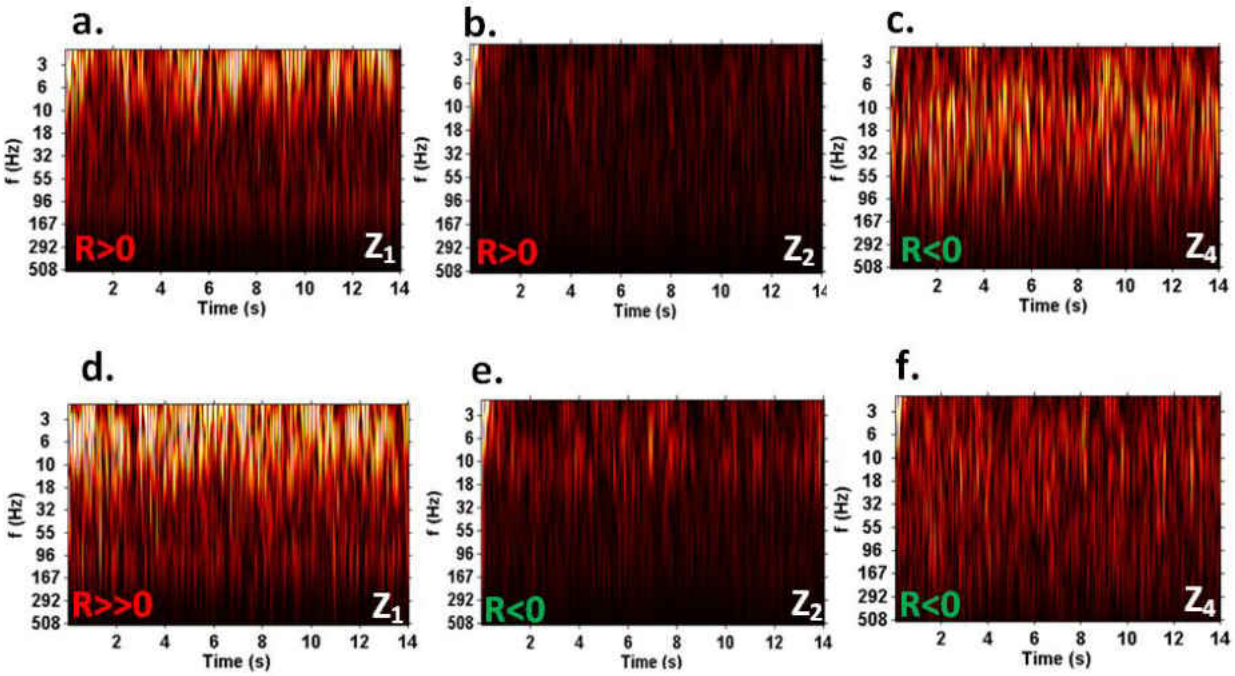

Figure 4.19: CH* Chemiluminescence Intensity CWT Spectra – Forced Lean (C2) Flames
a. S009-C2-105Hz | b. S009-C2-167Hz | c. S009-C2-315Hz
a. S034-C2-105Hz | b. S034-C2-167Hz | c. S034-C2-315Hz
R – Flame Response Index from Figure 4.9
Zn – Flame Locations in Complex Acoustic Impedance Plane of Figure 4.16

The CWT spectra for the leaner (C2) flames in Figure 4.19 are characterized by some different phenomena from the rich (C1) flames. The CWT spectra at the 105Hz acoustic forcing frequency in Figure 15 exhibit strong 3Hz – 15Hz heat release pressure oscillations present in the flame throughout the data acquisition period. Also immediately evident is the increase in the intensity of these low frequency heat release perturbations ($\hat{q}$) at the higher swirl (S034) intensity.

Once again, the phase curves for the S009-C2 and S034-C2 flames in Figure 4.15c explain the physical mechanism behind this increase in intensity. At a frequency of 105Hz, the S009-C2 flame configuration has relatively in-phase (ϕ = -90^o) velocity ($\hat{u}$) and heat release rate ($\hat{q}$) perturbations. At the higher swirl intensity level, the S034-C2 flame is characterized by a lower phase lag (ϕ = -45^o) between the velocity and heat release perturbations. Figure 4.15c shows both flame configurations with relatively equivalent gain values. As a result, more intense heat release perturbations are observed for the S034-C2 flame in the CWT spectra of Figure 4.19.

The impact of the acoustic impedance on the flame response is readily illustrated in the CWT spectra of the 167Hz forcing mode in Figure 4.19. The S009-C2 flames in Figure 4.19b is characterized by a *positive* (R>0) Flame Response index indicating relatively *in-phase* velocity ($\hat{u}$) and heat release rate ($\hat{q}$) perturbations. Figure 4.15c also shows a phase difference of approximately +20^o validating the Flame Response Index value along with *G(f)* gain values comparable to the 105Hz lean (C2) flames. However, the CWT of this flame in Figure 4.19b is characterized by very low intensity oscillations.

The 167Hz S009-C2 flame in question is located in the Z_2 region of the complex acoustic impedance plane of Figure 4.16. The low intensity 167Hz S009-C2 flame modal response in spite of comparable gain and relatively *in-phase* velocity ($\hat{u}$) and heat release rate ($\hat{q}$) perturbations appears to be the result of the positive Re(Z) resistance and positive Im(Z) reactance nature of its complex acoustic impedance. A positive resistive impedance component is characteristic of passive, energy dissipative flame configurations [30-31]. This is in contrast to the negative

resistance / positive reactance flames in the Z_1 region of the complex impedance plane characterized by actively oscillating, energy producing flame responses. Thus, in spite of comparable gain, a positive Flame Response Index (R>0) and relatively *in-phase* velocity ($\hat{u}$) and heat release rate ($\hat{q}$) perturbations, the 167Hz S009-C2 flame exhibits the minimally intensive CWT spectra in Figure 4.19b.

There are some similarities between the CWT spectra of the richer (C1) flames in Figure 4.18 and leaner (C2) flames in Figure 4.19. A low intensity ($\hat{q}$) CWT spectra for acoustic pulsing at 315Hz for both swirl intensity levels is common to the two flame configurations. In the *G(f)* transfer function phase curves of Figure 4.15c, we again observe an approximately -180^{o} phase difference between the *phase* velocity ($\hat{u}$) and heat release rate ($\hat{q}$) perturbations at 315Hz for both swirl intensity levels and fuel settings.

4.10 General Flame Response Criteria

The preceding analysis focused on the physical mechanisms behind the observed flame response to acoustic perturbations. Also of interest are the general criteria common to highly responsive flame configurations. In Figure 4.20, the Strouhal number defined as $St = f_p d_m / u_{avg}$ based on the burner annulus diameter and average velocity at the burner exit is estimated. The Strouhal number is a non dimensionalization of the forcing frequency relative to the nominal burner exit velocity. The highly responsive flame configurations occur in Strouhal number in the 1 – 3.5 range. The upper end of the Strouhal number range corresponds to the flame response cut-off frequency of 201Hz. This result is consistent with prior flame dynamics studies showing significant flame dynamics for Strouhal number on the order of unity [15-19, 35-36].

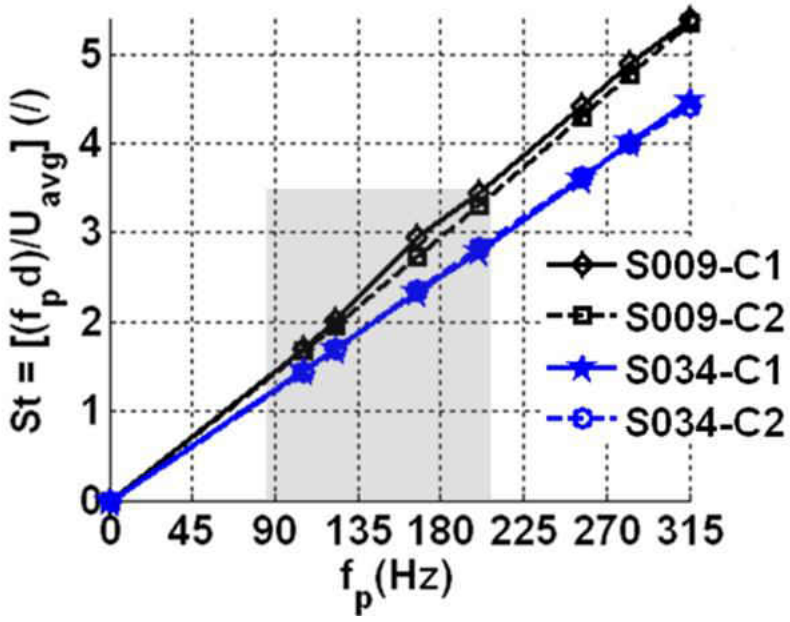

Figure 4.20: Strouhal Number Estimate

The normalized phase-conditioned velocity perturbation amplitude is illustrated in the top half of Figure 4.21. Imposing the observed the 201Hz forcing limit (analogous to $1 \leq St \leq 3.5$) yields a minimum normalized velocity perturbations amplitude of $|\langle \hat{u} \rangle| \geq 0.12$ for the highly responsive flame configurations in the present study. It is worthwhile to note that the highest velocity amplitudes in Figure 4.21 correlate with the positive reactance, negative resistance (Z_1 acosutic impedance) flames forced at 105Hz.

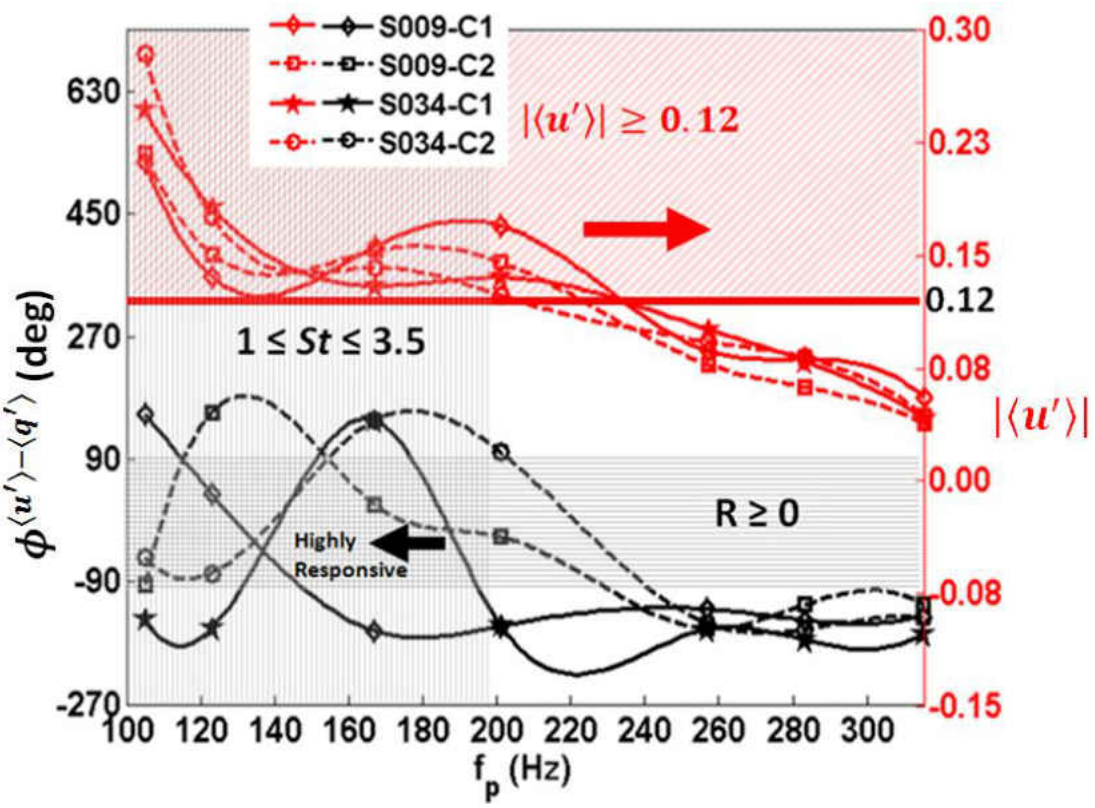

Figure 4.21: General Flame Response Criteria

An approximate $|\langle \hat{u} \rangle| \approx 1 / f_p$ relationship is readily observed for flames with a considerable flame response. Recognizing the Strouhal number as a normalized frequency, this result is similar to the $Pu \approx (1/St)$ condition observed as a necessary condition for a flame response initiation in a premixed flame configuration by Kulsheimer and Buchner [44]. In their work, the

acoustic pulsing excitation level (Pu) was defined as the rms to mean ratio of the premixed reactants' mass flow rate; analogous to the $|\langle\hat{u}\rangle|$ formulation used in the present article. It should be noted that there are minimally responsive (R <0) flame configurations that meet the $|\langle\hat{u}\rangle| \geq 0.12$ criterion in Figure 4.21. Additional criteria are therefore required to fully isolate the unstable flame configurations beyond the velocity amplitude requirement.

The additional criteria include the previously discussed velocity $\langle u'\rangle$ to heat release rate $\langle q'\rangle$ phase lag, $\phi^{\langle u'\rangle-\langle q'\rangle}$ presented in lower half of Figure 4.21. The phase relationship with forcing frequency suggests variations of the velocity to heat release time delay and requires additional investigation in light of the linear phase-frequency dependence observed by several authors [26-27, 35-37], albeit for primarily premixed flame configurations. Palies et al. [37] very recently report a mode switching effect of swirl intensity variations induced by azimuthal velocity perturbations propagating at the bulk axial velocity. This suggests that some nonlinearities may be present in the phase-frequency dependency particularly for the non-premixed flames in the present study.

All highly responsive (R ≥ 0) flames are located in the shaded $-90^{o} \leq \phi^{\langle u'\rangle-\langle q'\rangle} \leq 90^{o}$ band illustrated in the lower region of Figure 4.21 with the most responsive flames at the lower end of the forcing frequency domain. An equivalent to the $\phi^{\langle u'\rangle-\langle q'\rangle}$ phase difference specification is the time delay ($\tau^{\langle u'\rangle-\langle q'\rangle}$) normalized by the acoustic pulsing signal period, $T_p = 1/(2\pi f_p)$. This yields an alternative phase difference requirement for highly responsive flame configurations that may be stated as $\left|\tau^{\langle u'\rangle-\langle q'\rangle}\right| \leq 1$.

4.11 Concluding Remarks

The effect of swirl intensity and fuel flow rate variations on the response of relatively lean and rich non-premixed swirling flames acoustically perturbed at varying frequencies up to 315Hz was studied using an atmospheric burner. The time-averaged flame response data and CH* chemiluminescence images show highly responsive flame dynamics below a cut-off acoustic pulsing frequency of approximately 201Hz. A diminishing flame response is observed beyond 201Hz with further increase in pulsing frequency. A summary of the observed flame dynamics is illustrated in Figure 4.22.

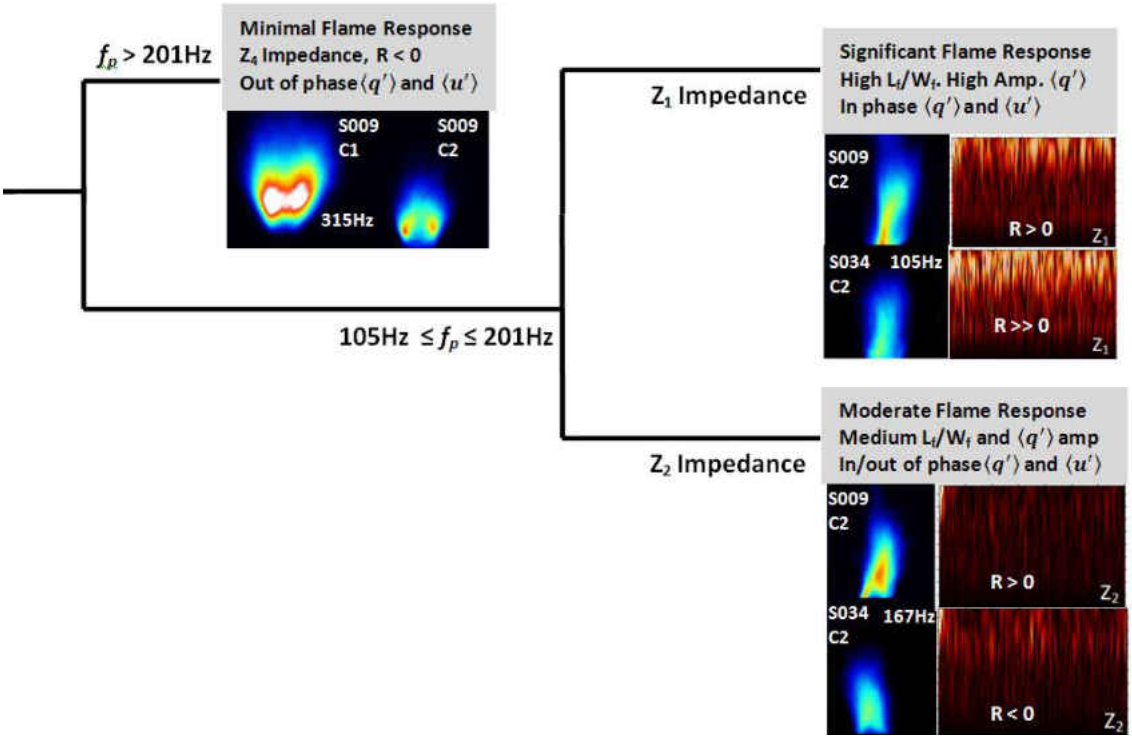

Figure 4.22: Flame Response Summary
R – Flame Response Index Illustrated in Figure 4.9
Zn – Flame Location in Complex Impedance Plane of Figure 4.16

The 201Hz boundary appears to be a result of the changes in the acoustic impedance of the flame above and below this boundary. Flames subject to pulsing frequencies between 100Hz and 201Hz were characterized by significant amplification in flame height, surface area and aspect ratio.

Increased swirl intensities and the introduction of acoustic forcing both resulted in lower flame liftoff heights. A reduction in the phase lag of the heat release rate perturbations $\langle q' \rangle$ relative of the forcing signal was also observed at higher swirl intensities. This resulted in in-phase and $\langle u' \rangle$ perturbations at the 105Hz mode and out of phase $\langle q' \rangle$ and $\langle u' \rangle$ perturbations at the 167Hz mode. Leaner flames at low swirl were observed to be characterized by a positive flame response index at the 105Hz and 167Hz pulsing modes. In spite of in-phase $\langle q' \rangle$ and $\langle u' \rangle$ perturbations, only flames with acoustic impedances characterized by a negative resistive component resulted in an oscillatory response exhibiting intense low frequency $\langle q' \rangle$ oscillations.

The studied flames were observed to be subject to the following requirements for the initiation and propagation of highly responsive flame dynamics:

- A Strouhal number requirement: $1 \leq St \leq 3.5$
- A velocity perturbation amplitude: $|\langle \hat{u} \rangle| \geq 0.12$;
- A $\langle q' \rangle$ to $\langle u' \rangle$ perturbation phase : $-90^{o} \leq \phi^{\langle u' \rangle - \langle q' \rangle} \leq 90o$
- A complex acoustic Impedance (Z): Re(Z) < 0, Im(Z) > 0

CHAPTER 5 TRANSIENT FLAME RESPONSE AND EXTINCTION DYNAMICS

5.1 Localized Flame Extinction / Reignition

The CCD images of CH* chemiluminescence reveals additional transient flame response phenomena not captured by the previously discussed time averaged analysis. Figure 5.1 illustrates the flame geometry between t = 6.000s and t = 6.875s for flames with no acoustic pulsing (f_p = 0Hz). Both flames in Figure 5.1a are at the same fuel flow rate but comparing rich (C1) flames reveals more intense CH* intensity at the higher (S034) swirl level. This is a verification of the more intense combustion and higher mixedness levels present in the higher swirl intensity flame. In Figure 5.1, the higher swirl intensity flames are characterized by low aspect ratios (height/width) in comparison with the low swirl intensity flames.

As observed in the time averaged results, the leaner (C2) flames in Figure 5.1b are smaller in area in comparison to the richer (C1) counterparts. In addition, the lean (C2) flames in Figure 5.1b are characterized by the periodic extinction of localized regions in the flame sheet particularly at the low swirl (S009) intensity level. This localized extinction is absent in the rich (C1) flames of Figure 5.1a. The periodic localized extinction phenomena are also present albeit to a lesser extent at the higher swirl intensity lean (S34-C2) flame. The flames in Figure 5.1 are not acoustically perturbed implying that localized flame extinction and restoration must be associated with natural coupling modes specific to the lean flames. The CCD images in Figure 5.1 suggest the localized flame extinction is exacerbated at low swirl levels.

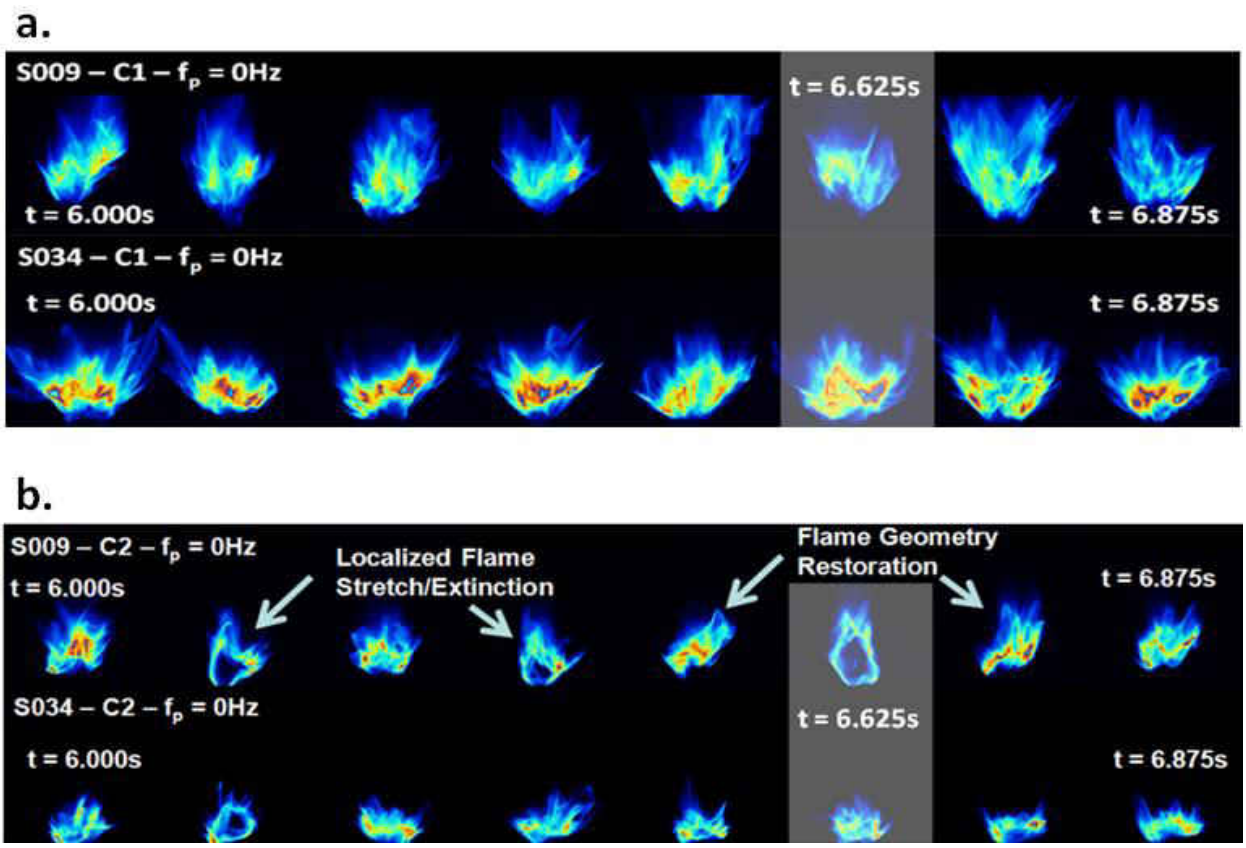

Figure 5.1: Transient CH* Chemiluminescence Images | f_p = 0Hz (Unpulsed)
a. Rich (C1) Flame | b. Lean (C2) Flame

In order to investigate the flame dynamics related to the observed localized extinction, the time trace of the heat release (q') and velocity (u') perturbations are illustrated in Figure 5.2 for the highlighted rich (C1) flames in Figure 5.1a. The pressure to velocity perturbation ratios at the burner exit (p_2'/u') and base of the burner (u'/p_1') are also plotted. This is in order to obtain a detailed look at the variations in the flames response parameters leading to the localized flame extinction observed in Figure 5.1. The ratios can be considered time domain equivalents of the mixing transfer function and a burner acoustic transfer function relating pressure perturbations at the base of the burner to the velocity perturbations at the burner exit. The shaded region in Figure 5.2 encompasses the period from the image acquisition trigger at t = 6.625s through the

10ms exposure capture window during which the CCD camera aperture is opened for the CH* intensity image acquisition. The bottom half of Figure 5.2 illustrate the continuous wavelet transform (CWT) spectra of the heat release rate perturbations (q') over the CH* image acquisition.

The time traces reveal similar velocity oscillations in the rich (C1) flames in Figure 5.2. The low swirl (S009) heat release rate (q') time trace exhibits large amplitude oscillations that are not present in the corresponding high swirl flame in Figure 5.2b. The burner exit pressure (p_2') perturbations are also much higher in the low swirl (S009-C1) flame of Figure 5.2a leading to large amplitude oscillations at the beginning of the 10ms CCD exposure window. These large amplitude p_2'/u' oscillations are absent in the high swirl flame revealing the stabilizing mechanism resulting from higher swirl. Large pressure oscillations are symptomatic of strong radiation from combustion noise due to flame surface are losses [6-7, 30-31]. This suggests a dampening of the combustion noise due to the lower p_2' oscillations at the S034 swirl level in the rich (C1) flames of Figure 5.2

The CWT spectra of the two swirl intensity flames in Figure 5.2 exhibit some similarity over the exposure window. However, strong low frequency (3Hz – 11Hz) heat release rate oscillations are present in the S034-C1 flame. Similarly dominant low frequency oscillations are absent in the CWT for the lower swirl S009-C1 flame. The CH* images of Figure 5.1a illustrates that the rich (C1) flames whose time traces are illustrated in Figure 5.2 do no exhibit the localized flame

extinction observed in the lean (C1) flames of Figure 5.1b. Thus the time traces of the lean flames need to be examined for localized extinction characteristics.

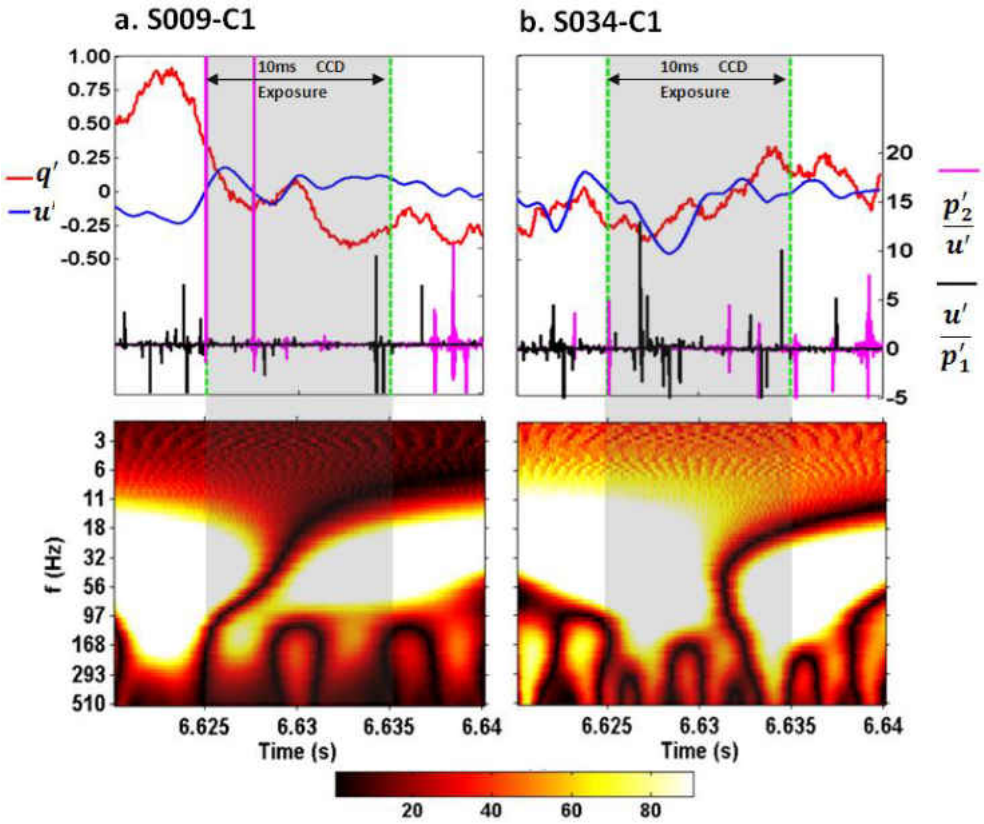

Figure 5.2: Signal Time Trace and *q'* CWT for Rich (C1) CH* Images of Figure 5.1a | f_p = 0Hz Time Period: t = 6.625s through t = 6.635s

The most prominent localized flame extinction events in Figure 5.1 occur for the lean, low swirl S009-C2 flame. In Figure 5.3, the time traces for this flame is characterized by more frequent higher amplitude p_2'/u' spikes during the flame image acquisition window. These large amplitude p_2' oscillations in the lean (C2) flames of Figure 5.3 are reduced at the high swirl intensity. This was also the case in the rich (C1) flames of Figure 5.2. These observations validate the noise reduction / stabilization that characterize the higher swirl flames independent of the fuel flowrate.

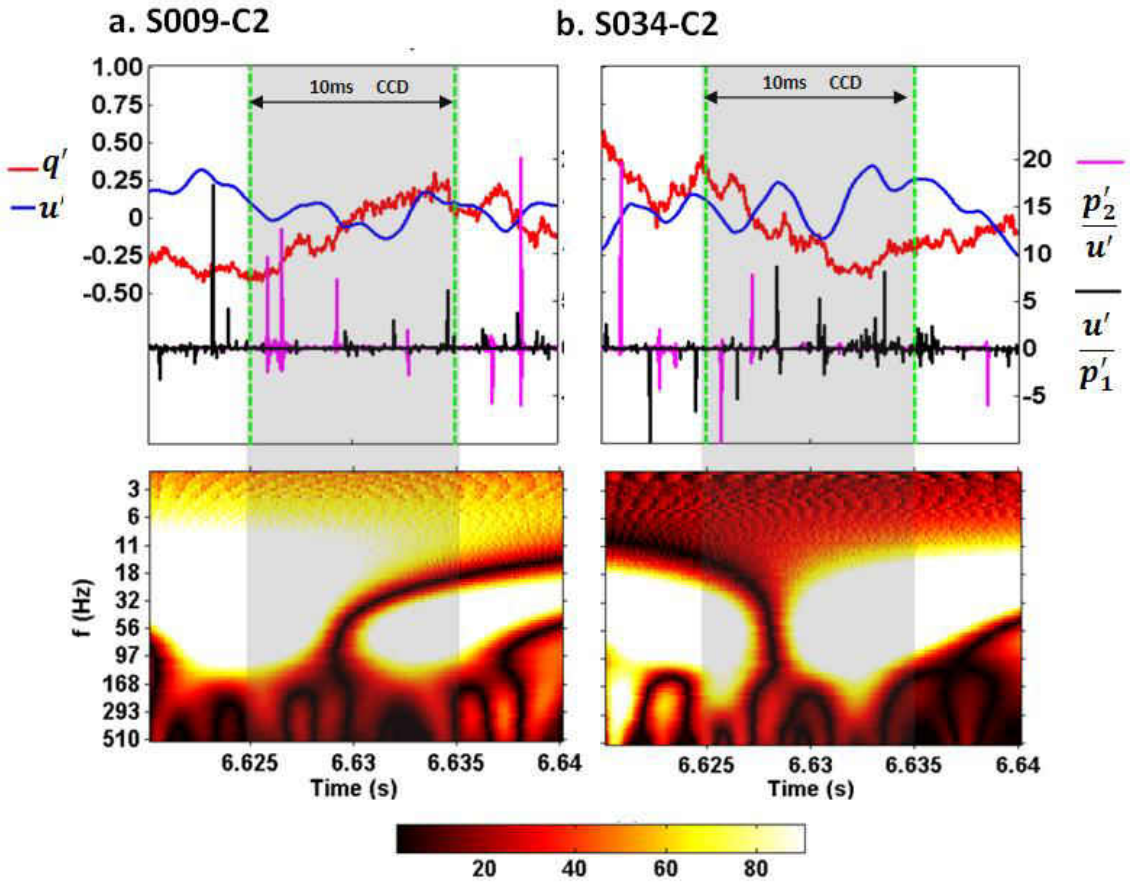

Figure 5.3: Signal Time Trace and *q'* CWT for Lean (C2) CH* Images of Figure 5.1a | f_p = 0Hz
Time Period: t = 6.625s through t = 6.635s

Figure 5.3 illustrates intense low frequency (3Hz – 11Hz) heat release rate (*q'*) perturbations in the CWT spectrum of the S009-C2 flame. These low frequency *q'* perturbations were previously observed to be excited under acoustic forcing in the CWT spectra of highly responsive flames in Figure 4.19. The previous discussion showed that the presence of these low frequency q' perturbations was symptomatic of strained high aspect ratio flames from the imposed acoustic forcing. It is then possible to suggest the presence of high strain the low swirl lean (S009-C2) flame in Figure 5.3a. The low swirl intensity would then mean a weakened ability to resist the periodic straining of the flame. It appears that the compact nature of the flame at higher swirl

intensity provides the S034-C2 flame in Figure 5.3b with a higher resistance to the induced strain. This leads to a lower occurrence of the localized extinction of the S034-C2 flame sheet as observed in Figure 5.1b.

The transient flame dynamics suggest two possible mechanisms to reducing the occurrence of the observed localized flame extinction. The first is the application of a higher fuel flowrate or making the flame richer. This observation is based on the CWT spectra in Figure 5.2b where low frequency 3Hz-11Hz heat release rate oscillation are observed for the S034-C1 flame. There is no localized flame extinction phenomena in the CH* image of the flame in Figure 5.1a. This suggests the higher swirl and/or the higher fuel flow rate prevented the occurrence of any localized flame extinction events.

The second apparent mechanism for avoiding localized flame extinction includes increasing the swirl intensity. This observation is based on the CH* images of figure 5.1b which illustrate less severe localized flame extinction for the higher swirl S034-C2 flame in comparison to the low swirl S009-C2 flame. The S009-C2 and the S034-C2 flames in figure 5.1b are also at the same fuel flowrates. This further validates the inference drawn about the prevention of localized extinction by increasing the swirl intensity.

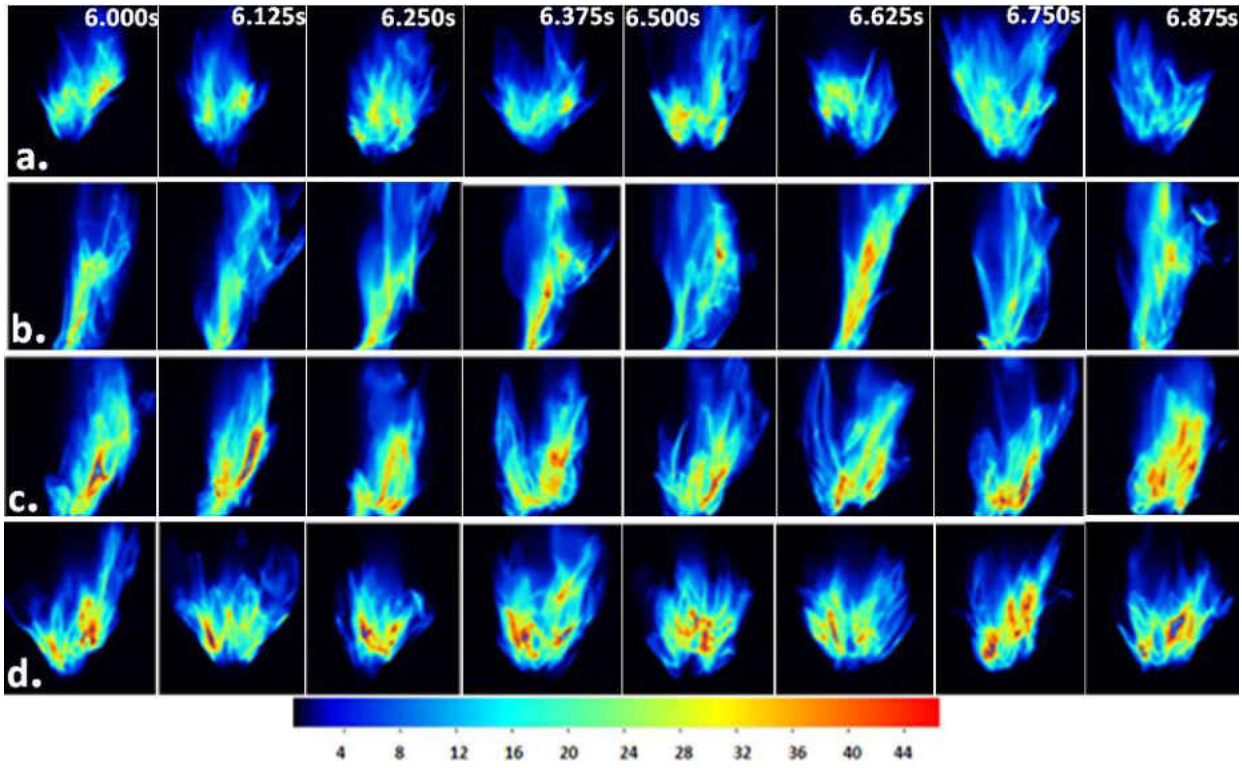

Figure 5.4: Transient CH* Chemiluminescence Images – S009-C1
a. S009-C1-0Hz | b. S009-C1-105Hz | c. S009-C1-201Hz | d. S009-C1-315Hz

Transient CH* chemiluminescence images over a sample time period of 6.000s – 6.875s are presented across representative forcing frequencies in Figure 5.4 through Figure 5.7. The highest CH* intensities are exhibited by the rich (C1) flames at both swirl intensities. The highest heat release rates are obtained with the combination of rich fuel flowrates and high swirl in the S034-C1 flames of Figure 5.6. These are in agreement with the previously discussed time averaged results. Leaner (C2) flames are characterized by a zero lift off height (attachment to the burner) with the application of acoustic forcing. Leaner and low swirl flames exhibit the previously discussed localized flame extinction and reignition. Increased swirl intensity is observed to dampen the occurrence of these localized flame extinction and reignition.

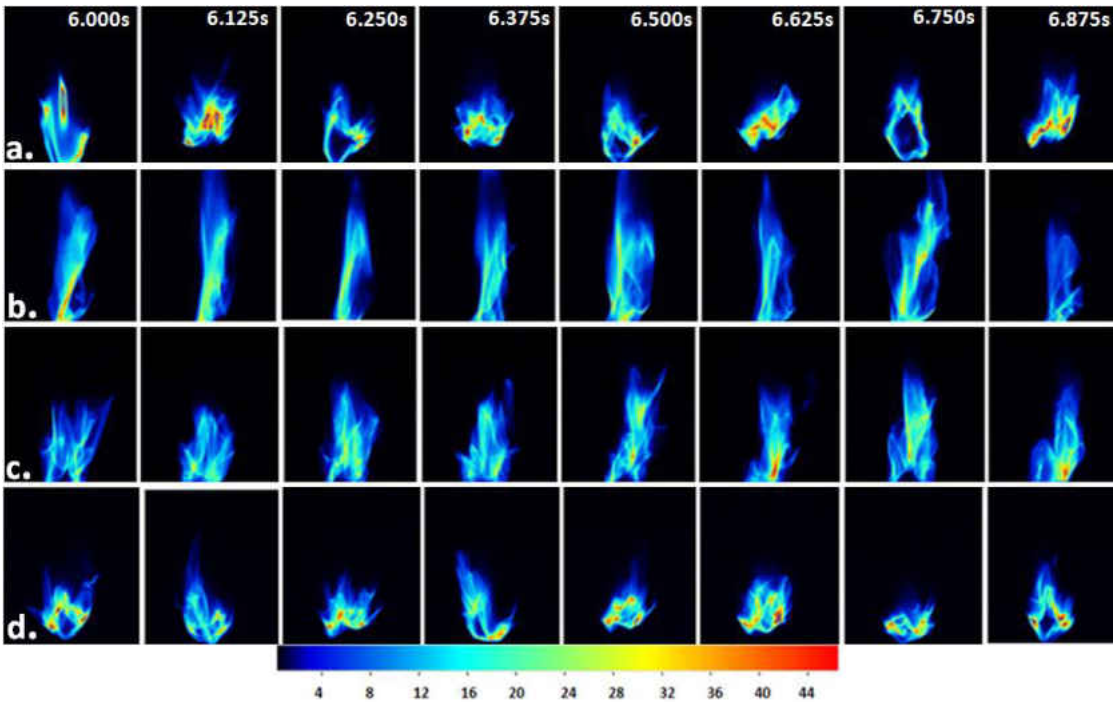

Figure 5.5: Transient CH* Chemiluminescence Images – S009-C2
a. S009-C2-0Hz | b. S009-C2-105Hz | c. S009-C2-201Hz | d. S009-C2-315Hz

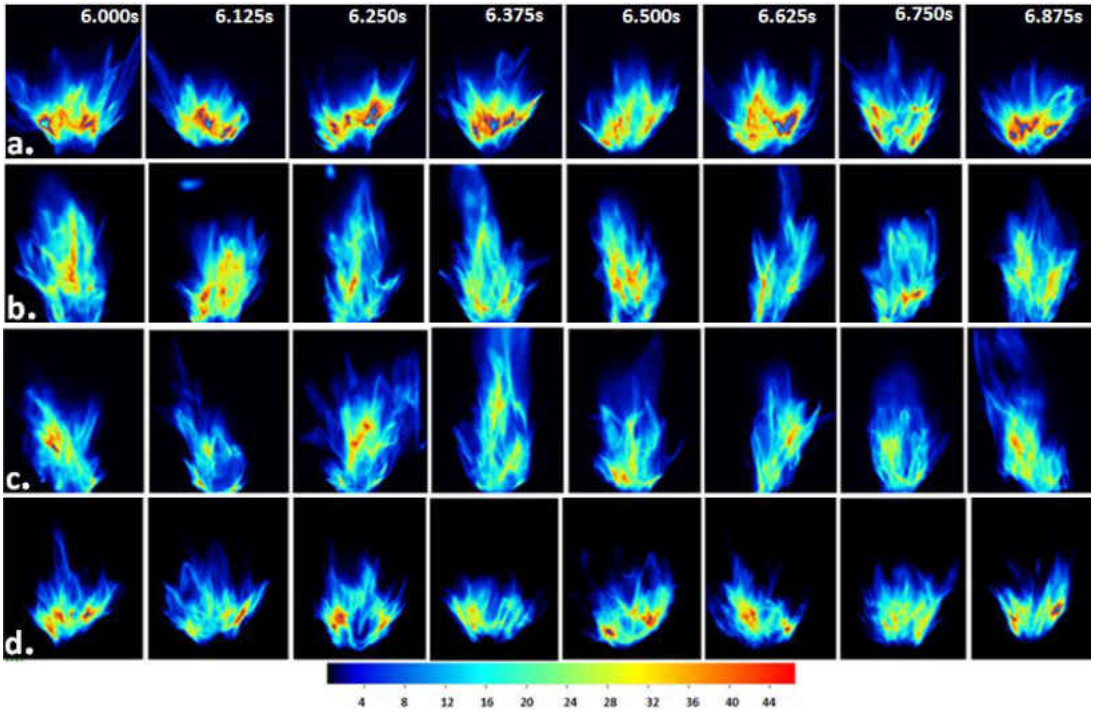

Figure 5.6: Transient CH* Chemiluminescence Images – S034-C1
a. S034-C1-0Hz | b. S034-C1-105Hz | c. S034-C1-201Hz | d. S034-C1-315Hz

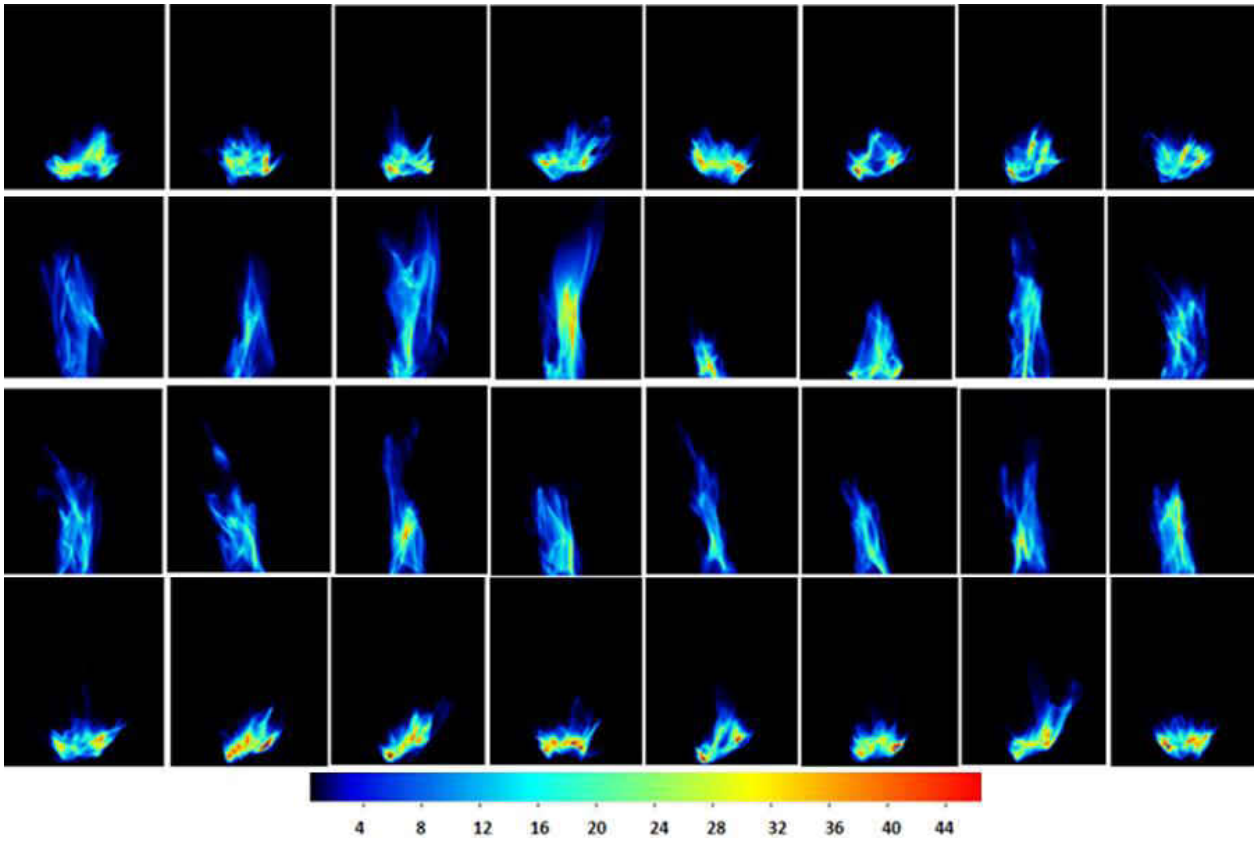

Figure 5.7: Transient CH* Chemiluminescence Images – S034-C2
a. S034-C2-0Hz | b. S034-C2-105Hz | c. S034-C2-201Hz | d. S034-C2-315Hz

5.2 Flame Response with Global Extinction from Decaying Fuel Flowrates (C3 Flames)

The third fuel flow rate condition detailed in Table 2 involved the dynamic variation of the fuel flow rate using a decay function until flame extinction was achieved. The exponential fuel flowrate decay function was illustrated in Figure 3.4. The exponential decay constant (λ) is selected to result in a fuel flowrate of 10% of the baseline in Table 1 at the end of the 14s data acquisition period. This 10% value ensures flame extinction for all the flame configurations in the present study. The primary focus in this section is the impact of swirl intensity on the flame response to acoustic forcing as the flame approaches global extinction.

5.2.1 Power Spectrum Analysis

The FFT spectrum of the heat release rate ($\hat{q}$) perturbations in Figure 5.8 illustrate a strong peak at the pulsing frequency for acoustic forcing between 105Hz and 201 Hz. Also present is the acoustically excited 1Hz – 10Hz low frequency range that was observed in the power spectrum of Figure 4.4 and 4.5 for the constant fuel flow rate flames. In the case of the decaying fuel flow rate flames in Figure 5.8, these 1Hz – 3Hz ($\hat{q}$) perturbations are prevalent at the higher swirl intensity S034-C3 flame in Figure 5.8b.

At all forcing frequencies in the low swirl (S009) flame is a very strong peak around 0.3Hz, with the power at this mode decreasing with increasing the swirl intensity. We believe this is a result of visually observed oscillation of the flame sheet about the burner axis which periodically moves the flame partially in and out of view of the PMT tube while attached to the central fuel

pipe. This oscillation of the flame sheet about the burner axis was observed to become more prominent as the flame approaches extinction. The 0.3 Hz mode is only observed for the low swirl intensity in Figure 5.8a. The higher swirl intensity appears to stabilize the flame consequently eliminating the 0.3Hz mode.

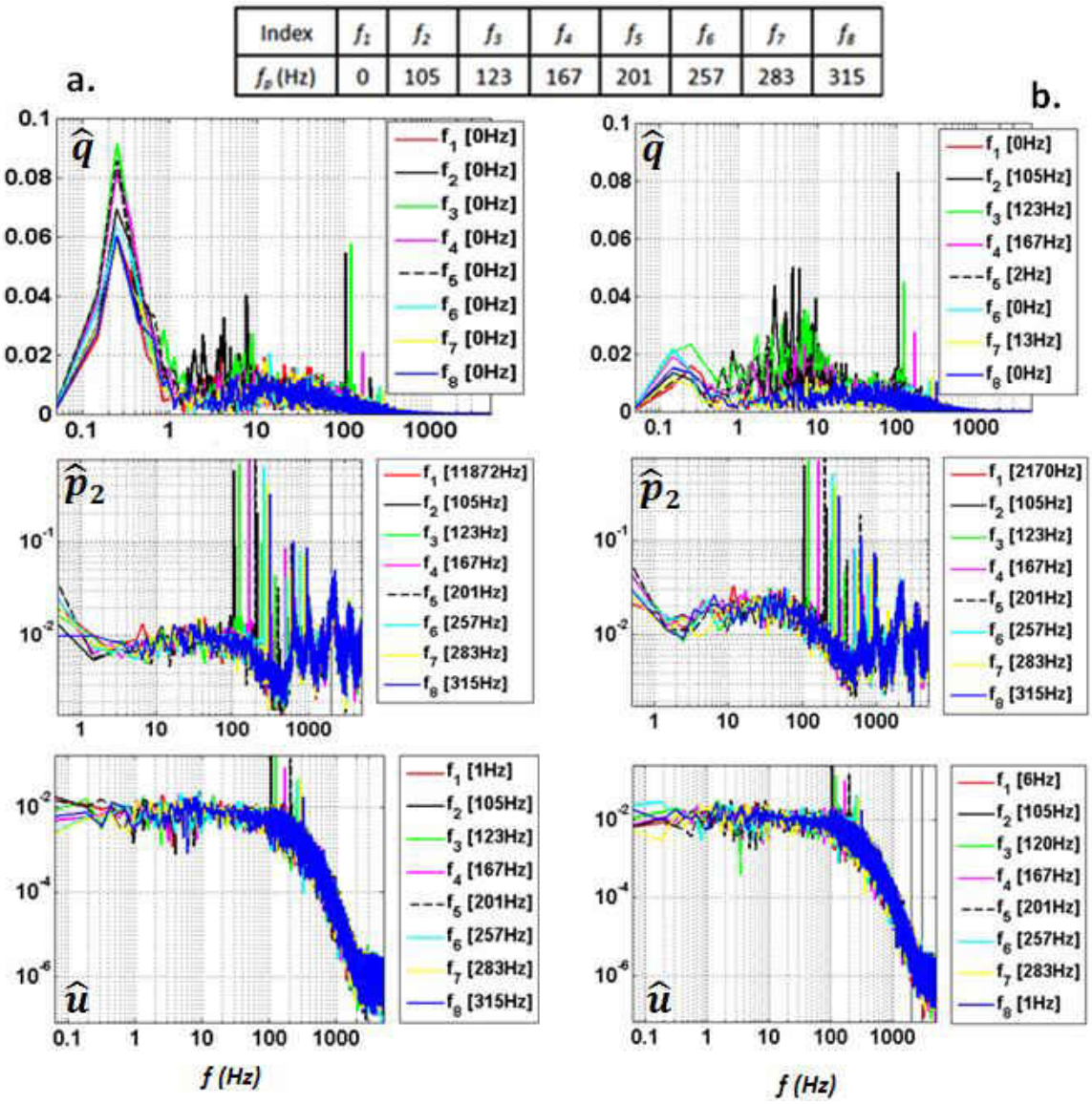

Figure 5.8: Flame Response Frequency Spectra – Decaying Fuel Flowrate (C3)
a. Low Swirl Intensity (S009) | b. High Swirl Intensity (S034)

This oscillation was also observed to be most prominent in the low swirling S009-C_3 flame and less prominent with increased swirl intensity. The heat release power spectrum in Figure 26 also supports this observation as the power of the 0.3Hz mode decreases with increasing swirl intensity. We believe this flame sheet oscillation is a result of the asymmetry in fuel concentration that results in the toroidal vortices which are important for enhanced mixing of fuel and oxidizer. Subsequent mixing studies by the authors with acetone PLIF and PIV methods will seek to further investigate this observed phenomenon.

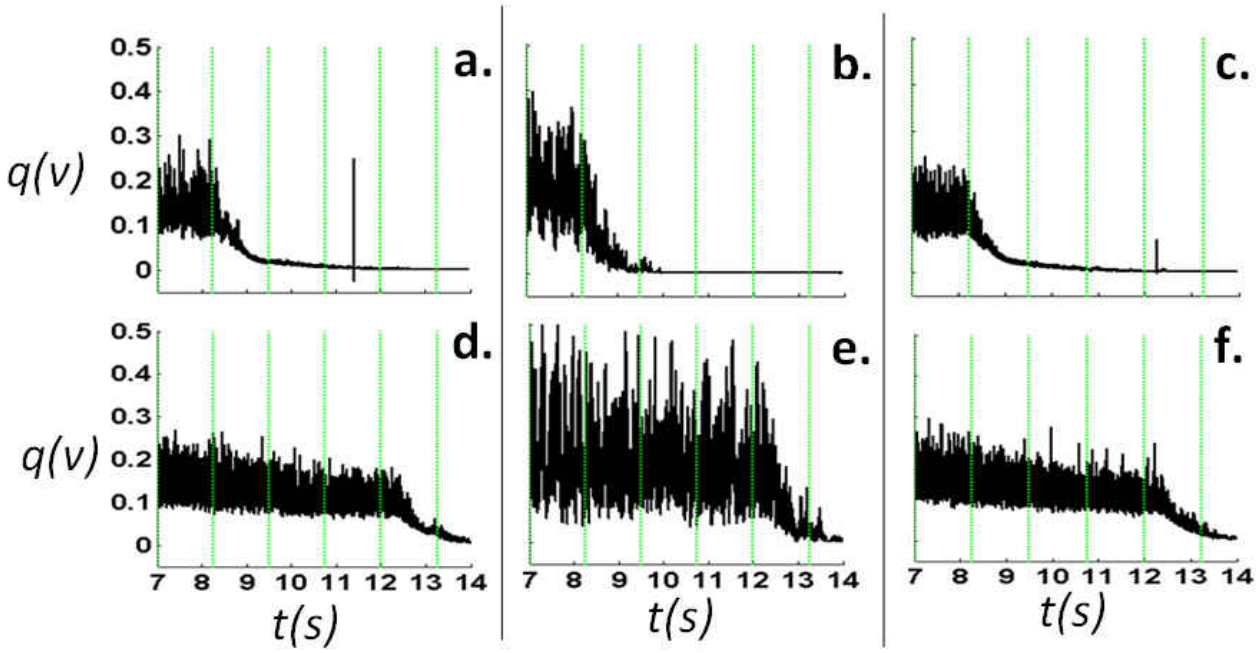

Figure 5.9: Heat Release Time Series for Decaying (C3) Fuel Flow Rates
a. S009-C3-0Hz (Unpulsed) | b. S009-C3-105Hz | c. S009-C3-315Hz
d. S034-C3-0Hz (Unpulsed) | e. S034-C3-105Hz | f. S034-C3-315Hz
Vertical Lines are Locations of CH* Chemiluminescence Images in Figure 5.10 and 5.11

5.2.2 Flame Extinction Dynamics

For this exponential decay (C3) class of flames, the heat release rate (q) time series of the low and high swirl intensity flames are presented in Figure 5.9. The vertical lines represent acquisition time instants of CH* chemiluminescence images. Immediately evident in Figure 5.9 is the spike in the heat release signal where a brief reignition of the flame occurs after the flame is seemingly extinguished. This flame reignition is observed in the unpulsed and f_p = 315Hz acoustically forced mode. This result is consistent with constant fuel flow rate (C1 and C2) flame dynamics in which the flame is observed to behave very similarly to its unpulsed mode beyond acoustic pulsing frequencies of approximately 200Hz.

At the both swirl intensity levels, Figure 5.9 illustrates the amplification in the flame heat release at the 105Hz acoustic pulsing mode. The high swirl intensity (S034) flame burns much beyond the extinction time limits of the corresponding low swirl intensity flame. This is primarily the result of the improved degree of mixedness and stability present in the higher swirl intensity flame. This observation points to the likelihood that pockets of unmixed gases are responsible for the sudden jump in the heat release signal observed at the low swirl (S009) intensity level as the flame approaches extinction.

The CH* chemiluminescence images of flames associated exponential decay fuel flow rates are presented in Figure 5.10 for low swirl and Figure 5.11 for high swirl. The relative large aspect ratio flame at the 105Hz forcing mode suggests a particularly sudden flame extinction event for the flame in Figure 5.10b. However, it is just possible to see the flame recede into the fuel pipe

at the 9.50s mark for the unpulsed flame and the 105Hz forcing mode. At a forcing frequency of 315 Hz Figure 5.10 illustrate apparent extinction of the flame at the 9.50s mark.

It is essential to recall that the unpulsed and 315Hz flames in Figure 5.10a and 5.10c are characterized by the sudden reignition event illustrated in Figure 5.9a and 5.9c. As previously mentioned, it appears the pockets of unburned reactants that tend to be prevalent at low swirl intensities may be responsible for the observed reignition events. These reignition events are not captured in the low swirl (S009) CH* images of Figure 5.10 but are readily observed in the heat release rate time series in Figure 5.9a and 5.9c.

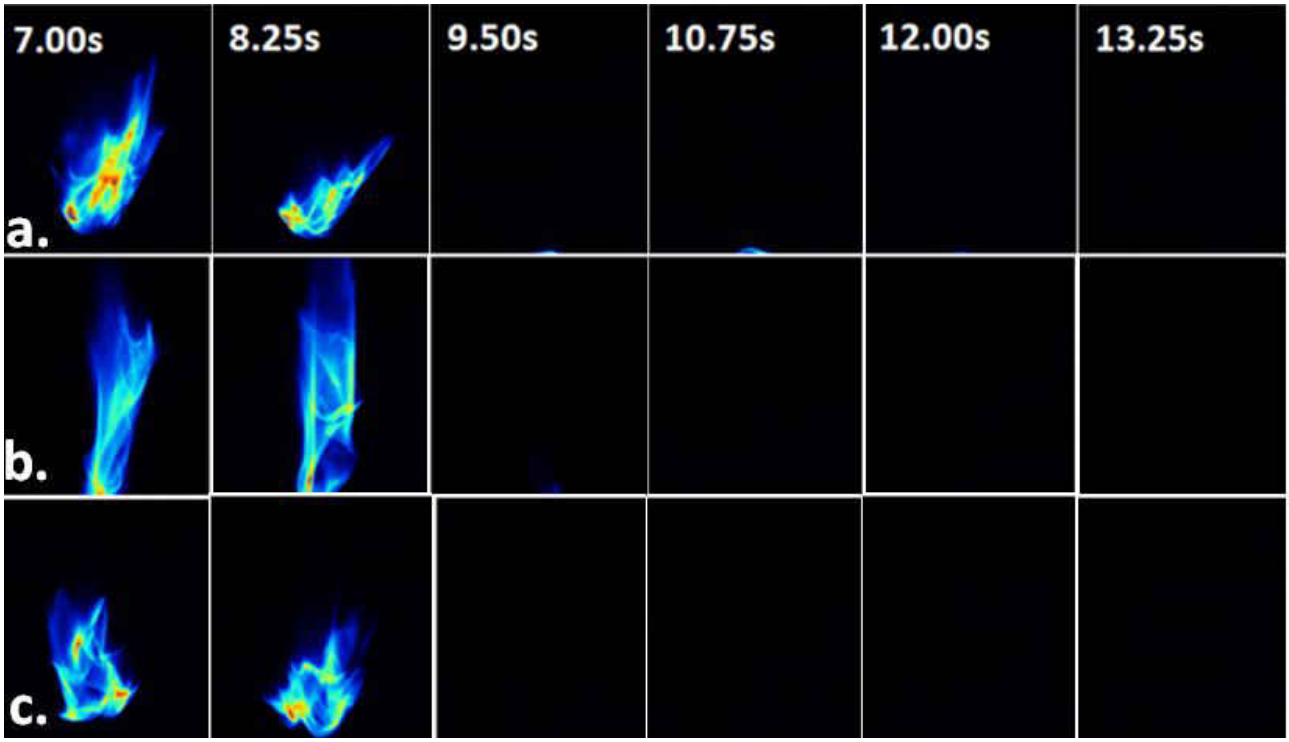

Figure 5.10: CH* Images | Exponential Decay Fuel Flowrate (C3) Flames – S009

In Figure 5.11 the C3 flames also exhibit the compact flame geometry previously observed for the constant fuel flow rate C1 and C2 flames at higher swirl intensities. The amplification in the flame surface area and aspect ratios are similar to those observed for the previous constant fuel flow rate flames for 105Hz acoustic forcing. A substantial increase in the flame burn time is readily evident for all forcing modes in the high swirl (S034) flames in Figure 5.11 The unpulsed flame at higher swirl intensity in Figure 11a appears to show the longest burn duration among all the C3 class of flames. This is a direct result of the increases mixedness levels and flame stabilization inherent at higher swirl intensities.

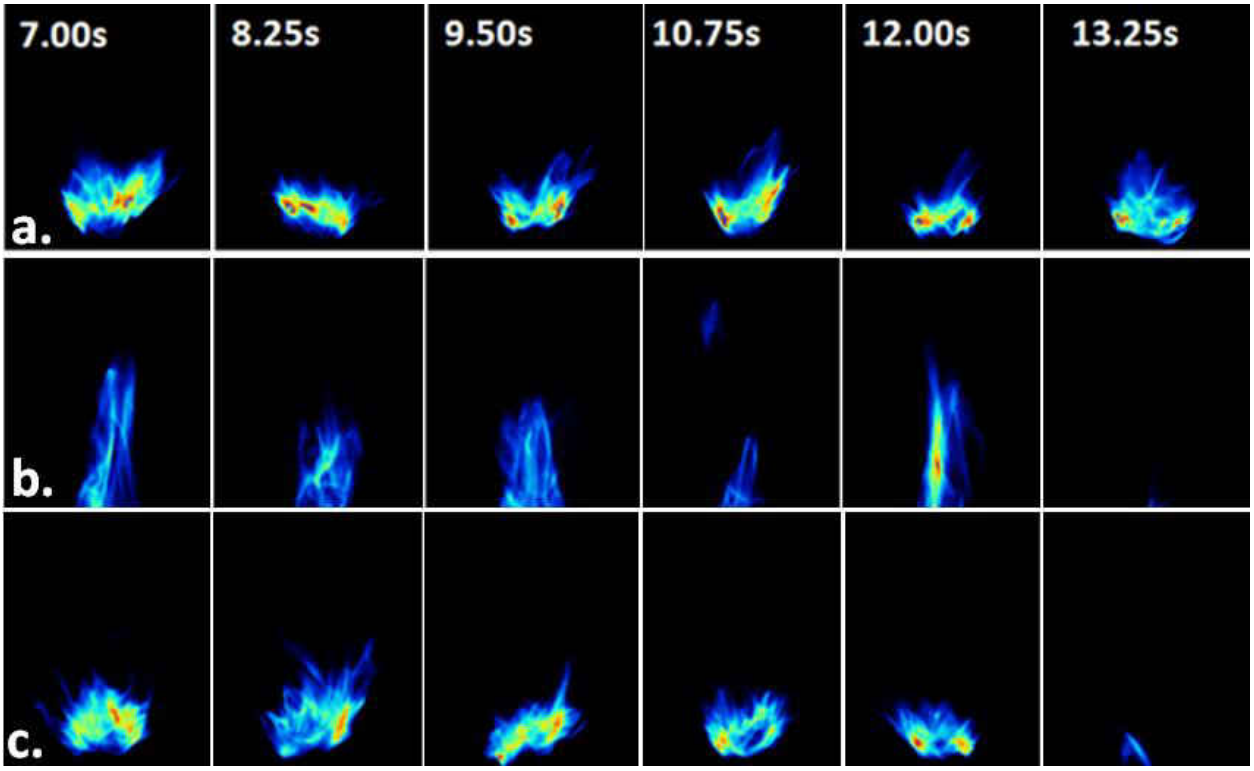

Figure 5.11: CH* Images | Exponential Decay Fuel Flowrate (C3) Flames – S034

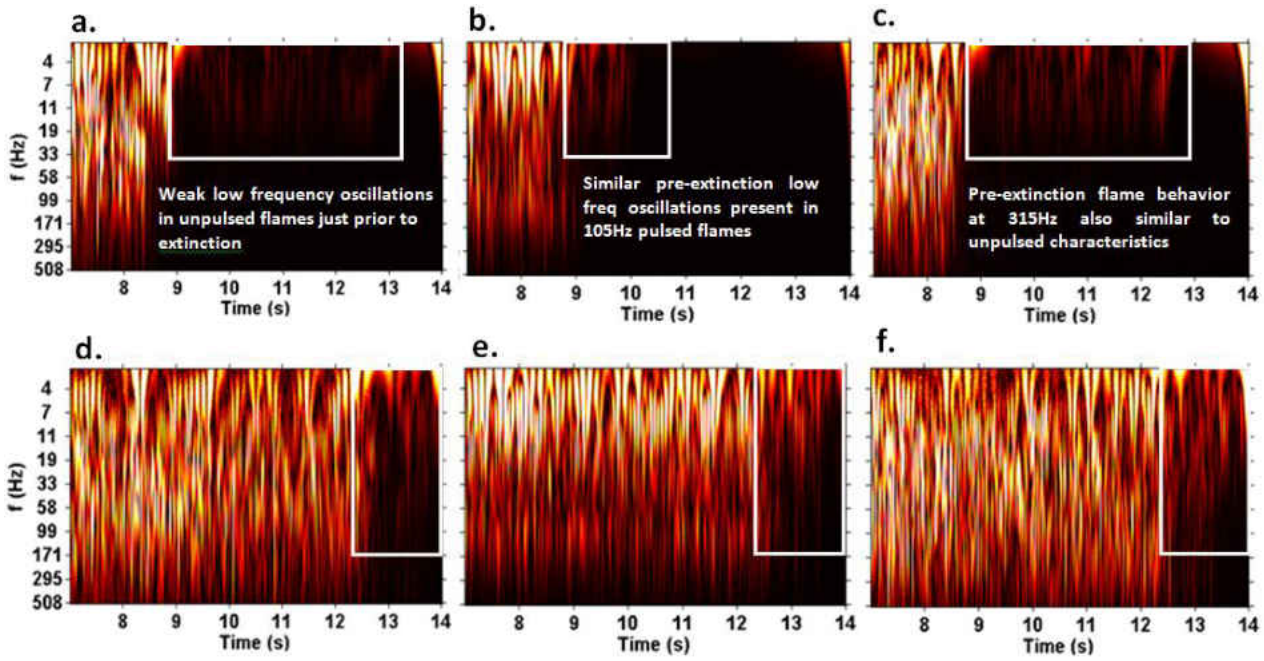

Figure 5.12: Heat Release (CWT) Spectra | Exponential Decay Fuel Flowrate (C3) Flames
a. S009-C3-0Hz (Unpulsed) | b. S009-C3-105Hz | c. S009-C3-315Hz
a. S034-C3-0Hz (Unpulsed) | b. S034-C3-105Hz | c. S034-C3-315Hz

The heat release perturbation ($\hat{q}$) CWT spectra associated with the decaying fuel flow rate (C3) flames are presented in Figure 12. It appears that just prior to extinction, the flame heat release perturbations are dominated by low frequency (3Hz – 20Hz) perturbations. This is more visible in the S034 flames in Figure 12 and also faintly visible in the low swirl (S009) flames even in the unpulsed (f_p = 0Hz) configuration. This suggests that this 3Hz-20Hz heat release perturbation mode is a natural pre-extinction mode of the flame.

The 3Hz-20Hz frequency mode in question is the same at which high intensity heat release rate perturbations were observed with 105Hz acoustic forcing in the CWT spectra of the constant fuel flow C1 and C2 flames of Figure 4.19 as well as the power spectra of Figure 4.4 and 4.5. The

same 3Hz-20Hz heat release perturbations are readily observed very clearly for the 105Hz pulsed flames and all the other flames (albeit less intensely) in Figure 22 just prior to extinction. These observations consequently lend credence to the acoustic forcing approach in the study of the flame response. It appears that the heat release rate modes excited by acoustic forcing are the same as those prevalent in the flame just prior to extinction.

In general, the study of the dynamic fuel flow rate flame yields some important information on the flame dynamics. First is the occurrence of localized flame extinction and reignition resulting in heat release rate perturbations in the 3Hz – 20Hz frequency range. Increasing the swirl intensity and/or the fuel flowrate dampens the occurrence of these localized flame extinction events.

Secondly, it appears the modes excited by acoustic forcing in the highly responsive flame configurations at constant fuel flowrates are the same modes prevalent in the flame just prior to extinction. Essentially, the application of acoustic forcing triggers a pre-extinction mode response in the flame. This pre-extinction mode is characterized by heat release rate oscillations in the 3Hz-20Hz frequency range. Increasing the swirl intensity significantly prolongs the life of the flame beyond the extinction fuel flowrate at low swirl numbers due to the improved stabilization and mixing of the incoming reactants.

CHAPTER 6 ISOTHERMAL FLUID MECHANICS

The characteristics of the burner exit isothermal (no flame) cold flow field is investigated the present chapter. The hot wire anemometry (HWA) and particle image velocity (PIV) techniques are used to study the fluid dynamics associated with the flame response for varying swirl intensities and different acoustic forcing frequencies. The characteristics of the burner exit flow field are first discussed based on the obtained anemometry measurements. The PIV results are then presented for measurements at different pulsing frequencies. The time-averaged fluid dynamics are discussed for relatively rich (C1) and lean (C2) fuel flow rate conditions across all swirl intensities. The effect is acoustic forcing on the topology of the inner recirculation necessary for flame stabilization is examined. This is followed by the phase conditioned analysis of the fluid mechanics associated with acoustic forcing.

6.1 Velocity Measurements with Hot Wire Anemometry

The results to be discussed in this section are based on the hot wire anemometry (HWA) technique for the measurement of velocity. The first results discuss validation attempts to ensure the velocity measurements are sufficiently independent of the anemometer probe orientation for the swirling flows in the current study. The radial distributions of the velocity field at several axial locations are measured to understand the baseline velocity fields associated with the different swirl intensities. The variations of the velocity and the associated intensity of fluctuations are examined for entrainment and swirl intensity effects.

6.1.1 Isolated Velocity Profiles Using Hot Wire Anemometry

In order to quantify the effect of the anemometer probe orientation on the burner exit velocity measurements, the constituent airflows of the burner (axial and tangential) are isolated and their radial distributions measured at the burner exit. Figure 6.1 illustrates the radial velocity profiles and corresponding velocity fluctuation intensities (I_U) at the burner exit for the S034 swirl intensity level. The fluctuation intensity is determined using the I_U relationship of Eq. 3.6.

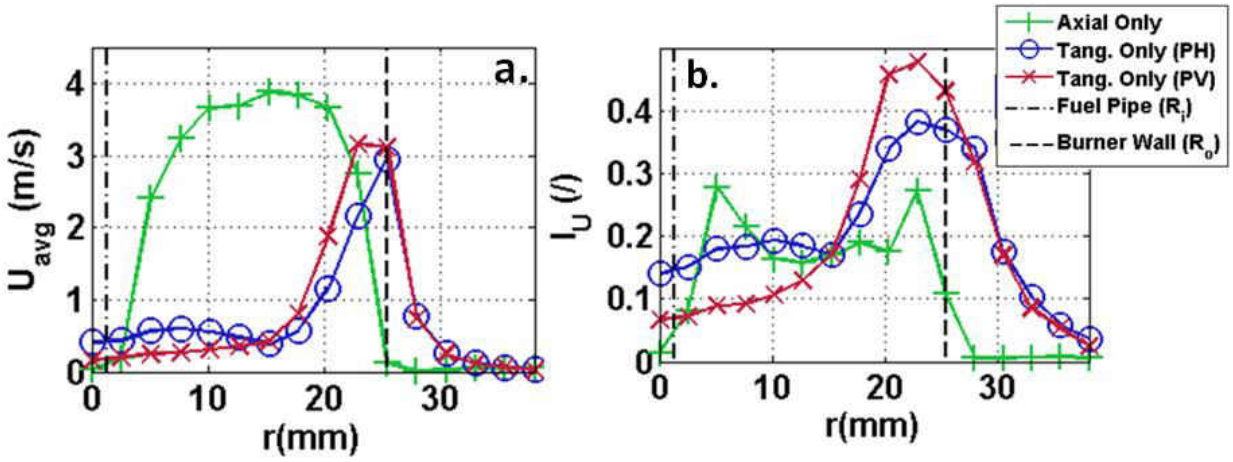

Figure 6.1: Isolated Burner Velocity Profiles for S034
a. Average Velocity – u_{avg}
b. Velocity Fluctuation Intensity – I_U

The radial velocity profiles in Figure 6.1 are acquired with: (1) the co-flow axial air supply on, the CTA probe axis aligned horizontal to the burner axis and tangential air ports turned off; (2) the co-flow axial air supply turned off, the tangential ports turned on and the CTA probe axis parallel to the exit plane of the burner (PH); (3) same conditions as the second case but with the CTA probe axis aligned vertically, parallel to the burner axis (PV).

A parabolic velocity distribution is obtained in Figure 6.1a at the burner exit with only the co-flowing axial air supply. The axial air only fluctuation intensities are highest close to the burner annulus outer wall and fuel pipe as is expected. A decaying velocity profile is obtained for both isolated tangential-only airflow cases. This is as a result of the location of the tangential air supply ports at the outer wall of the axial air annulus. The velocity fluctuation intensities are also highest in the tangential-only case at the burner annulus wall where the tangential air injection ports are located. This is due to ambient air entrainment effects and periodic velocity variations from the injection of swirling air from successive tangential ports.

The fluctuation intensities for the tangential-only cases decay away from the burner co-flow annulus outer wall as the effects of the tangential air injection become limited. This illustrates that most of the velocity fluctuations are produces from the tangential velocity component used to induce swirl. Figure 6.1b also demonstrates that although some dependence on the anemometer probe orientation is observed, consistent general trends are observed for both vertical and horizontal anemometer probe orientation when only the tangential airflow is activated. The isolated air flow results in Figure 6.1 consequently suggest that velocity measurements based on the CTA probe are sufficiently independent of the probe orientation and are adequately representative of fluid phenomena associated with the swirling flow field being investigated.

6.1.2 Cold Flow Field Mapping

Characterizing the burner exit cold flow field was accomplished by traversing the anemometer probe in the radial (*r*) direction at several axial (*Z* = constant) locations above the exit plane of the burner. The flow conditions investigated are as previously established for the various flames configurations presented in Table 1 resulting in maximum burner exit velocities in the range of 3-5 m/s. It should be noted that the mean burner annulus diameter d_m = 0.0254m [1in] was used as the length scale in the calculation of the Reynolds numbers presented in Table 1. The Reynolds number was also utilized to establish flow similarity conditions for the cold flow field mapping measurements carried out with air substituted in the central fuel pipe.

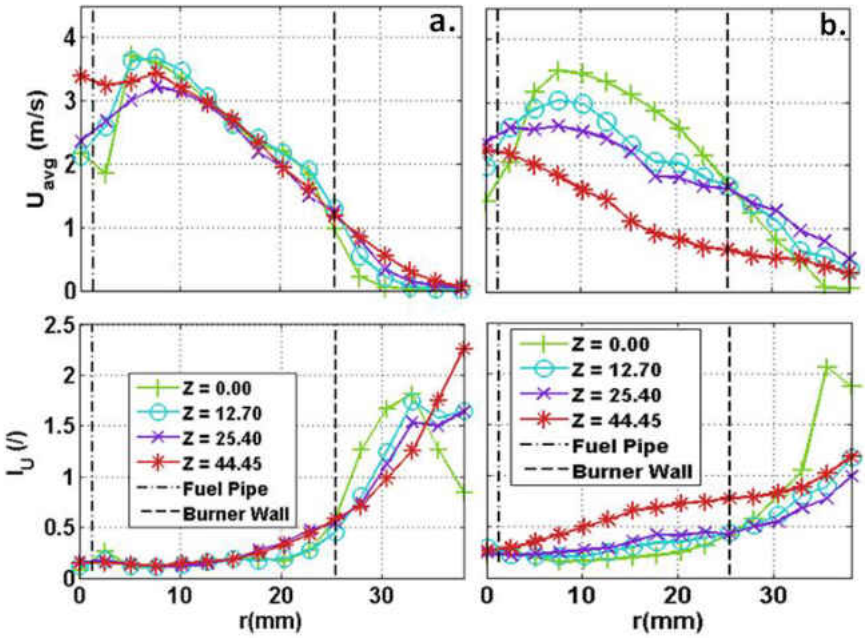

Figure 6.2: Isothermal Velocity Profiles Using Hot Wire Anemometry
a. Low Swirl (S009) | b. High Swirl (S034)

Figure 6.2 shows the cold flow velocity field for the two swirl intensities investigated in the present study. The stratification of the velocity profiles at various z=constant planes begins with peak velocities closest to the exit of the burner (Z=0) decreasing and approaching a flat velocity

profile farther away from the exit plane of the burner. The low swirl (S009) case of Figure 6.2a **Error! Reference source not found.**shows a lack of stratification of the velocity profiles at arious exit planes above the burner. There is minimal decay of the axial momentum leading to the similar velocity distributions as the axial planes in Figure 6.2a. This is characteristic of a jet-like flow field dominated by the axial flow and minimally impacted by the swirl inducing tangential flow for the S009 case.

The high swirl (S034) case in Figure 6.2b is characterized by a decaying velocity profile at succeeding *Z*=constant plane. The maximum velocity at the burner exit (*Z*=0) is comparable to the low swirl (S009) case, but decays relatively quickly by the *Z*=44.45mm plane. The dominance of the higher magnitude axial flow in the low swirl case of Figure 6.2a means it is also characterized by the lower velocity fluctuation intensity of the two swirl levels within the burner annulus ($r < 25.4$mm).

Figure 6.2 shows comparable swirl intensities at the burner exit (Z=0) beyond the burner annulus ($r > 25.4$mm). There are lower intensity fluctuations above the burner exit for the S034 swirl level in this region due to the increased the velocity decay at subsequent *Z*=constant planes. The flow mapping plots demonstrate the significance of the azimuthal velocity (*w*) component which is the primary mechanism for imparting swirl momentum to the axially directed flow. It is the higher azimuthal velocity component that leads to the increased decay in the radial velocity distributions at the higher swirl intensity level in Figure 6.2b.

6.2 Frequency (Time) Averaged Isothermal PIV Analysis

Particle Image Velocimetry studies are carried out for isothermal (no flame) conditions identical to the baseline configurations in Table 1 and Table 2. However, as was the case in the previously discussed hot wire anemometry measurements, air supply is substituted in the central fuel pipe with flow similarity established using the Reynolds numbers. This is in order to isolate the purely fluid dynamics phenomena associated with the observed flame responses. In this section, the time averaged PIV analysis of the various flame configurations are carried out.

6.2.1 PIV Averaging Methodology

For the unpulsed flow configurations the averages are computed as the direct average of 30 images acquired over the sample period. In the case of the forced flow configurations, the averaging procedure to obtain the time average is a follows:

- 30 phase-locked PIV image pairs are obtained trigged to a specific phase angle relative to the acoustic forcing frequency.
- The phase-locked average at this phase angle is obtained using the Davis cross correlation software on the 30 PIV image pairs.
- These phase-locked PIV images are used to compute an ensemble average across several phase angles over the acoustic forcing cycle.
- This resulting ensemble average represents a time (or frequency) average of the PIV measurements at that forcing frequency.
- The procedure is repeated for the various forcing frequencies of interest.

6.2.2 Inner Recirculation Zone (IRZ) Topology

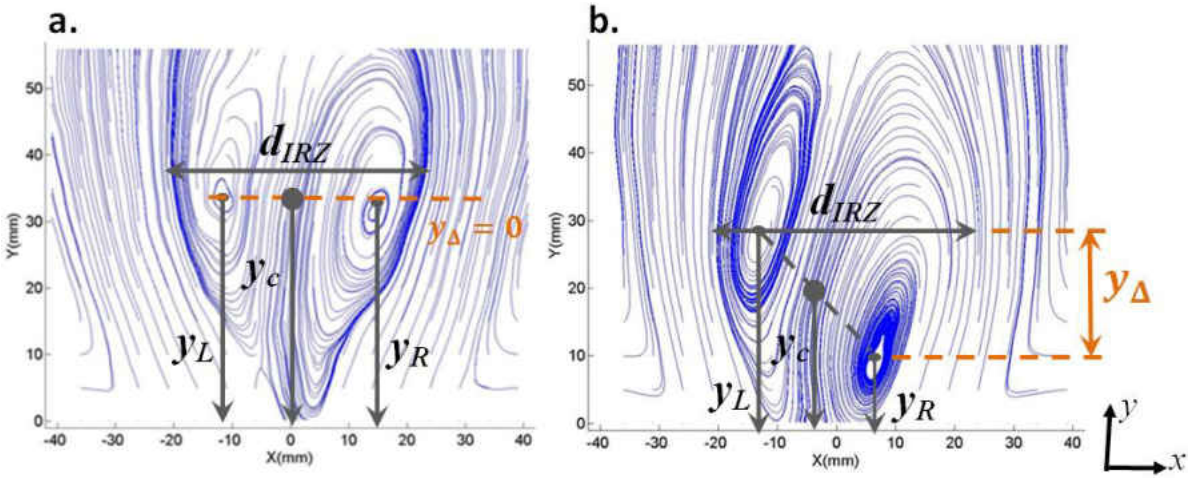

Figure 6.3: Inner Recirculation Zone (IRZ) Nomenclature
a. Symmetric IRZ | b. Non-Symmetric IRZ
Burner Exit Located at y = 0mm

The nomenclature illustrated in Figure 6.3 is used in examining the impact of acoustic forcing on the topology of the inner recirculation zone resulting from the swirling flow configuration. The typically symmetric IRZ is characterized by two mixing vortices. The major dimensions of the IRZ include:

- The diameter of the IRZ designated as d_{IRZ}. The IRZ diameter is determined by the maximum radial extent of the IRZ. The extent of the IRZ is delineated by the first streamlines observed to directly travel from the burner exit to aft of the IRZ.
- The axial coordinates of the left and right mixing vortices in the IRZ are designated as y_L and y_R respectively.

- The axial location of the midpoint of the IRZ designated as y_C. This allows the displacement of the IRZ to be quantified with a single parameter. This parameter is calculated as:

$$y_c = \frac{1}{2}(y_L + y_R) \tag{6. 1}$$

- The degree of symmetry in the IRZ is designated as y_Δ. It is based on the difference between the left a right IRZ vortex locations. Thus non-symmetric IRZs will result in non-zero $y_\Delta$values determined as:

$$y_\Delta = y_L - y_R \tag{6. 2}$$

6.2.3 Unforced Swirling Flow Configurations

The resulting streamlines and time-averaged velocity field at the burner exit from the PIV measurements are illustrated in Figure 6.4. A red reference line is included at the *Z*=20mm location for visualization of the shaded (yellow) inner recirculation zone (IRZ). The effect of lower fuel flow rates (C2) on the flow field is immediately evident in the lower velocity gradient (less dense streamlines) present in the IRZ vortex and is consistent across the two swirl intensity levels. The less dense streamlines in the C2 configurations in Figure 6.4 appear to be due to the lower mixing phenomena from the lower fuel flowrate setting.

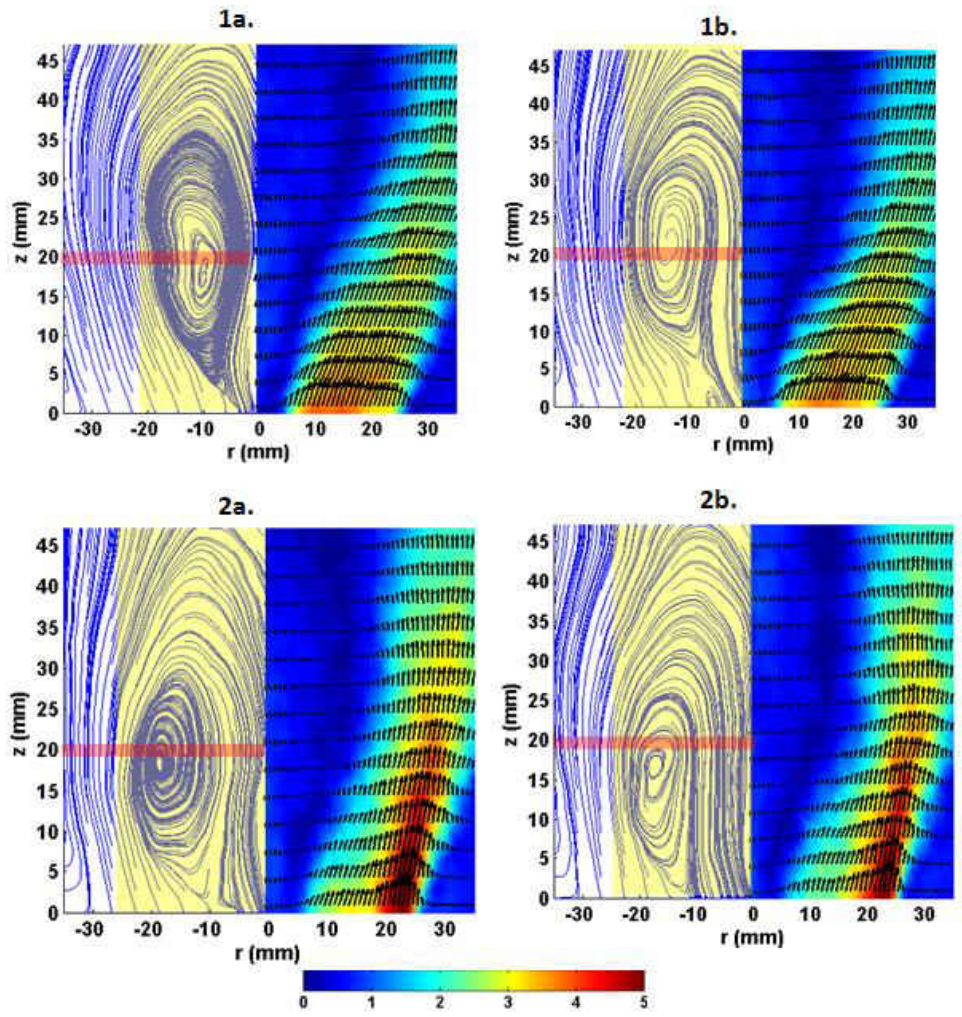

Figure 6.4: Time Averaged Isothermal Velocity Field – Unpulsed (f_p = 0Hz) Mode
1a. S009-C1 | 1b. S009-C2 | 2a. S034-C1 | 2b. S034-C2
Burner Axis: *r* = 0mm | Burner Exit: *z* = 0mm
Fuel Pipe Wall: *r* = 4.6mm | Burner Air Annulus Wall: *r* = 25.4mm

In Figure 6.4, the effect of higher swirl intensity from the S009 to S034 unpulsed case is an increase in the diameter of a more compact IRZ as well and an upstream displacement of the IRZ closer to the burner exit. This appears to be the driving mechanism behind the attachment of the flame (or upstream displacement closer to the burner axis) observed in the unpulsed high swirl flames in Figure 4.6 and Figure 4.7. This demonstrates the utility of the isothermal

fluid mechanics studies at it directly allows the fluid dynamics behind the observed flame response to be readily identified. It then appears that the upstream displacement of the IRZ is related to the inherent higher inertia and centrifugal forces present at the higher swirl level. This would explain the observed increase in the IRZ diameter and the upstream displacement of the IRZ of Figure 6.4.

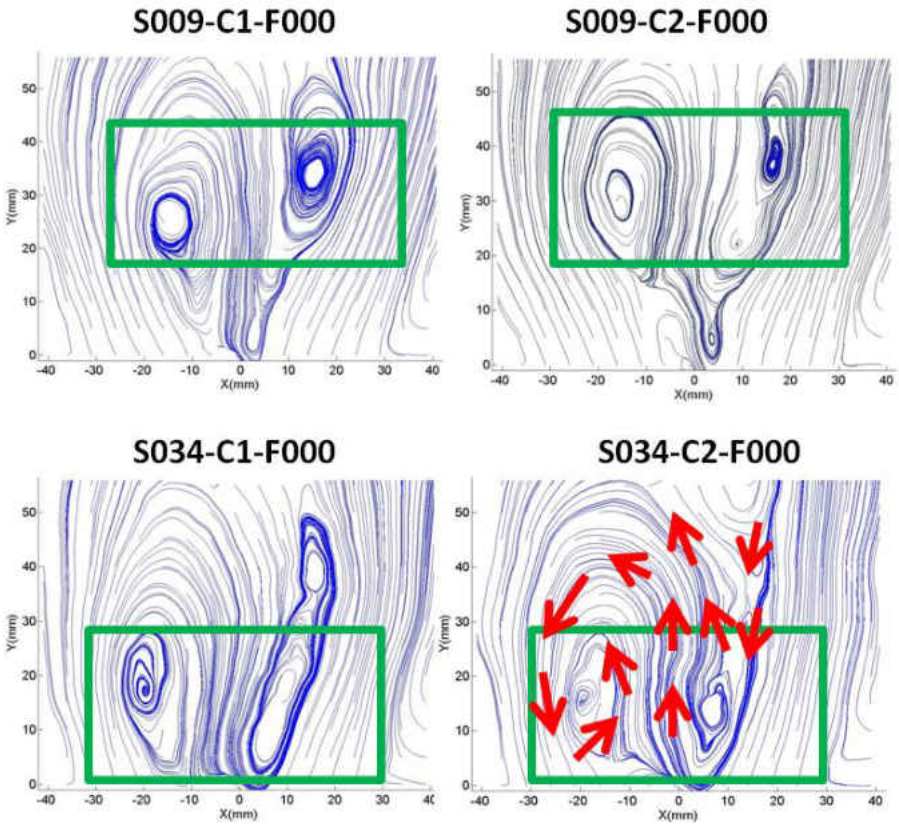

Figure 6.5: Time Averaged Isothermal Streamlines – Unpulsed (f_p = 0Hz) Mode

The full isothermal streamlines for the unforced flow configurations are illustrated in Figure 6.5. The corresponding acoustic pulsing frequency is designated using the FXXX nomenclature with XXX designating the pulsing frequency. The upstream displacement of the IRZ better observed as the IRZ vortices are highlighted in the green boxes. More importantly, Figure 6.5 reveals the

strongly non-symmetric mixing pattern inherent in the unforced swirl flow at all swirl intensities and fuel flowrate settings. The shown red arrows describe the flow pattern in the recirculation zone. It is likely that these asymmetry in the mixing pattern is behind the observed asymmetry in the unpulsed time averaged CH* chemiluminescence images in Figure 4.6.

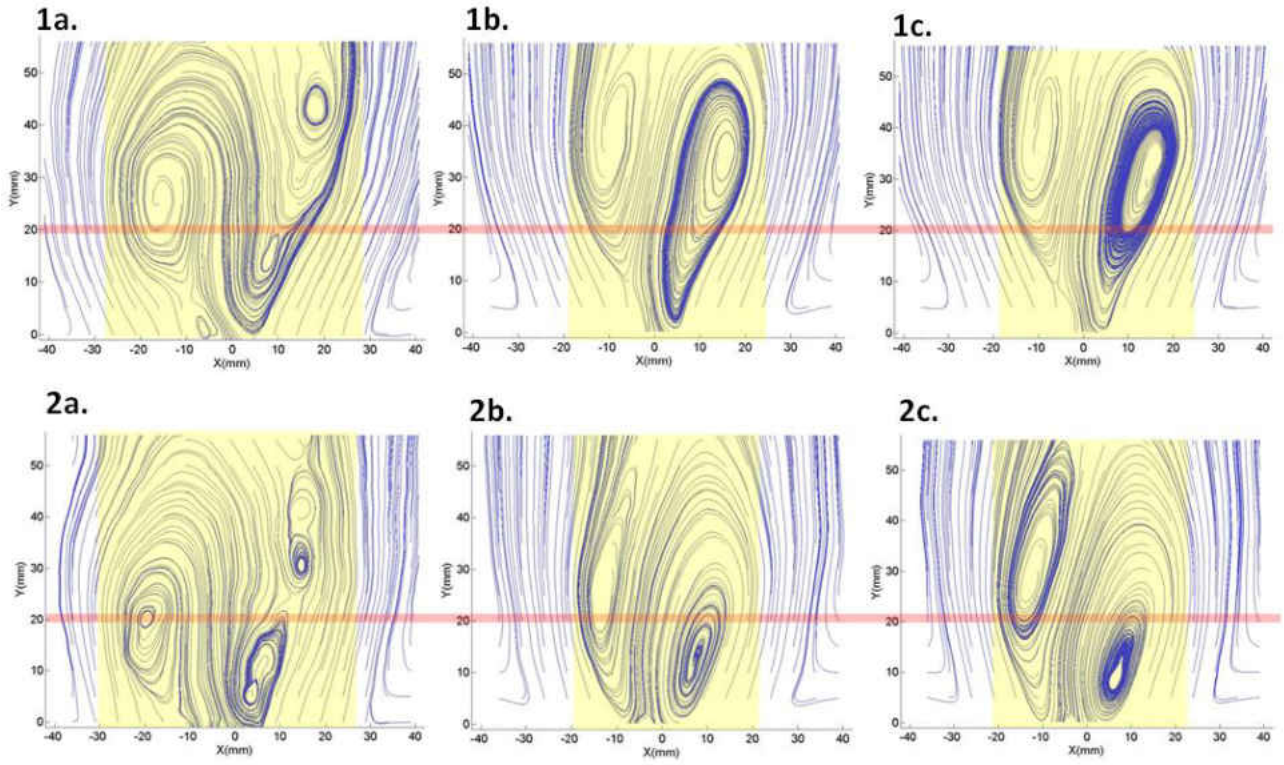

Figure 6.6: Time Averaged Isothermal Streamlines for Acoustically Forced Lean (C2) Flows
1a. S009-C2-0Hz (Unpulsed) | 1b. S009-C2-105Hz | 1c. S009-C2-315Hz
2a. S034-C2-0Hz (Unpulsed) | 2b. S034-C2-105Hz | 2c. S034-C2-315Hz

6.2.4 Forced Swirling Flow Configurations

The physical mechanism behind the observed flame aspect ratio amplification when acoustic forcing is introduced can be examined using the time-averaged isothermal streamlines for forced swirling flows in Figure 6.6. Once again redlines are strictly for the visualization of the

IRZ mixing vortices. Clearly visible is the distinct narrowing of the inner recirculation zone (IRZ) associated with acoustic pulsing that was observed in the flame images of Figure 4.6.

The IRZ in the isothermal flow field undergoes amplification in its aspect ratio which manifests as high aspect ratio flames. The narrowing in the IRZ can be attributed to the transported acoustic (pressure) perturbations in the co-flowing axial air surrounding the IRZ. The flame aspect ratio amplification appears to be a direct consequence of the cold flow IRZ aspect ratio amplification. This would imply that the highest aspect ratio amplification should be observed at the same frequency for both the hot flame conditions as well as isothermal flow field.

The time-averaged isothermal streamlines in Figure 6.6 show that a higher symmetry in the strengths of the mixing vortices (density of streamlines) in the IRZ at the higher S034 swirl intensity. In the low swirl (S009) intensity flow, the time averaged streamlines particularly with acoustic forcing show vortices with varying streamline densities. This is indicates a greater variation in degree of mixing within the vortices that form the IRZ. The resulting higher mixedness gradients (large spatial mixedness variations) in the IRZ would be responsible for increased susceptibility of the lower swirl flames to velocity oscillations from acoustic perturbations.

The effects of swirl intensity, fuel flowrate variations and acoustic forcing on the topology of the IRZ are illustrated in Figure 6.7. All IRZ topology parameters in the figure are normalized using the burner annulus diameter (D_o). The IRZ diameter is essentially analogous to the degree

of aspect ratio amplification in the IRZ due to acoustic forcing. Lower IRZ diameters would represent an IRZ that is squeezed by the acoustic perturbations transported in the co-flowing air surrounding the IRZ. Across all forcing frequencies including the unpulsed mode, the high swirl configurations are characterized by the wider IRZ diameters.

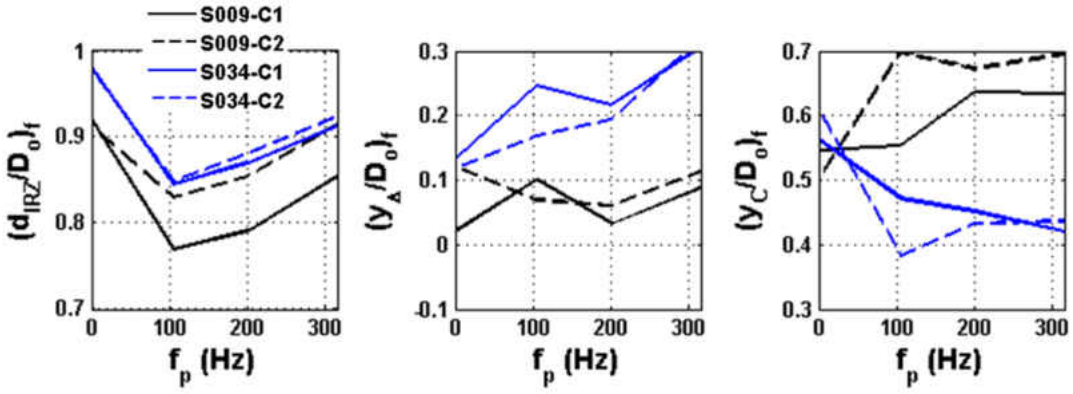

Figure 6.7: Time Averaged Effect of Acoustic Forcing on Inner Recirculation Zone (IRZ)

The largest reduction in the IRZ diameter (d_{IRZ}) occurs with acoustic forcing at a frequency (f_p) of 105Hz. This is the same frequency at which the highest aspect ratios were observed for the various flame configurations in Figure 4.6 through 4.8. The lower swirl flames are observed to exhibit the largest decreases in the IRZ diameters. It is likely that the higher inertia at the higher swirl level increases the resistance to IRZ diameter reduction (i.e. aspect ratio amplification).

The degree of symmetry (y_Δ) is relatively constant in the low swirl (S009) configurations with a small drop at the 105Hz and 201Hz forcing modes in the lean low swirl S009-C2 case. In contrast, the high swirl flow configuration is characterized by increasing asymmetry as the forcing frequency is increased.

The effect of acoustic forcing on the IRZ is observed to differ in Figure 6.7 depending on the swirl intensity. The IRZ center (y_c) in low swirl (S009) cases is displaced *downstream* away from the burner exit plane. The reverse occurs in the high swirl (S034) cases where the IRZ center is displaced *upstream* towards the burner exit. However, the flame CH* chemiluminescence images in Figure 4.6 clearly show that the flames remain attached to the burner axis when acoustic forcing is introduced. This must then imply that the low swirl (S009) flame must be subject to higher strain rates since the IRZ core is translated downstream way from the burner exit even while the flame is remain attached to the fuel pipe.

The increased straining at lower swirl intensities is reflected in the time averaged streamlines in Figure 6.6. The streamlines clearly demonstrate the increased stretching in the axial direction of the IRZ region in the low swirl (S009) cases subjected to acoustic forcing. The higher inertia at higher swirl appears to be the restraining mechanism that prevents the downstream displacement of the IRZ.

The observed higher asymmetry of the IRZ vortices at high swirl is then due to the combined effect of the upstream displacement of the higher inertia IRZ vortices coupled with the narrowing of the IRZ due to the pressure perturbations transported in the co-flowing air. The results clearly demonstrate the strong dependence of the flame response in the mixing phenomena for the non-premixed flame configurations being investigated.

6.3 Time Averaged Acoustic Forcing Effects on Vorticity, Strain Rate and Intensity

The further understand the fluid dynamics associated with the imposed acoustic forcing, the vorticity (ξ), strain rate (ε), fluctuation intensity (I_F) and kinetic energy (KE) are determined based on the velocity field measured using the particle image Velocimetry (PIV) technique. These parameters are dependent of the gradient and fluctuations of the velocity components as follows:

- Vorticity, ξ [s^{-1}]: This is computed using the curl of the velocity field ($\nabla \times \vec{V}$). For the planar 2D velocity field, the dell operator (∇) is defined as:

$$\nabla = \frac{\partial}{\partial x}\hat{\imath} + \frac{\partial}{\partial y}\hat{\jmath} \tag{6.3}$$

  Based on the burner exit coordinate systems illustrated in Figure 6.3, $\hat{\imath}$ and $\hat{\jmath}$ represent the unit vectors in the x (radial) and y (axial) directions respectively. The velocity field is defined with the u and v components in the x and y directions respectively resulting in the vector form:

$$\vec{\nabla} = u\hat{\imath} + v\hat{\jmath} \tag{6.4}$$

  Thus based on the measure velocity field, the vorticity (x) is computed as:

$$\xi = \frac{\partial v}{\partial x} - \frac{\partial u}{\partial y} \tag{6.5}$$

- Strain Rate, ε [s^{-1}]: The strain rate is also computed using the velocity gradients as:

$$\varepsilon = \frac{\partial v}{\partial x} + \frac{\partial u}{\partial y} \tag{6.6}$$

- The 2D Velocity Fluctuation Intensity, I_F [/]: is analogous to the formulation in Eq. 3.6 but takes into account the two dimensional nature of the flow field. It is computed as:

$$I_F = \frac{\sqrt{\overline{u'^2} + \overline{v'^2}}}{\sqrt{\mathrm{U}^2 + \mathrm{V}^2}} \tag{6.7}$$

  U and V refer to the time averaged velocity components in the x and y directions respectively.

- The Kinetic Energy, KE [m^2s^{-2}]: is the energy per unit mass and is analogous to the well known turbulent kinetic energy term in fully turbulent flows. It is a quantification of the mean normal stresses in the flow and computed as:

$$KE = \overline{u'^2} + \overline{v'^2} \tag{6.8}$$

The vorticity, strain rate and fluctuation intensity fields at each time instant are used in the averaging procedure detailed in section 6.2.2 to obtain either the frequency (time) averaged or phase conditioned results. The desired analysis also drives the averaging method used to compute the kinetic energy term.

The instantaneous velocity, vorticity(x) and strain rate (e) at a selected time instant are presented for the baseline cases in Figure 6.8. The streamlines also included to illustrate the intense vorticity (ξ) and strain rates (ε) that characterize the outer shear layer as a result of ambient air entrainment. The velocity components, vorticity and strain rates are normalized using the diameter of the burner annulus (D_o) and the bulk velocity (U_o) of each follow configuration.

The bulk velocity is computed using the nominal axial ($U_{a,a}$), tangential ($U_{a,t}$) and fuel (U_{fb}) velocities calculated from the respective mass flow rates in Table 1. An area averaging procedure is then used to obtain the bulk velocity (U_o) as follows:

$$U_o = \frac{A_{a,a}U_{a,a} + A_{a,t}U_{a,t} + A_f U_{fb}}{A_{a,a} + A_{a,t} + A_f} \tag{6.9}$$

Table 4: Nominal and Flow Bulk Velocities

Case	$U_{a,a}$ (m/s)	$U_{a,t}$ (m/s)	U_f (m/s)	U_o (m/s)
S009-C1	1.46	7.23	1.09	1.76
S009-C2	1.46	7.23	0.39	1.74
S034-C1	1.42	12.49	1.09	2.02
S034-C2	1.42	12.49	0.39	1.99

The cross-sectional area of the burner co-flow air annulus, total cross-section area across all tangential ports and the fuel pipe cross-sectional areas are respectively denoted as $A_{a,a}$, $A_{a,t}$ and A_f in Eq. 6.9. The obtained nominal velocities as well as the computed bulk velocity for each flow configuration are detailed in Table 4.

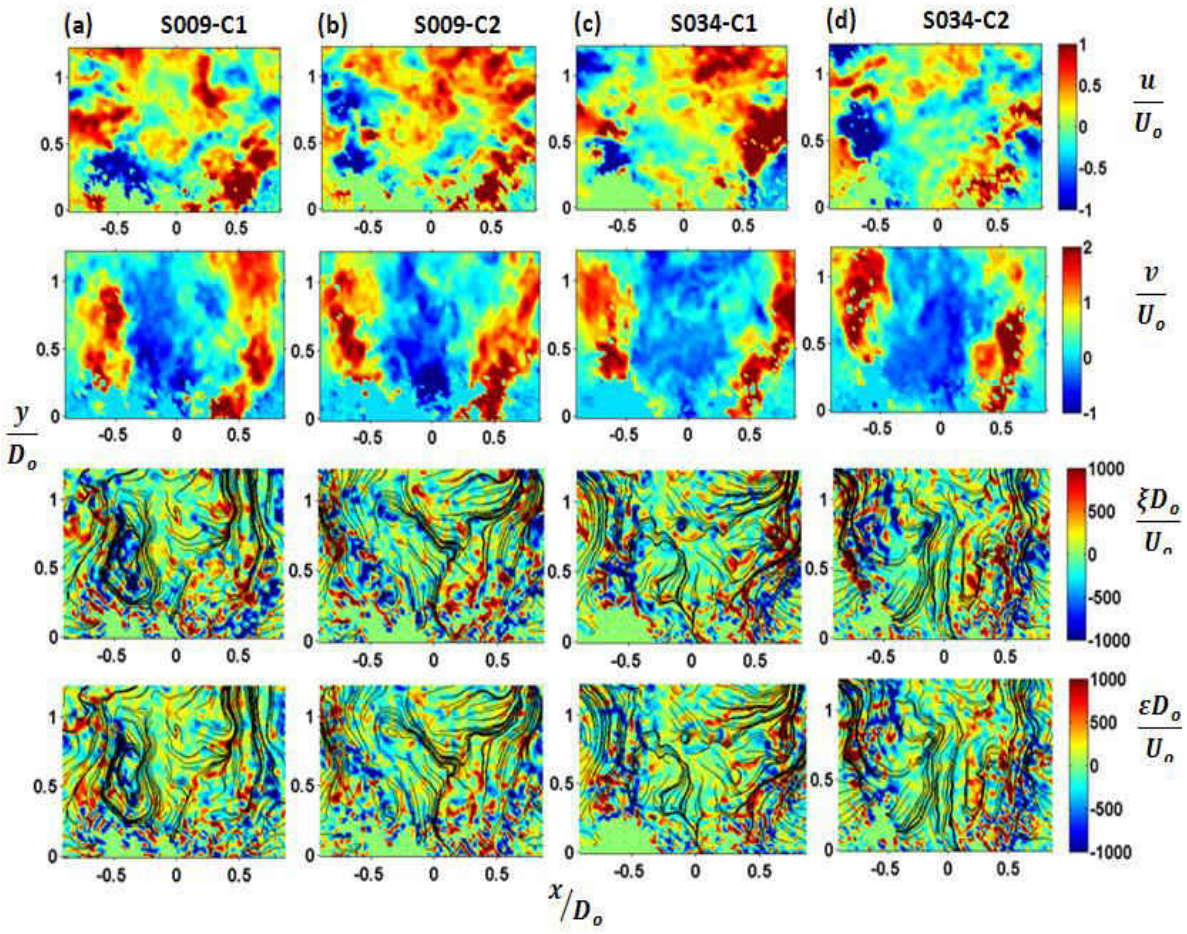

Figure 6.8: Instantaneous Velocity, Vorticity and Strain Rate – Unpulsed (f_p = 0Hz) Mode

The highest strain rates and vorticities in the instantaneous results in Figure 6.8 are located in the outer shear layer where entrainment of ambient air occurs. There also appears to be a fundamental asymmetry associated with the flow field particularly directly above the burner exit. This is in agreement with the time averaged streamlines for the unforced cases in Figure 6.5 and Figure 6.6 where a naturally asymmetric mixing pattern was observed in the inner recirculation zones of unforced flow configurations. The instantaneous results in Figure 6.8 suggest that an averaging procedure is necessary for the examination of the fluid dynamics in the various flow configurations.

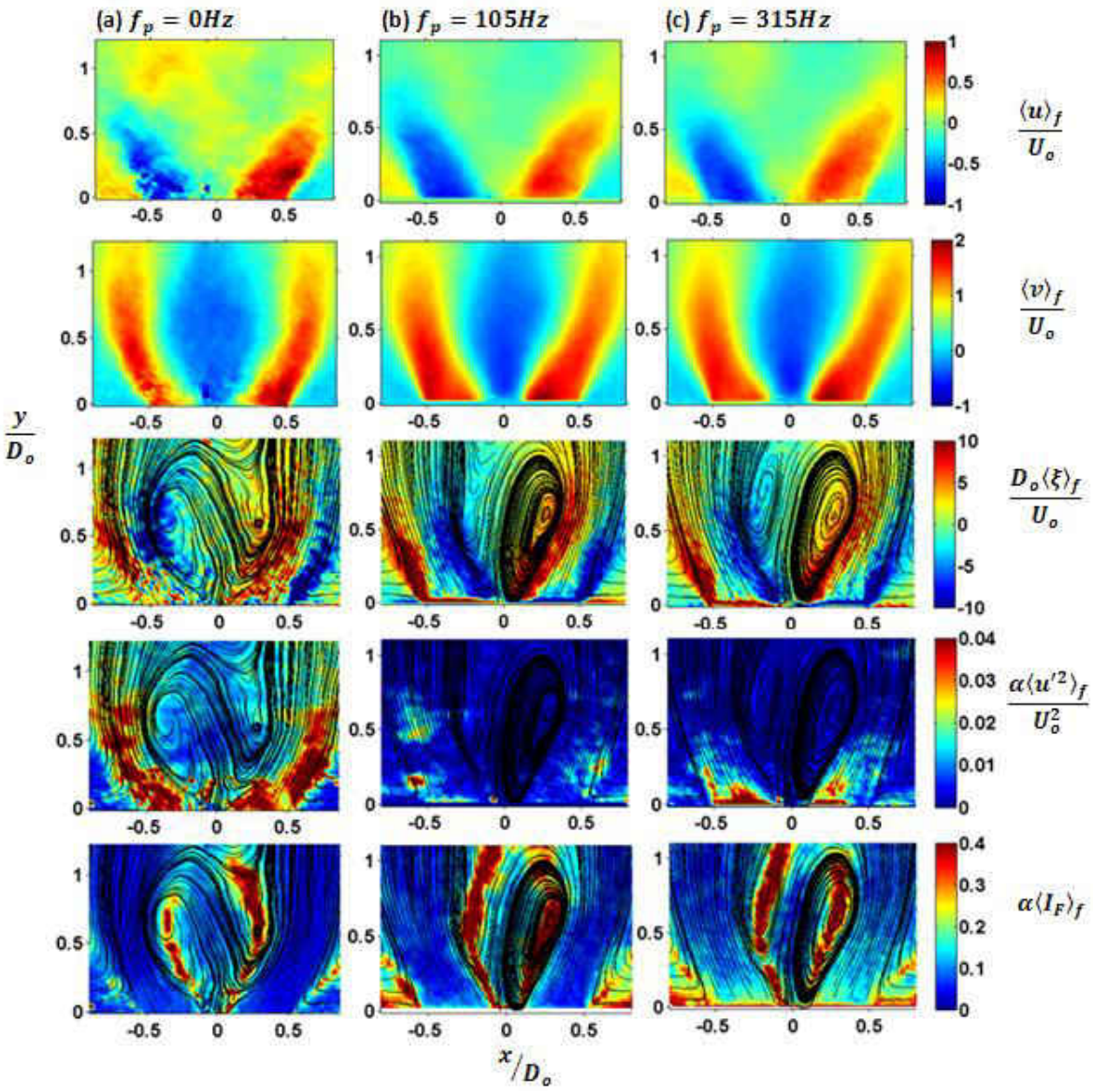

Figure 6.9: Frequency (Time) Averaged Isothermal Fluid Response – S009-C1
a. Unpulsed (α = 0.1) | b. 105Hz Forcing (α = 1) | c. 315Hz Forcing (α = 1)

The time averaged results from the PIV calculations are presented in Figure 6.9 for the S009-C1 flow configuration. The *f* subscript in the nomenclature of figure 6.9 denotes that the results are frequency (time) averaged results. The improvement in the laminarity of the velocity field when acoustic forcing is applied is clearly evident. The negative v velocity component clearly delineates the IRZ at the core of the surround co-flowing air. The IRZ is better defined in the

pulsed flow configurations due to the laminarization of the velocity field with acoustic forcing. The vorticity field illustrates the high vorticity present in not just the outer shear layer (OSL) where ambient entrainment occurs, but also an inner shear layer (ISL) due to the interaction between the IRZ mixing vortices and the co-flowing fluid being.

The decrease in the kinetic energy, $\left(\frac{\alpha\langle u'^2\rangle_f}{U_o^2}\right)$ in the co-flowing air due to the imposed acoustic perturbations is readily evident. The scaling factor (α) is used to ensure the data is fitted magnitude-wise to the common color map used for the kinetic energy plots. Taking the scaling factor into account in Figure 6.9, the kinetic energy in the unpulsed case is an order of magnitude higher in the coflowing air between the inner and outer shear layers. The kinetic energy is subsequently reduced in the acoustically forced cases. However, there appears to be an asymmetric period shedding of high energy regions (eddies) at the 105Hz forcing mode. This periodic shedding is absent at the 315Hz forcing mode where minimal flame responses were obtained. The periodic shedding of eddies is not observed either at the unpulsed flow configuration.

The fluctuation intensity (I_F) field plots in Figure 6.9 also illustrate an order or magnitude decrease due to the imposed acoustic forcing. However, it is clearly evident that the locations of maximum velocity fluctuation intensity are the core of the IRZ mixing vortices, as well as the entrainment region between the co-flowing and ambient air. Hence the mixing phenomena occurring the IRZ and entrainments layer are characterized by high intensity velocity fluctuations.

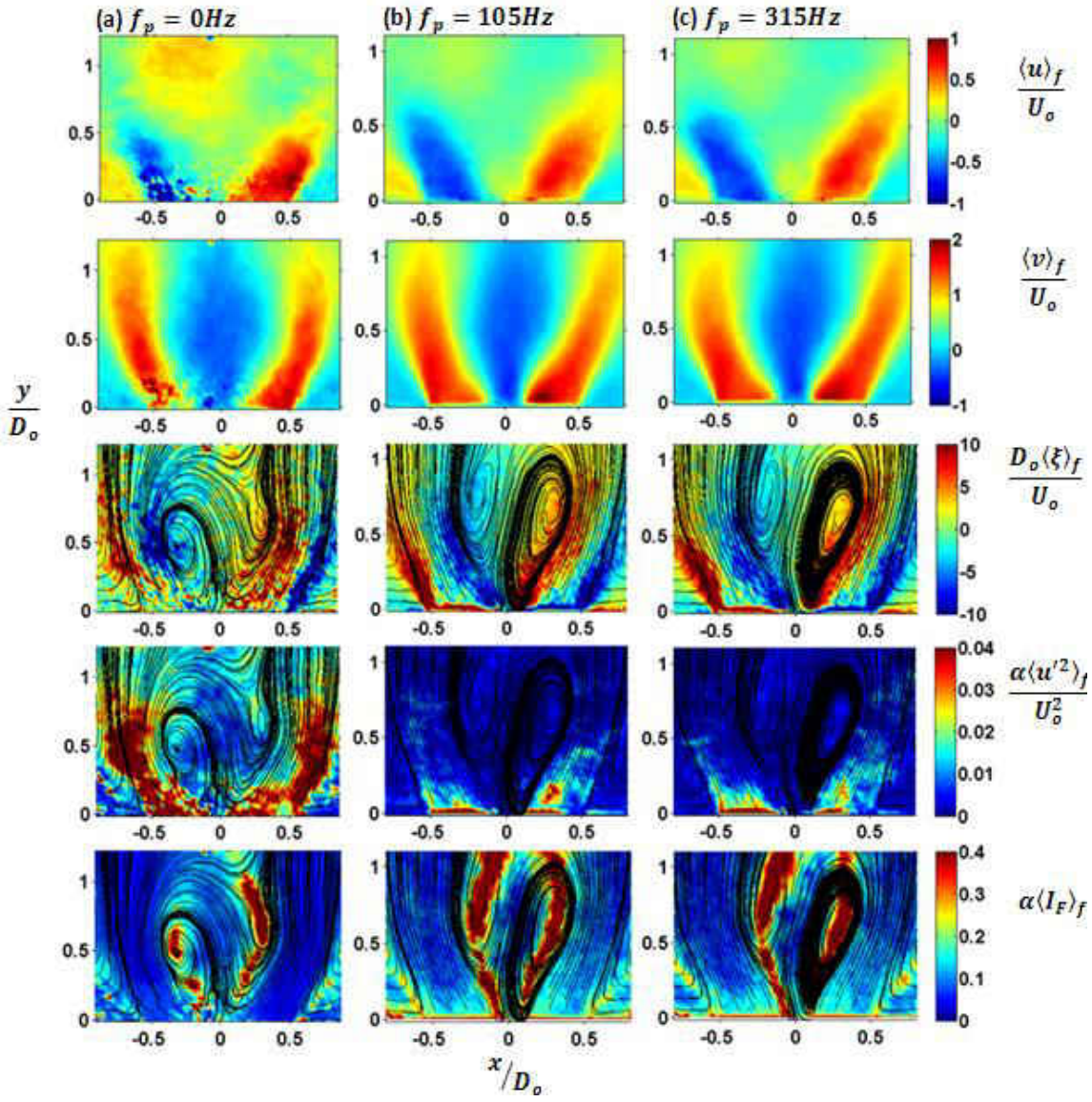

Figure 6.10: Frequency (Time) Averaged Isothermal Fluid Response – S009-C2
a. Unpulsed (α = 0.1) | b. 105Hz Forcing (α = 1) | c. 315Hz Forcing (α = 1)

The results for the low swirl and lean S009-C2 flow configuration is illustrated in Figure 6.10. The general results as somewhat similar to the previous S009-C1 case in Figure 6.9. As in the S009-C1 case, introduction of acoustic forcing appears to better concentrate the high vorticity regions into the ISL and OSL along with one critical difference. There is an absence of the period shedding of high energy regions (eddies) in the kinetic energy $\left(\frac{\alpha \langle u'^2 \rangle_f}{U_o^2}\right)$ field in the Figure 6.10

as was observed for the high fuel flowrate S009-C1 case in Figure 6.9. The absence of periodic shedding of eddies is also accompanied by a generally lower intensity of the velocity fluctuations (I_F) in the entrainment region between the co-flowing and ambient air when acoustic forcing is introduced.

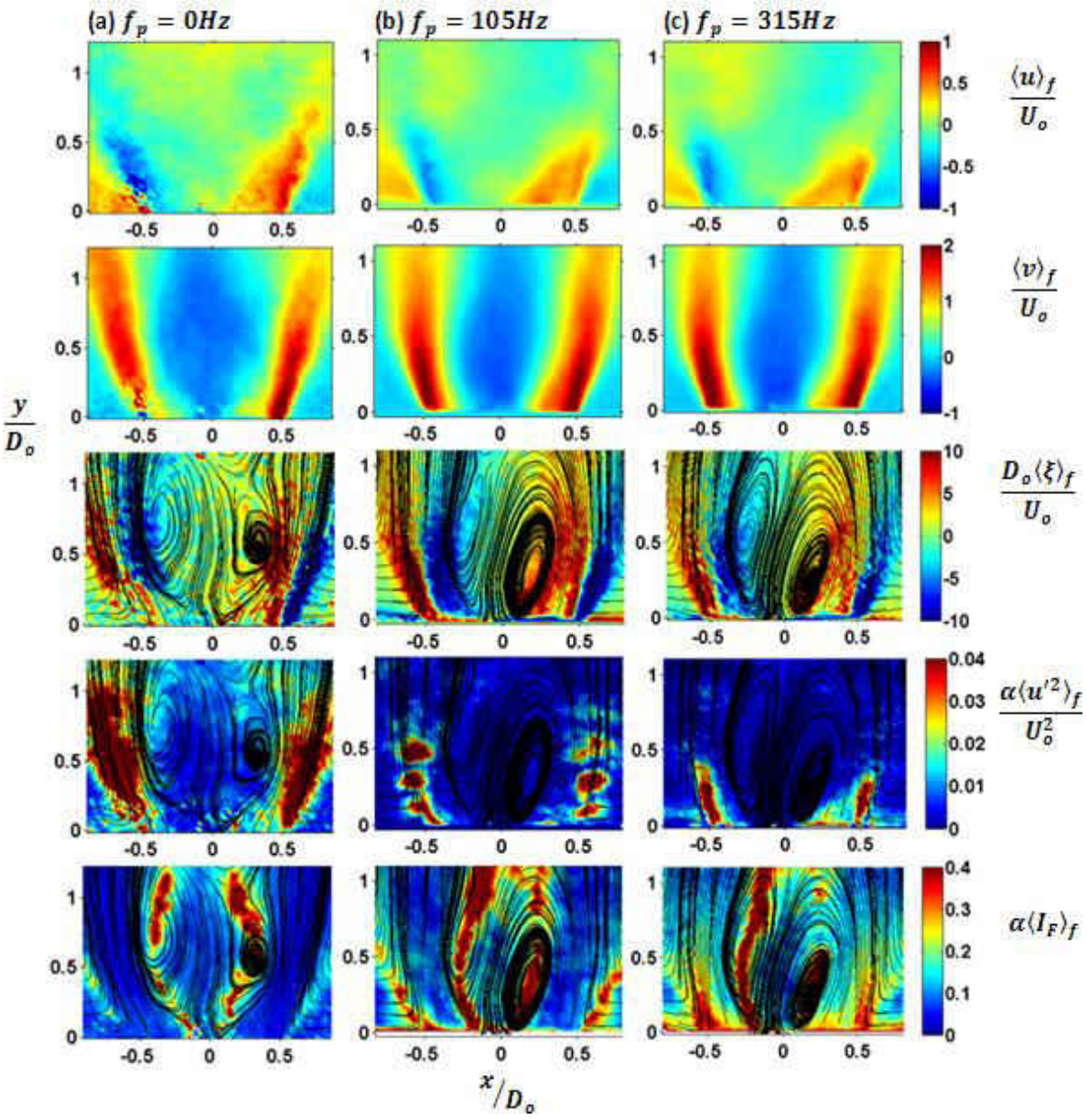

Figure 6.11: Frequency (Time) Averaged Isothermal Fluid Response – S034-C1
a. Unpulsed (α = 0.1) | b. 105Hz Forcing (α = 1) | c. 315Hz Forcing (α = 1)

The PIV results for the S034-C1 flow configuration are presented in Figure 6.11. The larger IRZ diameters previously discussed in Figure 6.7 are readily observed across all the forcing modes. A thinner region of high coflow velocity components (*u* and *v*) in comparison to the low swirl cases in Figure 6.9 and 6.10 is also visible in the velocity fields of Figure 6.11. This is a direct consequence of the higher inertia present at high swirl intensities. The axial velocity (*v*) is also higher than the previously discussed low swirl (S009) cases. This is expected due to the higher tangential air velocities utilized to generate the high swirl intensity.

The vorticity $\left(\frac{D_o\langle\xi\rangle_f}{U_o}\right)$ field plots in Figure 6.11 exhibit some similarities to the low swirl cases including the concentration of the high vorticity regions into the inner shear layer (ISL) and outer shear layer (OSL). In addition, the regions of high vorticity in the OSL and ISL extend farther downstream in the high swirl intensity case of Figure 6.11. There also appear to the strong interaction between the inner and outer shear layers particularly at the 105Hz forcing mode where the high vorticity regions in the ISL and OSL completely span the co-flowing air region surrounding the IRZ. This would suggest significant energy interaction between the OSL, ISL and the IRZ vortices in the S034-C1 case of Figure 6.11.

Indeed when we examine the $\left(\frac{\alpha\langle u'^2\rangle_f}{U_o^2}\right)$ field in Figure 6.11 at the 105Hz acoustic forcing mode, there is a significant enhancement of the periodic shedding of the regions of high kinetic energy in comparison with the low swirl S009-C1 case of Figure 6.1. These high energy eddies are particularly well defined at the 105Hz forcing mode and hardly observable at the 315Hz mode.

In addition, a higher velocity fluctuation intensity (I_F) is observed in the outer shear layer due to entrainment at the 105Hz mode. This firmly establishes the link between entrainment and periodic shedding of high energy eddy at in strongly responsive flow configurations. Similar shedding phenomena has been reported by Kulsheimer et al. [44] as a precondition for the initiation of a significant premixed flame response under acoustic forcing.

It is necessary to note that the analogous S034-C1 flame configuration is characterized by a positive Flame response index in Figure 4.9 i.e., minimally responsive. Thus the observed vortex shedding is not an automatic indicator of a strong flame response. This is because the velocity oscillations $\langle u' \rangle$ induced by the shedding of high energy vortices and heat release rate perturbations may not be in phase. In fact, Figure 4.21 shows the S034-C1 case with a velocity $\langle u' \rangle$ to heat release rate $\langle q' \rangle$ perturbation phase lag of 135^{o} indicating somewhat out of phase oscillations.

In the results for the S034-C2 flow configurations in Figure 6.12, the velocity fields are similar to those of the S034-C1 case in figure 6.11. The concentrations of high vorticity in the OSL and ISL are as previously observed including the order of magnitude reduction in the kinetic energy in the co-flowing air between the ISL and OSL. At the 105Hz forcing mode, there is a similar periodic shedding of high energy eddies which appear to be larger in area although less well defined as those of the S034-C1 case. Also observed is the expected increase in fluctuation intensity (I_F) in the entrainment layer which is maximum at the 105Hz forcing mode among the forced flow configurations in the S034-C2 case of Figure 6.12.

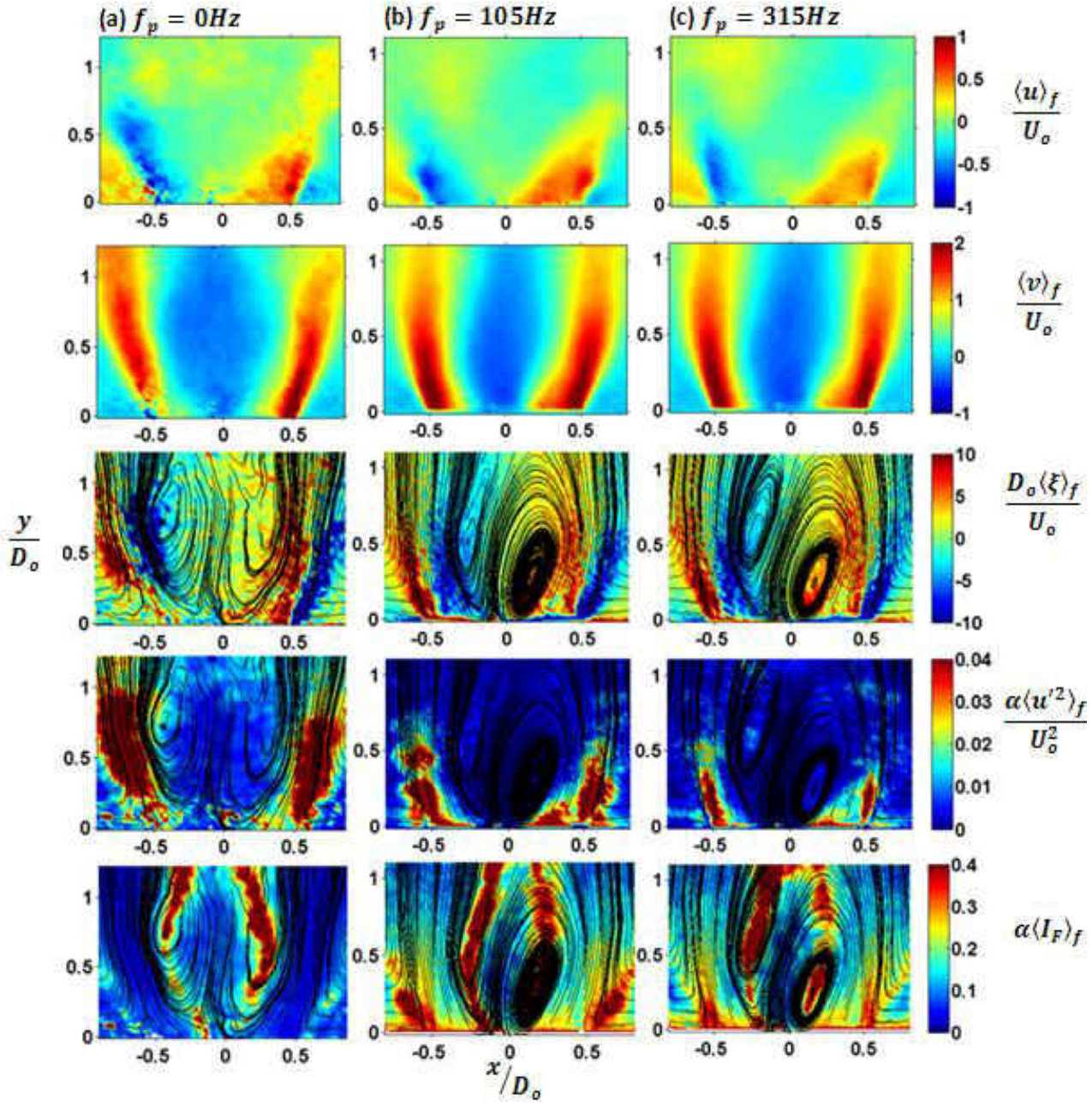

Figure 6.12: Frequency (Time) Averaged Isothermal Fluid Response – S034-C2
a. Unpulsed (α = 0.1) | b. 105Hz Forcing (α = 1) | c. 315Hz Forcing (α = 1)

6.4 Phase Conditioned Isothermal PIV Analysis

The previous discussion focused on a frequency (time) averaged analysis of the fluid mechanics associated with acoustic forcing. In this section, the phase conditioned analysis of the fluid dynamics is carried out. Isothermal flow streamlines associated with the acoustically pulsed flow configurations are illustrated in Figure 6.13 for the 105Hz forcing mode. These streamlines are averaged across specific phases relative to the pulsing signal based on the averaging procedure set forth in section 6.2.1.

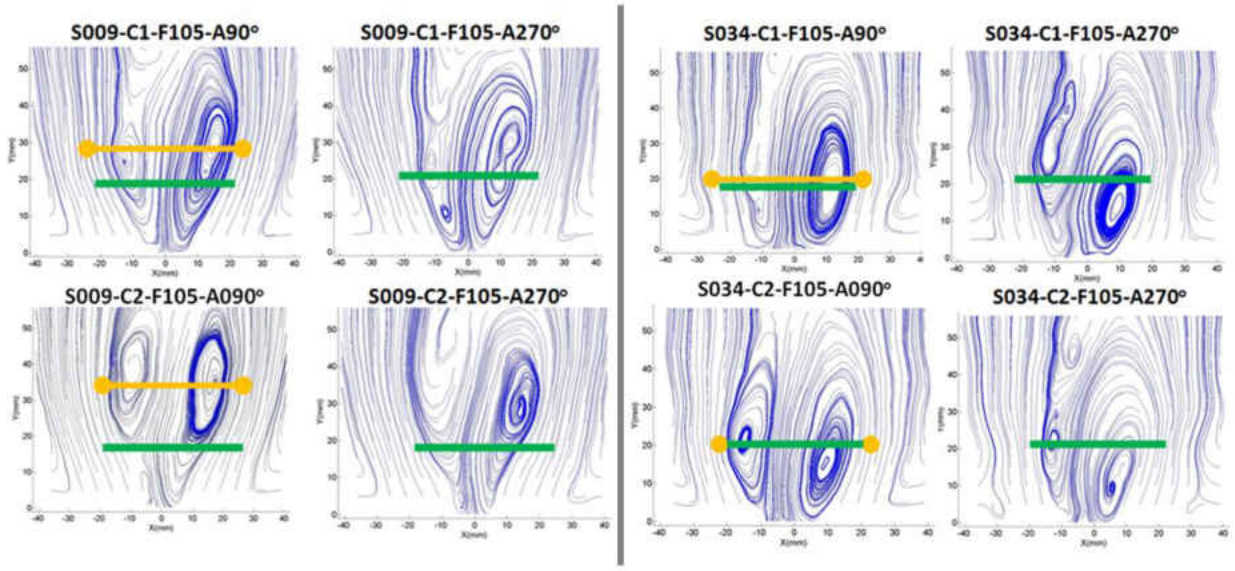

Figure 6.13: Phase Conditioned Isothermal Streamlines – 105Hz Forcing Mode
Left: Low Swirl (S009) | Right: High Swirl (S039)

Immediately visible is the distinct narrowing of the inner recirculation zone (IRZ) associated with acoustic pulsing as observed in the previous time averaged results. The transport of the acoustic (pressure) perturbations in the co-flowing axial air surrounding the IRZ leads to the observed narrowing in the IRZ width.

In Figure 6.13, a green reference line is provided for visualization purposes at the y = 20mm location. In addition, the yellow dumbbell shaped line highlights the vertical location of the cores of the mixing vortices in the IRZ. The phase locked streamlines for the S009-C1 and the S034-C1 cases are on the left and right sides of Figure 6.13 respectively. The cases are identified using the S009-C1-FXXX-AYYY nomenclature. XXX represents the acoustic forcing frequency and YYY represents the phase angle to which the images are locked.

The phase-locked acoustically forced streamlines for the lower swirl (S009) case in Figure 6.13 clearly illustrates the vertical displacement of the IRZ core is strongly linked to the phase of the acoustic perturbation signal. Using the S009-C1 case in Figure 6.13 as an example, the IRZ vortices are located farther downstream at the 90^{o} peak of the forcing signal, than at the 270^{o} acoustic forcing phase. Streamlines for only two phase angles are provided for each case in shown in Figure 6.13 but it is observed that the maximum vertical displacement of the IRZ vortices occurs at the peak (90^{o} phase angle) of the acoustic forcing signal. At the trough (270^{o}) of the acoustic pulsing signal, the IRZ vortices are observed to be at or below the green reference line in Figure 11.

There also appears to be some dependence on the fuel flowrate setting. At the 90^{o} phase angle, the S009-C2 IRZ vortices are displaced farther downstream from the burner exit compared to the S009-C1 case which is at the same swirl level. This is the result of the lower inertial resistance to vertical displacement inherent in the weakly mixed vortices at the lower fuel

setting in the S009-C2 case. Figure 6.13 illustrates that for higher fuel flow configurations (C1), the increased mixing appears to yield IRZ vortices with an increased resistance to phase dependent displacement by the acoustic perturbations.

Also clearly demonstrated in Figure 6.13 is the decreased vertical displacement of the IRZ vortices at the peak and trough (90^o and 270^o phase angles) of the acoustic pulsing signal. The increased inertia introduced by the higher swirl intensity appears to improve the resistance of the IRZ to vertical displacement perturbations by the acoustic pulsing signal. For the higher swirl (S034) case, it does appear that rather than a symmetric displacement if the IRZ vortices, the acoustic forcing results in a higher asymmetry in the IRZ which would be symptomatic of a toroidal IRZ vortical structure gyrating about its axis.

The phase conditioned velocity perturbations $\frac{\langle u \rangle_\phi}{U_o}$ and $\frac{\langle v \rangle_\phi}{U_o}$ as well as the strain, kinetic energy and fluctuation intensity are illustrated in Figure 6.14 through Figure 6.17 for the lean fuel flowrate (C2) cases. This is motivated by the previous observation that the most highly responsive flames were configurations with lean (C2) fuel flowrates. Figure 6.14 illustrates the results for the S009-C2 case with 105Hz acoustic forcing. Phase averages are provided at phase angles of 0, 90 and 270 degrees. As was observed in the previous time averaged results, the inner recirculation zone is well defined by the region of negative axial velocity $\left(\frac{\langle v \rangle_\phi}{U_o}\right)$. The regions of high vorticity $\left(\frac{\boldsymbol{D_o \langle \xi \rangle_\phi}}{\boldsymbol{U_o}}\right)$ are once again concentrated in the inner shear layer (ISL) and outer shear layer (OSL). There is no observable phase dependence in the S009-C2 flame

subjected to acoustic forcing. There is also no significant period shedding of high energy eddies for the S009-C2-105Hz mode. This is an important observation about the nature of the flame response at this forcing mode / swirl intensity configuration which is characterized by one of the highest flame response indices (highly responsive flame) in the current study.

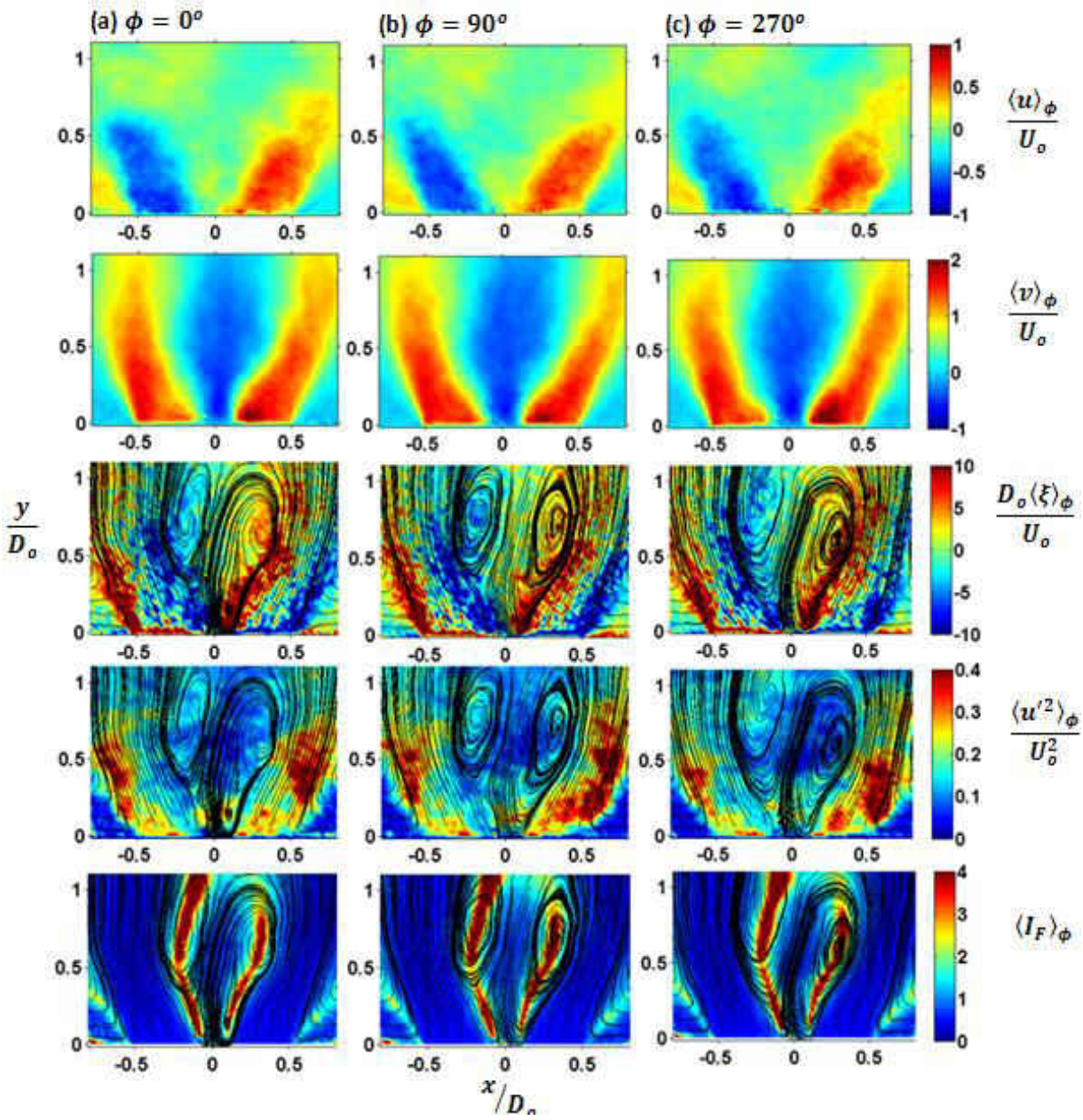

Figure 6.14: Phase Conditioned Fluid Dynamics – S009-C2-105Hz
a. $\phi = 0^o$ | b. $\phi = 90^o$ | c. $\phi = 270^o$

In the phase conditioned fluid dynamics results in Figure 6.15 there is once again no observable period shedding of high energy vorticity shedding for the S009-C2 flame when subjected to 315Hz forcing. This is somewhat expected du for this forcing frequency since it is higher than the threshold of 201Hz below which high responsive flame configurations were observed.

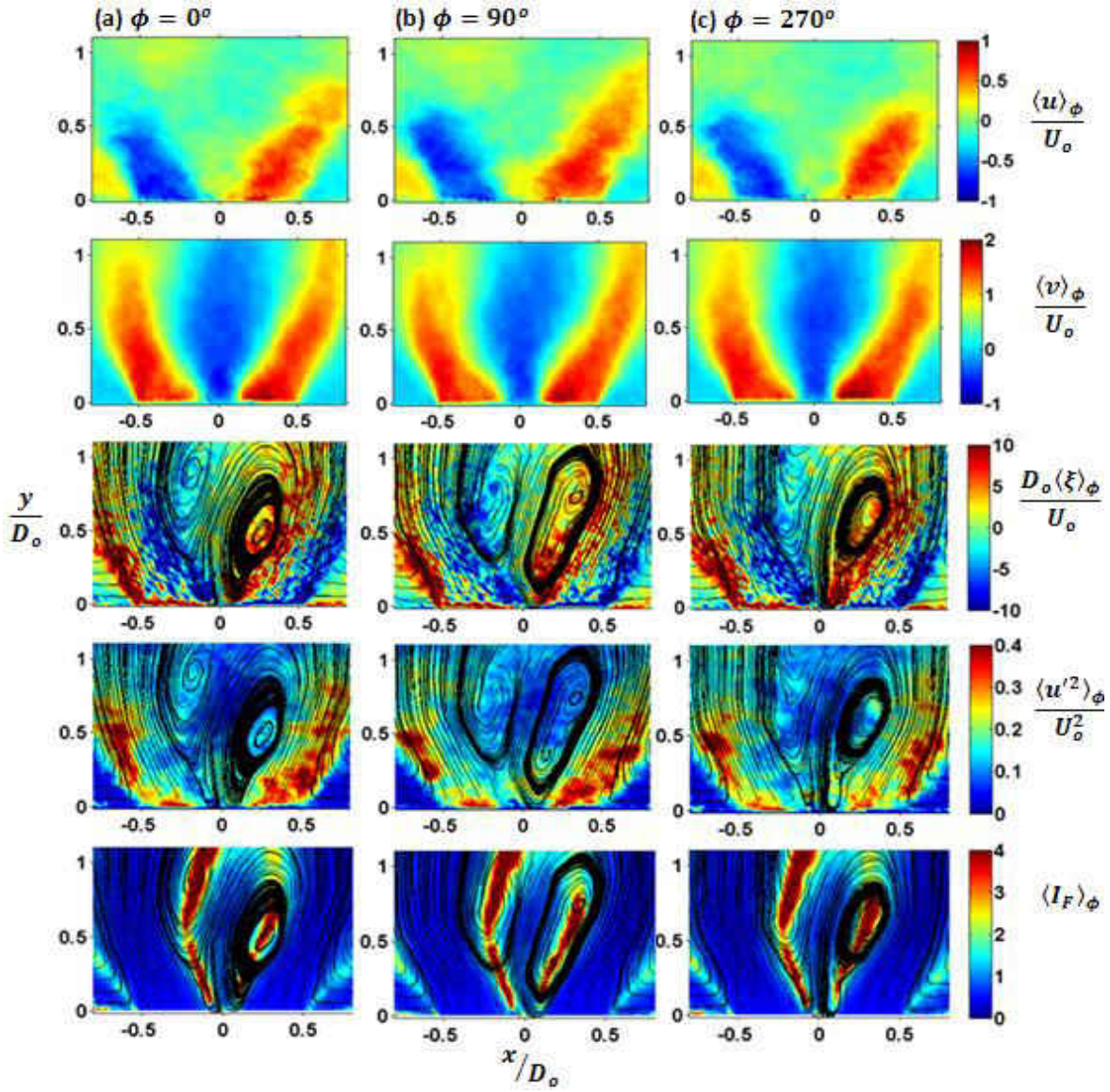

Figure 6.15: Phase Conditioned Fluid Dynamics – S009-C2-315Hz
a. ϕ = 0° | b. ϕ = 90° | c. ϕ = 270°

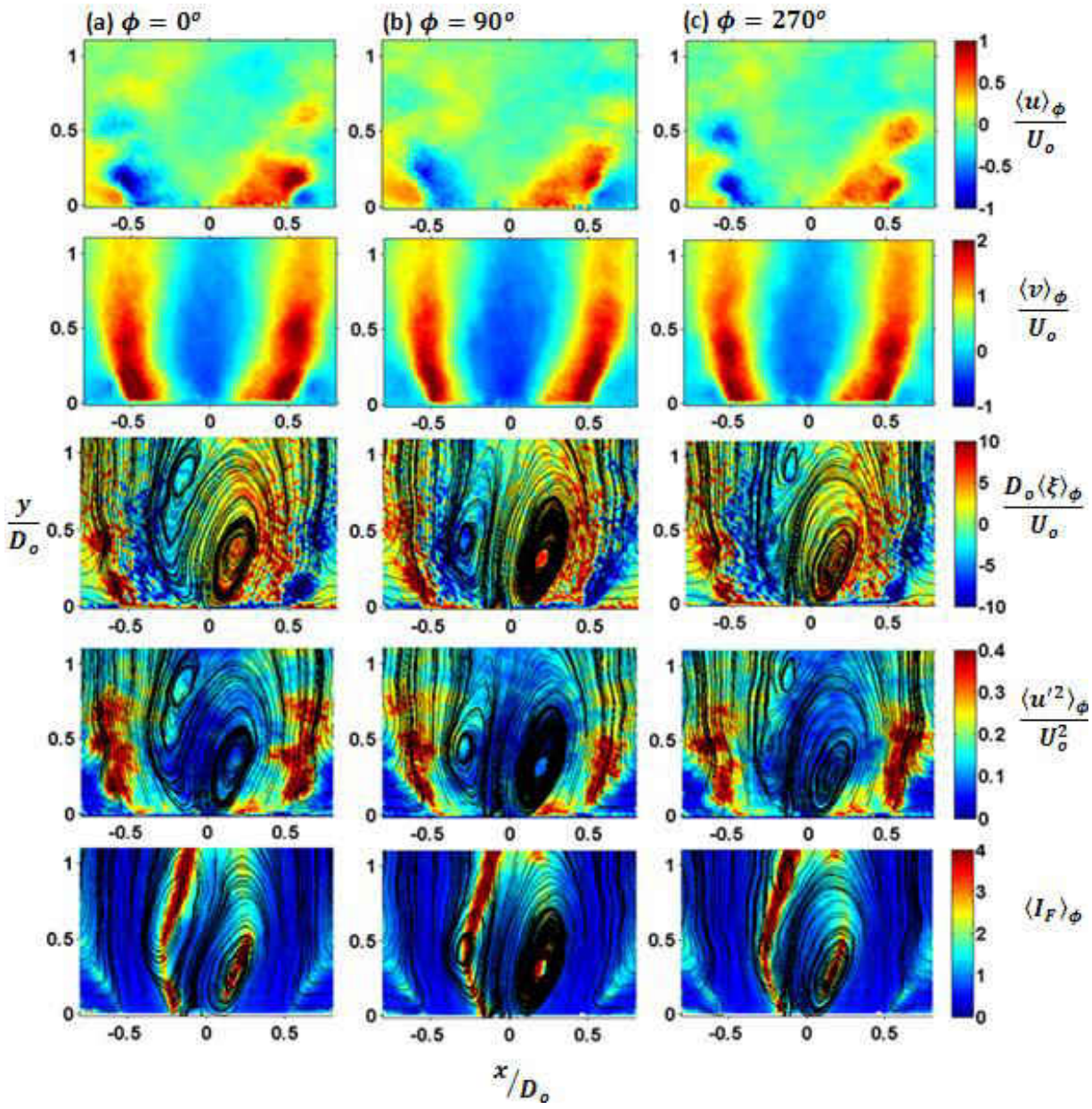

Figure 6.16: Phase Conditioned Fluid Dynamics – S034-C2-105Hz
a. ϕ = 0° | b. ϕ = 90° | c. ϕ = 270°

Clearly observable periodic shedding of eddy is once again observed for the high swirl flow configuration (S034-C2) forced at 105Hz in Figure 6.16. The phase conditioned axial velocity $\left(\frac{\langle u \rangle_\phi}{U_o}\right)$, radial velocity $\left(\frac{\langle v \rangle_\phi}{U_o}\right)$, vorticity $\left(\frac{D_o \langle \xi \rangle_\phi}{U_o}\right)$, kinetic energy $\left(\frac{\alpha \langle u'^2 \rangle_f}{U_o^2}\right)$ all exhibit the periodicity associated with the shedding of high energy eddies. Figure 6.16 shows a phase dependence in

the shedding phenomena with a maximum number of well defined eddies at a phase angle of 270^{o} relative to the imposed acoustic perturbation (Figure 6.16c). This result is consistent with the previously observed shedding phenomena reflected in the frequency averaged results for the S032-C2 flow configuration with 105Hz forcing in Figure 6.12b.

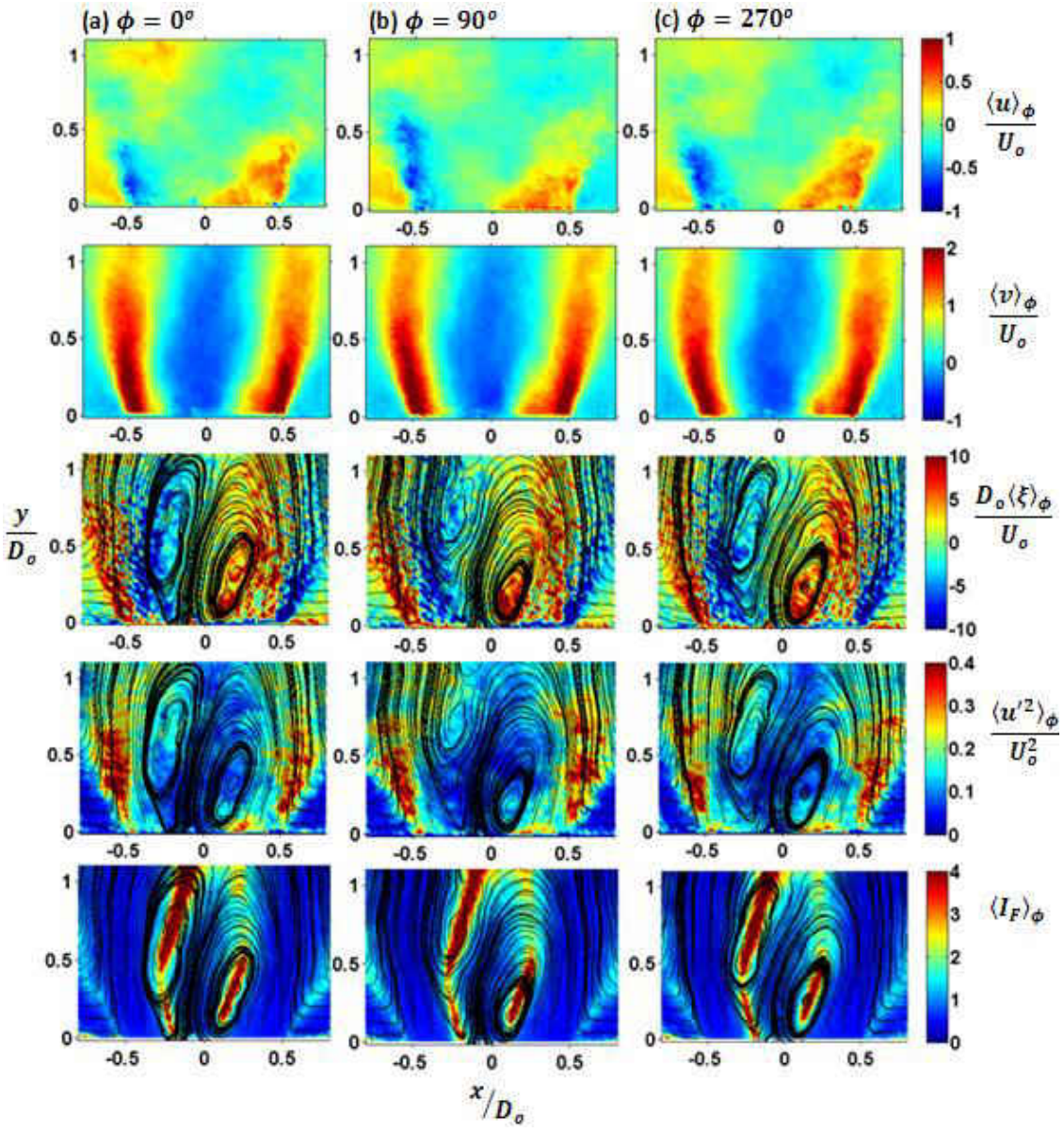

Figure 6.17: Phase Conditioned Fluid Dynamics – S034-C2-315Hz
a. ϕ = 0^{o} | b. ϕ = 90^{o} | c. ϕ = 270^{o}

When acoustic forcing is of 315Hz frequency imposed at to the S034-C2 from Figure 6.16, the periodic shedding of eddies is observed is observed to be significantly dampened as illustrated in Figure 6.17. The eddies in Figure 6.17 for forcing at 315Hz are less distinct compared to the case of acoustic forcing at 105Hz in Figure 6.16 for the exact same swirl intensity and fuel flowrate configuration. This clearly supports the conclusions regarding the 105Hz forcing mode as the frequency results in the most intense flame response in the present study.

6.5 Concluding Remarks

The examination of the fluid mechanics in this chapter reveals several important results associated with the flame response to acoustic forcing. These include the contributions of swirl intensity, fuel flowrate and forcing frequency on the fluid dynamics of the flame response. The first result is that the introduction of acoustic forcing leads to a narrowing of the inner recirculation zone (IRZ). This radially constrains the mixing vortices responsible for flame stabilization and leads to an increase in the flame aspect ratio.

Low swirl intensity is found to exacerbate the aspect ratio amplification. At higher swirl intensities, the inherent inertia associated with higher swirl restricts the degree of aspect ratio amplification reducing the stretching and the associated straining on the flame. The strain on flames subject to low swirl intensities is amplified by the downstream convection of the IRZ vortices even while the base of the flame remain attached to the fuel pipe. In the high swirl flames, the more compact high inertia IRZ undergoes an upstream displacement closer to the burner exit reducing the axial strain levels on the flame. However, there is an increase in asymmetry as the higher inertia mixing vortices are constrained in a narrowed IRZ from the pressure perturbations transported in the co-flowing air surrounding the inner recirculation zone.

The downstream displacement of the IRZ in the low swirl configuration was observed to exhibit a phase dependence relative to the acoustic forcing signal. Maximum downstream IRZ displacement occurred at the peak of the acoustic forcing with the reverse at the trough of the

acoustic forcing signal. Lean (C2) fuel flowrates exacerbated the downstream displacement in the lean flames while rich fuel flowrates (C1) reduced the phase dependence of the IRZ displacement. Increase stabilization at higher swirl intensities led to very minimal phase dependence in IRZ displacement.

The high swirl intensity flow configurations were found to be characterized by increased shedding of high energy eddies particularly the highly responsive 105Hz forcing mode. High energy shedding of eddies was observed at high swirl intensity even for fuel settings at which moderate to minimal flame responses (negative Flame Response indices) were observed. This implies that the a velocity $\langle u' \rangle$ to heat release rate $\langle q' \rangle$ perturbation phase requirement is important even in the presence of shedding phenomena. Another critical point is the lack of shedding phenomena in the highly responsive S009-C2 configuration which is also characterized by significant IRZ displacement suggesting the existence of two flame response modes. These include a flame stretching response at low swirl primarily driven by aspect ratio effects and a second mode at high swirl in which high energy shedding exacerbates the flame response.

CHAPTER 7 CONCLUSION

7.1 Concluding Discussion

In the present work, the flame response to acoustic perturbations in investigated using various experimental methods including CH* chemiluminescence imaging and intensity measurements, hot wire anemometry, particle image velocity (PIV) and dynamics pressure measurements via microphones. The resulting combustion dynamics data were analyzed with various methods including phase conditioning, FFT, the continuous wavelet transform (CWT) and acoustic impedance analysis.

The flame response is observed to exhibit a low-pass filter characteristic with minimal flame response beyond pulsing frequencies of 201Hz. Flames at lower fuel flow rates are observed to remain attached to the central fuel pipe at all acoustic pulsing frequencies. PIV imaging of the associated isothermal fields show the amplification in flame aspect ratio is caused by the narrowing of the inner recirculation zone (IRZ). Good correlation is observed between the estimated flame surface area and the heat release signature at higher swirl intensity flame configurations. A flame response index analogous to the Rayleigh criterion in non-forced flames is used to assess the potential for a strong flame response at specific perturbation configurations and is found to be a good predictor of highly responsive modes.

Wavelet analyses of heat release perturbations indicate highly responsive modes are characterized by sustained low frequency oscillations which accompany the high amplitude velocity perturbations at these modes. Higher intensity low frequency heat release oscillations are observed for lean flame/low pulsing frequency conditions. The complex acoustic impedance estimates of the various flame configurations illustrate strong frequency dependence in the resistance and reactance components. The positive reactance and negative resistive components of the acoustic impedance at highly responsive modes validate the amplifier flame characteristic observed below the cut-off frequency of 201Hz.

Phase conditioned analysis of the flame dynamics yield additional criteria in highly responsive modes to include the effective amplitude of velocity oscillations induced by the acoustic pulsing. In addition, highly responsive modes were characterized by velocity $\langle u' \rangle$ to heat release rate $\langle q' \rangle$ phase lag in the $\pm\pi/2$ range. A final observed characteristic in highly responsive flames is a Strouhal number between 1 and 3.5 based on the burner co-flow annulus diameter ($St = f_p U_{avg}/d_m$).

The analysis of the fluid dynamics in the inert and isothermal flow conditions suggest the prevalence of increased vortex shedding at higher swirl intensities particularly at the highly responsive acoustic forcing frequencies. The high swirl intensity flow configurations were found to be characterized by increased shedding of high energy eddies particularly the highly responsive 105Hz forcing mode.

High energy shedding of eddies was observed at high swirl intensity even for fuel settings at which moderate to minimal flame responses (negative Flame Response indices) were observed. This implies that the velocity $\langle u' \rangle$ to heat release rate $\langle q' \rangle$ perturbation phase requirement is important even in the presence of shedding phenomena. Another critical point is the lack of shedding phenomena in the highly responsive S009-C2 configuration which is also characterized by significant IRZ displacement suggesting the existence of two flame response modes. These include a flame stretching response at low swirl primarily driven by aspect ratio effects and a second mode at high swirl in which high energy shedding exacerbates the flame response.

Table 5: Flame Response Summary

Flame Configuration	Aspect Ratio (Lf/Wf)	IRZ Displ.	Periodic Eddy Shedding	Ambient Entrainment	|u'| Amp.	u' - q' Phase Lag (deg)	St	R	Response Mode
S009-C1-105	1.52	Moderate	Low	Low	> 0.12	+π	1.8	-0.82	
S009-C2-105	3.00	High	Minimal	Minimal	> 0.12	-π/2	1.8	0.48	Stretch
S034-C1-105	1.50	Minimal	High	High	>> 0.12	-3π/4	1.5	-0.95	
S034-C2-105	2.51	Minimal	Moderate	Moderate	>> 0.12	-π/4	1.5	1.32	Stretch + Shedding

Table 5 summarizes the relationship between the observed flame response and the isothermal fluid mechanics using four sample flame configurations, all pulsed at the highly responsive 105Hz forcing frequency. This clearly validates the suggestion that there are two possible response modes in the flames in the current study strongly driven by the swirl intensity. The first response mode is essential the results of high straining of the flame from the high aspect ratio resulting from acoustic forcing in a low swirl configuration.

The second response mode is observed to occur at high swirl where there is increased resistance to flame stretching and aspect ratio amplification. In this mode, velocity perturbations $\langle u' \rangle$ due to the periodic shedding of high energy eddies must be relatively in phase with the heat release rate $\langle q' \rangle$ oscillations in the flame. The result is an exacerbated flame response with some of the highest flame response indices in the studied flames.

The caveat in determining the flame response is the complex acoustic impedance (*Z*) of the flame. As was previously shown, it is entire possible to achieve high amplitude, relatively in-phase velocity perturbations that do not result in highly oscillatory responses if the real component of the acoustic impedance, *Re(Z)* is positive. In order words, a negative resistance component of the acoustic impedance (*Re(Z)* < 0) is required to elicit highly reactive oscillatory flame responses to imposed acoustics.

The following then represent the general criteria observed are necessary to result in highly oscillatory responses in the non-premixed swirling investigated in the current work:

- A Strouhal number requirement: $1 \leq St \leq 3.5$
- A velocity perturbation amplitude: $|\langle \hat{u} \rangle| \geq 0.12$;
- A $\langle q' \rangle$ to $\langle u' \rangle$ perturbation phase : $-90^{o} \leq \phi^{\langle u' \rangle - \langle q' \rangle} \leq 90o$
- A complex acoustic Impedance (Z): $Re(Z) < 0$, $Im(Z) > 0$

7.2 Future Considerations

The present effort has elucidated the various response mechanisms in non-premixed swirling flames. The natural extension of the current effort may include more detailed experiments to obtain the well defined flame transfer functions over the frequency domain. The impact of the velocity amplitude may need to be investigated in line with the Flame Describing Function methodology of several recent works [15-16, 26, 31].

The development of control methodologies to actively prevent the occurrence of combustion driven instabilities the ultimate goal of efforts to fundamentally understand thermoacoustic coupling phenomena. Based on the current research effort, the swirl intensity and fuel flowrate appear to be the clearest mechanisms by which the acoustic impedance may be manipulated to avoid thermoacoustic instabilities.

Future gas turbine will likely be required to meet even more stringent emission targets as well as the fuel flexibility to operate with a variety of biofuels. The will require even more fundamental studies such as those carried out in this effort to understand the interaction between combustion dynamics, acoustic and fluid mechanics that may drive the thermoacoustic instability process with varying fuel blends.

NOMENCLATURE

Roman

a	Continuous wavelet transform (CWT) scale
$A_{favg,fp}$	Time-average flame surface area from acoustic pulsing at frequency, f_p
$A_{favg,\phi}$	Average flame surface area at phase angle, ϕ from acoustic pulsing at frequency, f_p
C	Continuous wavelet transform coefficient
d_m	Mean burner annulus diameter: $d_m = R_i + R_o$
f_a	Frequency equivalent of wavelet transform scale, $f_a = f_c/a\Delta$
f_c	Center frequency of "mother wavelet"
f_p	Acoustic pulsing frequency
$F(x)$	Complex Fast Fourier Transform (FFT) of signal, x
$F(x,f_p)$	Complex Fast Fourier Transform (FFT) of signal x at frequency bin f_p
I_{CL}	CH* Chemiluminescence Image Centerline Intensity
I_u	Velocity fluctuation intensity
m_f	Fuel flow rate
m_{fr}	Baseline fuel flow rate ("richer" flame)
p'_1	Burner base pressure perturbations
p'_2	Burner exit pressure perturbations
q	Flame CH* chemiluminescence (heat release rate) intensity
q'	CH* chemiluminescence (heat release rate) intensity fluctuations ($q' = q-q_{avg}$)
$q'_{avg,fp}$	Time-average CH* chemiluminescence (heat release rate) from acoustic pulsing at pulsing frequency, f_p
$q'_{avg,\phi}$	Average CH* chemiluminescence (heat release rate) at phase angle (ϕ) from acoustic pulsing at frequency, f_p
r	Radial coordinate relative to burner axis
R_i	Inner radius of burner annulus
R_o	Outer radius of burner annulus
Re	Reynolds number: $Re = \rho U_{avg} d_m/\mu$
S	Swirl number
t	Time
t_P	Total data acquisition period
T_P	Acoustic pulsing period: $T_p = 1/(2\pi f_p)$
$u_{fp}(t)$	Time trace of velocity at pulsing frequency, f_p
u'	Velocity fluctuations: $u' = u-u_{avg}$
$u'_{avg,\phi}$	Average velocity fluctuation at phase angle (ϕ) from acoustic pulsing at frequency, f_p
u_{avg}	Spatial average velocity at burner exit plane
$u_{avg,fp}$	Time-average velocity fluctuation from acoustic pulsing at pulsing frequency, f_p
z	Axial coordinate vertically from burner exit plane

Greek

α	Fluctuation Intensity and Kinetic Energy Scaling factor
Δ	Signal sampling period
ϕ	Phase angle
ϕ_p	Acoustic pulsing signal phase
$\phi_d^{x'-y'}$	Phase difference from input perturbation, x' to output perturbation, y'
λ	Dynamic fuel flow rate decay constant
μ	Air dynamic viscosity
ρ	Air density
$\tau_d^{x'-y'}$	Time delay from input perturbation, x' to output perturbation, y': $\tau_d^{x'-y'} = \phi_d^{x'-y'}/(2\pi f_p)$

RELATED PUBLICATIONS

1. U. Idahosa, A. Saha, C. Xu and S. Basu, “Non-Premixed Acoustically Perturbed Swirling Flame Dynamics,” **Combustion and Flame** (2010), 10.1016/j.combustflame.2010.05.008.
2. U. Idahosa, A. Saha, C. Xu and S. Basu, “Coherence Dynamics, Wavelet Analysis and Transfer Functions of Non-Premixed Swirling Flames,” **Journal of Heat Transfer** (*In Review*), 2010.
3. U. Idahosa, A. Saha, S. Basu, C. Xu, “Acoustic Perturbation Effects on the Fluid Dynamics and Swirling Flame Response In A Non-Premixed Co-Flow Burner,” GT2010-23735, **Proceedings of the 2010 ASME Turbo Expo**, Glasgow, UK, June 14-18, 2010.
4. U. Idahosa, A. Saha, S. Basu, “Laser Diagnostics in an Acoustically Perturbed Non-Premixed Burner to Visualize Effects of Equivalence Ratio and Swirl-Intensity**,” 2010 Workshop on Application of Lasers In Mechanical Industries (WALMI)**, Jadavpur University, Kolkata, India, January 8 – 9, 2010.
5. U. Idahosa, A. Saha, C. Xu, S. Basu, "On the Fluid Dynamics of Acoustically Perturbed Swirling Non-Premixed Flames," **Proceedings of the Combustion Institute, Eastern States Section – Fall Technical Meeting 2009**, College Park, MD, October 18-21, 2009.
6. U. Idahosa, A. Saha, C. Xu, S. Basu, "Characterization of Combustion Dynamics in Swirl Stabilized Flames," **POWER2009-81168, Proceedings of ASME POWER 2009**, Albuquerque, NM, July 21-23, 2009.
7. U. Idahosa, A. Saha, C. Xu, S. Basu, "Frequency Response Characterization of Swirl-Stabilized Flame Dynamics," **Proceedings of the 6th U.S. National Combustion Meeting**, Ann Arbor, MI, May 17-19.

APPENDIX

REFERENCES

[1] G. J. Bloxsidge and A. P. Dowling. Reheat Buzz – An Acoustically Driven Combustion Instability. *Proceedings of the 9th AIAA/NASA Aeroacoustics Conference*, (AIAA-84-2321), Williamsburg, VA, 1984.

[2] T. Lieuwen. Modeling Premixed Combustion-Acoustic Wave Interactions: A Review. *Journal of Propulsion and Power*, 19(2):765-780, 2003.

[3] T. Lieuwen. *Investigation of Combustion Instability Mechanisms in Premixed Gas Turbines*. PHD thesis, Georgia Institute of Technology, Atlanta, GA, USA, August, 1999.

[4] V. K. Khannah. *A Study of the Dynamics of Laminar and Turbulent Fully and Partially Premixed Flames*. PHD thesis, Virginia Polytechnic Institute and State University, Blacksburg, VA, USA, July 2001.

[5] S. Pater. *Acoustic of Turbulent Non-Premixed Syngas Combustion*. PHD thesis, University of Twente, Enschede, The Netherlands, November 2007.

[6] T. Schuller, D. Durox and S. Candel. Self-Induced Combustion Oscillations of Laminar Premixed Flames Stabilized on Annular Burners. *Combustion and Flame*, 135:525-537, 2003.

[7] S. Candel, D. Durox and T. Schuller. Flame Interactions as a Source of Noise and Combustion Instabilities. *Proceedings of the 10th AIAA/CEAS Aeroacoustic Conference*, (AIAA2004-2928), 2004.

[8] S. Nair and T. Lieuwen. Acoustic Detection of Blowout in Premixed Flames. *Journal of Propulsion and Power*, 21(1): 32-39, 2005.

[9] T. Schuller, S. Ducruix, D. Durox, S. Candel. Modeling Tools for the Predictions of Premixed Flame Transfer Functions. *Proceedings of the Combustion Institute*, 29:107-113, 2002.

[10] Preetham, T. Lieuwen. Nonlinear Flame-Flow Transfer Function Calculations: Flow Disturbance Celerity Effects. *Proceedings of the 40th AIAA/ASME/SAE/ASEE Joint Propulsion Conference and Exhibit*, *Fort Lauderdale, FL,* (AIAA 2004-4035), July 2004.

[11] Preetham, H. Santosh and T. Lieuwen. Dynamic of Laminar Premixed Flames Forced by Velocity Disturbances. *Journal of Propulsion and Power*¸24(6):1390-1402, 2008.

[12] Lord Rayleigh. The Explanation of Certain Acoustical Phenomena. *Royal Institution Proceedings*, 8:536-542, 1878.

[13] S. Shanbhogue and T. Lieuwen. Studies on the Vorticity Field of Harmonically Excited Bluff Body Flames. *Proceedings of the 46th AIAA Aerospace Sciences Meeting, Reno, NV*, (AIAA2008-122), January 2008.

[14] F. Nicoud and T. Poinsot. Thermoacoustic Instabilities: Should the Rayleigh Criterion Be Extended to Include Entropy Changes? *Combustion and Flame*, 142:153–159, 2005.

[15] D. Durox, T. Schuller, N. Noiray, A.L. Birbaud and S. Candel. Rayleigh Criterion and Acoustic energy Balance in Unconfined Self-Sustained Oscillating Flames. *Combustion and Flame*, 156:106–119, 2009.

[16] D. Durox, T. Schuller, N. Noiray and S. Candel. Experimental Analysis of Nonlinear Flame Transfer Functions for Different flame Geometries. *Proceedings of the combustion Institute*, 32:1391-1398, 2009.

[17] K. T. Kim, J. G. Lee, H. J. Lee, B. Quay and D. Santavicca. Characteristics of Forced Flame Response of Swirl-Stabilized turbulent Lean-Premixed Flames in a Gas Turbine Combustor. *Proceedings of ASME Turbo Expo 2009, Orlando, FL*, (GT2009-60031), June 2009.

[18] D. Durox, T. Schuller and S. Candel. Combustion Dynamics of Inverted Conical Flames. *Proceedings of the Combustion Institute*, 30:1717-1724, 2005.

[19] A. Chaparro, E. Landry and B.M. Cetegen. Transfer Function Characteristics of Bluff-Body Stabilized Conical V-Shaped Premixed Turbulent Propane-air Flames. *Combustion and Flame,* 145: 290–299, 2006.

[20] C. Schulz and V. Sick. Trace-LIF Diagnostics: Quantitative Measurement of Fuel Concentration, Temperature and Fuel/Air Ratio in Practical Combustion Systems. *Progress in Energy and Combustion Science,* 31:75-121, 2005.

[21] B.O. Ayoola, R. Balachandran, J.H. Frank, E. Mastorakos and C.F. Kaminski. Spatially Resolved Heat Release rate Measurements in Turbulent Premixed Flames. *Combustion and Flame,* 144:1-16, 2006.

[22] C. M. Vagelopoulos and J. H. Frank. An Experimental and Numerical Study on the Adequacy of CH as a Flame Marker in Premixed Methane Flames. *Proceedings of the Combustion Institute*, 30:241-249, 2005.

[23] T. Yi and D. Santavicca. Flame Spectra of a Turbulent Liquid-fueled Swirl-Stabilized LDI Combustor. *Proceedings of the 47th AIAA Aerospace Sciences Meeting, Orlando, FL*¸ (AIAA2009-985), January 2009.

[24] S. Tachibana, J. Yamashita, L. Zimmer, K. Suzuki and A.K. Hayashi. Dynamic Behavior of a Freely Propagating Turbulent Premixed Flame Under Global Stretch-Rate Oscillations. *Proceedings of the Combustion Institute*, 32:1795-1702, 2009.

[25] S. Nair and T. Lieuwen. Near Blowoff Dynamics of a Bluff Body Stabilized Flame. *Journal of Propulsion and Power*, 23(5):421-427, 2007.

[26] P. Palies, D. Durox, T Schuller, P. Morenton and S. Candel. Dynamics of Premixed Confined Swirling Flames. *Comptes Rendus Mechanique*, 337:395-405, 2009.

[27] P. Palies, D. Durox, T. Schuller, S. Candel. The Combined Dynamics of Swirler and Turbulent Premixed Swirling Flames. *Combustion and Flame*, 2010 (In Press), doi:10.1016/j.combustflame.2010.02.011.

[28] B.D. Bellows, Y. Neumeier and T. Lieuwen. Forced Response of A Swirling Premixed Flame to Flow Disturbances. *Journal of Propulsion and Power*, 22(5):1075-1084, 2006.

[29] D. Fritsche, M. Furi and K. Boulouchos. An Experimental Investigation of Thermoacoustic Instabilities in a Premixed Swirl-Stabilized Flame. *Combustion and Flame*, 151:29-36, 2007.

[30] N. Noiray, D. Durox, T. Schuller and S. Candel. Passive Control of Combustion Instabilities Involving Premixed Flames Anchored on Perforated Plates. *Proceedings of the Combustion Institute*, 31:1283–1290, 2007.

[31] N. Noiray, D. Durox, T. Schuller and S Candel. A Unified Framework for Nonlinear Combustion Instability Analysis Based on the Flame Describing Function. *Journal of Fluid Mechanics*, 615:139-167, 2008.

[32] C.J. Lawn, S. Evesque and W. Polifke. A Model for the Thermoacoustic Response of a Premixed Swirl Burner. Part I: Acoustic Aspects. *Combustion Science and Technology*, 176 (2004) 1331-1358.

[33] Z. S. Li, B. Li, Z. W. Sun, X. S. Bai and M. Alden. Turbulence and Combustion Interaction High Resolution Local Flame Front Structure Visualization Using Simultaneous Single-Shot PLIF Imaging of CH, OH and CH20 in a Piloted Premixed Jet Flame. *Combustion and Flame,* 2010 (In Press), doi:10.1016/j.combustflame.2010.02.017.

[34] D. Fanaca, P. R. Alemala, C. Hirsch, T. Sattlemayer and B. Schuermans. Comparison of the Flow Field of a Swirl Stabilized Premixed Burner and a Single Burner Combustion Chamber. *Proceedings of ASME Turbo Expo 2009, Orlando, FL*, (GT2009-59884), June 2009.

[35] S. Chaudhuri and B.M. Cetegen. Blow-Off Characteristics of Bluff-Body Stabilized Conical Premixed Flames with Upstream spatial Mixture Gradients and Velocity Oscillations. *Combustion and Flame*, 153:616-633, 2008.

[36] S. Chaudhuri and B.M. Cetegen. Response Dynamics of Bluff-Body stabilized Conical Premixed Turbulent Flames with Spatial Mixture Gradients. *Combustion and Flame*, 156:706-720, 2009.

[37] Y. M. Marzouk, A. F. Ghoniem, H. N. Najm. Dynamic Response of Strained Premixed Flames to Equivalence Ratio Gradients. *Proceedings of the combustion Institute*, 28:1859-1866, 2000.

[38] A. Giannadakis, K. Perrakis and T. Panidis. Swirling Jet Under the Influence of Coaxial Flow. *Experimental Thermal and Fluid Science*, 32:1548-1563, 2008.

[39] M.M. Ribeiro and J.H. Whitelaw. Coaxial Jets With and Without Swirl. *Journal of Fluid Mechanics*, 96:769-795, 1980.

[40] C.K. Chan, K.S. Lau, W. K. Chin and R.K. Cheng. Freely Propagating Open Premixed Turbulent Flames Stabilized By Swirl. *Twenty-Fourth Symposium (International) on Combustion*, pp. 511–518, 1992.

[41] W. Fick, N. Syred, A. J. Griffiths and T. Odoherty. Phase-Averaged Temperature Characterization in Swirl Burners. *Proceedings of the Institute of Mechanical Engineers*, 210(A01995):383-395, 1996.

[42] C. O. Paschereit, F. Bauermeister and E. Gutmark. Lean Blow-Out control Using and Auxiliary Premixed Flame in a Swirl Stabilized Combustor. *Proceedings of the 43rd AIAA/ASME/SAE/ASEE Joint Propulsion Conference & Exhibit, Cincinnati, OH*, (AIAA2007-5632), July 2007.

[43] A. Umemura and T. Owaki. Premixed Swirl Combustion Modes Emerging for a Burner Tube with Converging Entrance. *Proceedings of the Combustion Institute*, 31:1067-1074, 2007.

[44] C. C. Kulsheimer and H. Buchner. Combustion Dynamics of Turbulent Swirling Flames. C*ombustion and Flame*, 131:70-84, 2002.

[45] B. Bellows, M. K. Bobba, J. M. Seitzman and T. Lieuwen. Nonlinear Flame Transfer Function Characteristics in a Swirl Stabilized Combustor. *Journal of Engineering for Gas Turbines and Power*, 129:954-961, 2007.

[46] C. O. Paschereit, B. Schermans, W. Polifke and O. Mattson. Measurements of Transfer Matrices and Source Terms of Premixed Flames. *Journal of Engineering for Gas Turbines and Power*, 124:239-247, 2002.

[47] E. Freitag, H Konle, M. Lauer, C. Hirsch and T. Sattlemayer. Pressure Influence on the Flame Transfer Function of a Premixed Swirling Flame. *Proceedings of the ASME Turbo Expo, Barcelona, Spain*, (GT2006-90540), May 2006.

[48] V. V. Golubev and H. Atassi. Sound Propagation in an Annular Duct with Mean Potential Swirling Flow. *Journal of Sound and Vibration*, 198(5):601-616, 1996.

[49] A. V. Grebennikov. Stability of Negative Resistance Oscillator Circuits. *International Journal of Electrical Engineering Education*, 36:242-254, 1999.

[50] H. Hou and J. H. Yang. An Electro-Acoustics Impedance Error Criterion and its Application to Active Noise Control. *Applied Acoustics*, 65:485-499, 2004.

[51] L.E. Kinsler, A.R. Frey, A.B. Coppens and J. V. Sanders. *Fundamentals of Acoustics*. John Wiley & Sons, 1982.

[52] R. Singh and M. Schary. Acoustic Impedance Measurements Using Sine Sweep Excitation and known Volume Velocity Technique. *Journal of the Acoustical Society of America*, 64(4):995-1003, 1978.

[53] J. P. Dalmont. Acoustic Impedance Measurements Part I: A Review. *Journal of Sound and Vibration*, 243(3):427–439, 2001.

[54] M. Atig, J. P. Dalmont, J. Gilbert. Termination Impedance of Open-Ended Cylindrical Tubes at high Sound Pressure Level. *Comptes Rendus Mechanique*, 332:299-304, 2004.

[55] P. Dickens, J. Smith and J. Wolfe. Improved Precision in Measurements of Acoustic Impedance Spectra Using Resonance-Free Calibration Loads and Controlled Error Distribution. *Journal of the Acoustic Society of America*, 121(3):1471–1481, 2007.

[56] R. F. Huang, S. C. Yen. Aerodynamic Characteristics and Thermal Structure of Non-Premixed Reacting Swirling Wakes at Low Reynolds Numbers. *Combustion and Flame*, 155:539-556, 2008.

[57] M. P. Juniper, L. K. B. Li and J. W. Nichols. Forcing of Self-Excited Round Jet Diffusion Flames. *Proceedings of the Combustion Institute*, 32:1191-1198, 2009.

[58] Stephen R. Turns. *An Introduction to Combustion*. McGraw Hill Higher Education, 2nd Edition, 2000.

[59] D. Feikema, R. H. Chen and J. F. Driscoll. Blowout Limits for Swirling Premixed and Non-Premixed Flame. C*ombustion and Flame*, 80:183-195, 1990.

[60] P. Koutmos. A Damkohler Number Description of Local Extinction in Turbulent Methane Jet Diffusion Flames. *Fuel*, 78:623-626, 1999.

[61] W. Leuckel, P. Habisreuter and H. P. Scmid. A Model for Calculating Heat Release in Premixed Turbulent Flames. *Combustion and Flame*, 113:79-91, 1998.

[62] G. H. Markstein. *Nonsteady Flame Propagation.* Macmillan, NY, 1964.

[63] T. Schuller, D. Durox and S. Candel. A Unified Model for the Prediction of Laminar Flame Transfer Functions: Comparisons between Conical and V-Flame Dynamics. *Combustion and Flame*, 134:21-34, 2003.

[64] M. Fleifil, A.M. Annaswamy, Z.A. Ghoneim and A.F. Ghoniem. Response of a Laminar Premixed Flame to flow Oscillations: A Kinematic Model and Thermoacoustic Instability Results. *Combustion and Flame*, 106:487-510, 1996.

[65] T. Lieuwen and B.T Zinn. The Role of Equivalence Ratio Oscillations in Driving Combustion Instabilities in Low NOx Gas Turbines. *Twenty-Seventh Symposium (International) on Combustion*, pp. 1809–1816, 1998.

[66] W. Polifke and C. J. Lawn. On the Low-Frequency Limit of Flame Transfer Functions. *Combustion and Flame*, 151:437-451, 2007.

[67] J.H. Cho and T. Lieuwen. Laminar Premixed Flame Response to Equivalence Ratio Oscillations. *Combustion and Flame*, 140:116-129, 2005.

[68] D. You, Y. Huang and V. Yang. A Generalized Model of Acoustic Response of turbulent Premixed Flame and its Application to Gas Turbine Combustion Analysis. *Combustion Science and Technology*, 177:1109-1150, 2005.

[69] S. Kang, H. Kim, J. Lee and Y. Kim. Stabilization and combustion Processes of turbulent Premixed Lifted Methane-Air Flames on Low-Swirl Burner. *Energy & Fuels*, 22:925-934, 2008.

[70] Y. Huang and V. Yang. Combust. Bifurcation of Flame Structure in a Lean Premixed Swirl Stabilized Combustor: Transition from Stable to Unstable. *Combustion and Flame*, 136:383-389, 2004.

[71] N. Syred and K. R. Dahman. Effect of High Levels of Confinement Upon the Aerodynamics of Swirl Burners. *Journal of Energy*, 2(1):8-15, 1978.

[72] N. Syred. A Review of Oscillation and the Role of the Precessing Vortex Core (PVC) in Swirl Combustion Systems. *Progress in Energy and combustion Science*, 32:93-161, 2006.

[73] P.H. Renard, D. Thevenin, J.C. Rolon and S. Candel. Dynamics of Flame/Vortex Interactions. *Progress in Energy and Combustion Science*, 26:225-282, 2000.

[74] A. K. Gupta and S. S. Archer. Behavior of Unconfined Swirling Flames Under Fuel-Lean Conditions Using Particle Image Velocimetry. *Proceedings of IDETC/CIE 2006, Philadelphia, PA*, (DETC2006-99132), September 2006.

[75] T. Ivanic, E. Foucault and J. Pecheux. Dynamics of Swirling Jet Flows. *Experiments in Fluids*, 35:317-324, 2003.

[76] A. Lehr and A Boles. Experimental Investigation of the Periodic Unsteady Transonic Flow Field Around a Compressor Blade by Means of Particle Image Velocimetry (PIV). *International Journal of Rotating Machinery*, 10(5):401-413, 2004.

[77] Y. M. Al-Abdeli and A. R. Masri. Recirculation and Flow Field Regimes of Unconfined Non-Reacting Swirling Flows. *Experimental Thermal and Fluid Science*, 27:655-665, 2003.

[78] Y. Zhang, D. Shomikuri, Y. Mukae and S. Ishizuka. Flow Field in Swirl Type Tubular Burner. *JSME International Journal, Series B*, 48(4):830-838, 2005.

[79] S. V. Alekseenko, Y. M. Dulin, Y. S. Kozorenov and D. M. Markovich. Effect of Axisymmetric forcing on the Structure of A Swirling Turbulent Jet. *International Journal of Heat and Fluid Flow*, 29:1699-1715, 2008.

[80] Y. Maciel, L. Facciolo, C. Duwig, L. Fuchs and P. H. Alfredsson. Near Field Dynamics of a Turbulent Round Jet with Moderate Swirl. *International Journal of Heat and Fluid Flow*, 29:675-686, 2008.

[81] J. Cai, Y. Fu, N. Flohre, S. M. Jeng and H. Mongia. Experimental Study on Coherent Structures of a Counter Rotating Multi-Swirler Cup. *Proceedings of the 43rd AIAA/ASME/SAE/ASEE Joint Propulsion Conference and Exhibit, Cincinnatti, OH*, (AIAA2007-5674), July 2007.

[82] W. Shanwu, S. Y. Hsieh, V. Yang. Unsteady Flow Evolution in Swirl Injector with Radial Entry. *Physics of Fluids*, 17(045106), 2005.

[83] K. K. J. Ranga Dinesh, M. P. Kirkpatrick. Study of Jet Precession Recirculation and Vortex Breakdown in Turbulent Swirling Jets Using LES. *Computers and Fluids*, 38:1232-1242, 2009.

[84] G. A. Siamas, X. Jiang and L. C. Wrobel. Numerical Investigations of a Perturbed Swirling Two-Phase Jet. *International Journal of Heat and Fluid Flow*, 30:481-493, 2009.

[85] A. Olivanti, G. Solero, F. Cozzi and A. Coghe. Near Field Flow Structure of Isothermal Swirling Flows and Reacting Non-Premixed Swirling Flows. *Experimental Thermal and Fluid Science*, 31:427-436, 2007.

[86] M. Misiti, Y. Misiti, G. Oppenheim and J.M. Poggi. *Wavelet Toolbox 4. Matlab Users Guide*. Mathworks, 2009.

[87] T. Poinsot, F. Nicoud and A. Giauque. Validation of a flame Transfer Function Reconstruction Method for Complex Turbulent Configurations. *Proceedings of the 14th AIAA/CEAS Aeroacoustics Conference, Vancouver, BC, Canada*, (AIAA2008-2943).

[88] F. Nicoud, L. Benoit, C. Sensiau and T. Poinsot. Acoustic Modes in Combustors with Complex Impedances and Multidimensional Active Flames. *AIAA Journal*, 45(2): 426-441, 2007.